



University of Tennessee, Knoxville

Trace: Tennessee Research and Creative Exchange

Doctoral Dissertations

Graduate School

8-2019

Single Crystal to Polycrystal Neutron Simulation

Luc Dessieux Dessieux

University of Tennessee, ldessieu@vols.utk.edu

Follow this and additional works at: https://trace.tennessee.edu/utk_graddiss

Recommended Citation

Dessieux, Luc Dessieux, "Single Crystal to Polycrystal Neutron Simulation. " PhD diss., University of Tennessee, 2019.

https://trace.tennessee.edu/utk_graddiss/5580

This Dissertation is brought to you for free and open access by the Graduate School at Trace: Tennessee Research and Creative Exchange. It has been accepted for inclusion in Doctoral Dissertations by an authorized administrator of Trace: Tennessee Research and Creative Exchange. For more information, please contact trace@utk.edu.

Single Crystal to Polycrystal Neutron Transmission Simulation

A Dissertation Presented for the

Doctor of Philosophy

Degree

The University of Tennessee, Knoxville

Luc Lucius Dessieux

August 2019

© by Luc Lucius Dessieux, 2019
All Rights Reserved.

To Olivera, Mateya and Neven

Acknowledgements

The work that is presented herein has been made possible with the help of many people who I would like to thank. First, I would like to express my deepest gratitude to my major Professor Dr. Mike Guidry, for his patience, his guidance, and his constant support during my graduate research years at UTK for both my masters project and later my PhD project. I am grateful to Dr. Philip Bingham for the opportunity to work on the neutron Transmission problem, his mentor-ship and friendship. I am specially thankful to Dr. Alexandru Stoica for the knowledge of neutron physics and crystal physics I acquired under his guidance. In addition I would like to thank the other members of my committee: Dr. Takeshi Egami and Dr. Geoffrey Greene for their time and effort devoted to the completion of my Ph.D. degree.

I would like to express my gratitude to my colleagues from the research group: Dr. Venkatakrisnan, Singanallur V.(Venkat), Dr. Aravind Mikkilineni, and Mr. David Cornett for their help with editing my thesis and practicing my defense. I like to share my thanks to Dr. Vincent Paquit for sharing his office space with me during my time at ORNL.

I want to also acknowledge Dr. Yarom Polsky and Dr. Dayakar Penumadu for their time and assistance in the completion of my Ph.D. degree.

I would also like to Thank Dr. Soren Sorensen and Dr. Hanno Weiterin, the former and present head of the physics department, for the award of a teaching assistantship. I also thank Dr. Marianne Breinig for her guidance and instructional support during my time as a graduate student and teaching assistant.

Special thanks to my parents Luc and Jaccinette for supporting me in the pursuit of this degree, to my siblings Rools, Lesly, Guesly, Sabine, and Melinda for their support in pursuit of this thesis.

Last but not least, I express my deepest gratitude to my wife Olivera, my daughter Mateya, and my son Neven for their support, love, and laughter in the pursuit of this degree.

Abstract

The holy grail for inspection of manufactured parts is being able to place an arbitrary part in a measurement system that generates a 3-D map of grain size, orientation, and strain within the part at 10 μm resolution. Current measurement capabilities are far from this ideal and development of models, instruments and algorithms is needed to reach this ideal. Over the past two decades the technique of Bragg-edge neutron transmission along with computed tomography algorithms has materialized as a potential technique to obtain three-dimensional maps within the bulk of materials. To date, these techniques have been applied only to simplistic three-dimensional strains without consideration of texture. In this work, a new approach to modeling Neutron Bragg-edge transmission is investigated. The basic principle of the Bragg-edge transmission technique is the measurement of transmission of cold and thermal neutrons through polycrystalline materials. The spectral signatures of the transmission are based on the sample's-crystal symmetry, and atomic parameters. The shape, position, and relative magnitude of these Bragg-edge spectral signatures contain information about grain size, grain orientation, and the average strain within the sample that is collinear with the incident beam.

The focal point of this thesis is the development of a new neutron Bragg-edge transmission simulation code in which the user can define distributions for grain

size, mosaic distribution per grain, grain orientations (texture), and general three-dimensional strain on the grain systems of the sample. A theoretical neutron cross-section calculation for single crystals dependent on crystallographic description of the sample, granular topology, and the strain state of the grain is applied to each crystal in the defined distribution to model the Bragg-edge effect in polycrystalline materials. The cross-section calculation is implemented using the python scripting language and the simulation tool is used to investigate the transmission spectrum of single crystals and polycrystalline materials. In order to verify the transmission spectrum, simulations spectra are compared to neutron transmission taken at the VULCAN instrument at the Spallation Neutron Source. Comparison of the simulation spectra to those found in literature are also presented.

Table of Contents

1	Introduction	1
1.1	Basic Properties of the Neutron	9
1.2	Neutron Generation	10
1.3	Neutron Moderation	11
1.4	Neutron Detection	12
1.5	Neutron Wavelength	13
1.6	Neutron Strain Measurements	15
1.7	Grain-Interaction Models	17
1.7.1	Voigt Model	18
1.7.2	Reuss Model	19
1.7.3	Hill Model	19
1.8	Why Another Bragg-Edge Simulation Package	20
1.9	Structure of Thesis	21
2	Neutron Interaction with Crystalline Material	23
2.1	Neutron Interaction with Matter	24
2.1.1	Nuclear Cross Section	24
2.1.2	Elastic Cross Section	25
2.1.3	Scattering Length	26
2.1.4	Interaction with Crystals	27
2.1.5	Inelastic Cross Section	29

2.1.6	Absorption Cross Section	29
2.1.7	Diffraction of Neutrons by a Polycrystalline Element	29
2.1.8	Debye Waller Factor	31
2.2	Neutron Transport Equation in Mosaic Crystals	33
2.2.1	Scattering and Absorption Probabilities	38
2.2.2	Generalized Darwin Equation	41
2.2.3	Darwin Equation for a Mosaic Slab Crystal	43
2.2.4	Solution of the Darwin Equations	45
2.3	Attenuation of Neutrons by Crystals	49
2.3.1	Absorption Cross Section	49
2.3.2	Thermal Diffuse Scattering	50
2.3.3	Bragg Scattering Cross Section	52
3	Implementation	57
3.1	Input Parameters	57
3.1.1	Crystal Data	58
3.1.2	Sample Data	59
3.1.3	Instrumentation Data	62
3.2	Crystal/Sample Orientation	62
3.2.1	Crystals in Sample's Coordinate System	62
3.2.2	Sample in Laboratory' Coordinate System	65
3.2.3	Calculation of Direction Cosines	66
3.3	Single Crystal Transmission	68
3.4	Total Transmission	68
3.5	Polycrystal Transmission	68
3.6	Computing Considerations	69
4	Sinpol: Testing and Verification	71
4.1	Single Crystal	71
4.1.1	Extinction	76

4.2	Polycrystalline Simulation	77
4.2.1	Voxel-Grain Ration	78
4.2.2	Extinction	80
4.2.3	Log-normal Distribution of Grains	81
4.3	A Comparison with Experimental Results	84
4.4	Conclusion	85
5	Extending Sinpol for Texture	87
5.1	Introduction	87
5.2	Orientation Distribution Function	92
5.3	Neutron Simulation of Texture	95
5.4	Grain Statistics at Bragg-edges	106
5.5	A Comparison with Experimental Results	111
5.6	Summary	116
6	Extending Sinpol for Strain Simulation	118
6.1	Macro-Strain to Lattice Strain	119
6.1.1	Single Crystal Macro-Strain to Lattice Strain Transformation	120
6.1.2	Single Crystal Macro-Strain to Lattice Strain Simulation Results	121
6.1.3	Polycrystal Macro-Strain to Lattice Strain	126
6.2	Macro-Stress to Lattice Strain	133
6.2.1	Single Crystal Macro-Stress to Lattice Strain Calculation . . .	133
6.2.2	Single Crystal Macro-Stress to Lattice Strain Simulation Results	136
6.2.3	Polycrystal Macro-Stress to Lattice Strain	138
6.3	Phenomenological Model	142
6.4	Summary	146
7	Summary	148
7.1	Discussion and Conclusions	148
7.2	Future Work	151

Bibliography	153
Appendix	170
A Inter planar spacing, unit cell volumes, inclination angles	171
A.1 Inte-Planar Spacing	171
A.2 Unit Cell Volume	172
A.3 Inclination angles	173
B Input File Example	175
C Generation of Log-normal Distribution of Thicknesses	177
Vita	180

List of Tables

1.1	Classification of neutrons [45]	12
4.1	Physical parameters for simulations of Cu, Fe, and Ni samples.	72
4.2	Typical parameters of the peaks observed in (1-T), simulated along the [110] direction of the reference copper sample and compared to measurement by Santisteban [7].	75
4.3	Refined and derived peak parameters for the copper sample and compared to measurement by Malamud [96].	77
5.1	Physical parameters for simulations of Cu, Al, and Inconel samples.	95
5.2	Enhanced Bragg-edges for different texture components with the sample at two selected angles.	105
5.3	Number of grains contributing to Bragg-edges of different texture components with the sample at $\rho = 0$ degrees.	110
5.4	Number of grains contributing to Bragg-edges of different texture components with the sample at $\rho = 90$ degrees.	110
5.5	Nominal chemical composition of Inconel 718 powder in weight percent (wt.%).	112
6.1	Comparison between theoretical wavelength position and simulated wavelength position for 4 peaks with 1000 Mpa applied stress	136
6.2	B value obtained from fitting diffraction experiment	144

6.3	Comparison between simulated strain and measured on 316 stainless steel sample with loading direction parallel to loading direction. . . .	146
6.4	Comparison between simulated strain and measured on 316 stainless steel sample with loading direction perpendicular to loading direction.	146

List of Figures

1.1	Transmission measurement at ISIS showing the residual elastic strain around a cold- expanded hole in a 12 mm thick steel plate. The measured strains correspond to the through thickness average of the out-of-plane strains. [28]	7
1.2	Neutron transmission probes the projected strain which for the ring and plug sample consists of a combination of hoop and radial strain components. (b) Projected strain as a function of sample radius and corresponding data collected at ENGIN-X. [20]	7
1.3	Comparison of strain map from modelling (left) and Bragg-edge imaging (right). [13]	8
1.4	Coordinate system used to measure strain with diffraction. The laboratory coordinate system X'_3 is related to the sample coordinate system X_i by the orientation angles ψ, ϕ	17
2.1	The relationship between the incident wavevector k_0 , the final wavevector k_1 , and the scattering vector \mathbf{Q}	24
2.2	Geometry of scattering.	25
2.3	Total scattering cross section for a rigid lattice [79].	31
2.4	Segmented plate with A columns and with columns containing N distinct grain orientations. Each grain transmission is calculated, a distribution of grains is aggregated to form voxel transmission; with voxel transmission, a sample's transmission can be calculated.	56

3.1	Schematic of <i>Sinpol</i> architectural organization.	58
3.2	Neutron transmission simulation of a copper crystal for various mosaic spreads.	60
3.3	Neutron transmission simulation of a copper single crystal for various orientations.	61
3.4	Neutron transmission simulation through different thickness of single crystal copper.	61
3.5	Schematic representation of Euler angles, as defined by Bunge[92]. . .	63
3.6	Scattering path in a plane-slab crystal, showing the relationship between the diffraction beam \vec{S}_H and the incident beam \vec{S}_o , and the relationship between the incident beam \vec{S}_o and the sample's normal \vec{Y}_3^S . . .	67
3.7	Neutron Transmission of a copper powder for various mosaic spreads. . .	69
4.1	Movement of peak locations and intensity as a function of crystal rotation for a single crystal.	73
4.2	(top) Neutron transmission spectra of single copper crystal. (bottom) Shifts in peak position as a result of rotation of sample, solid line the incident beam is aligned with [110] direction, dashed line sample is rotated by 1 and 2 degrees in the transverse direction.	74
4.3	Simulated copper neutron transmission with 10 million distinct crystallites orientations.	78
4.4	Copper neutron transmission for 10 distinct crystallites orientations, 100 distinct crystallites orientations, 1000 distinct crystallites orientations and 10000 distinct crystallites orientations.	79
4.5	Neutron transmission simulations of copper polycrystals, with grain sizes of $\tau = 1000\mu\text{m}$, $\tau = 100\mu\text{m}$, $\tau = 10\mu\text{m}$, and $\tau = 1\mu\text{m}$	80
4.6	Neutron simulation through a 1-cm copper plate using a log-normal distribution to represent the grain size, with varying b_{LN} ; the mean size τ_v was kept to $1\mu\text{m}$	82

4.7	The relationship of the standard deviation of the neutron transmission simulation (STD_{NT}) to the relative standard deviation of a log-normal distribution (c_v).	83
4.8	As the relative standard deviation (c_v) of the log-normal grain size distribution increases, the grain size population will move toward larger grain sizes. The neutron transmission simulation spectra of a log-normal distribution with $b_{LN} = 10$ resembles the neutron simulation spectra of a single crystal.	83
4.9	Comparison of simulated neutron transmission of Fe and Ni to neutron transmission measurement of Fe and Ni.	84
5.1	<i>Sinpol</i> transmission simulation results for copper: (a) single crystal at one orientation, (b) single crystal over rotations round one axis, (c) powder at one orientation, and (d) powder over rotations around one axis.	96
5.2	Cube texture neutron transmission simulation spectra for copper sample with populations of 10 grains, 100 grains, 1000 grains, and 10000 grains.	98
5.3	<i>Sinpol</i> simulated cube texture ideal component pole figures (a) with associated inverse pole figure (b) and corresponding neutron transmission simulation for a copper sample with its RD aligned along the neutron beam (c), (d) map of sample rotated along the vertical axis, and (e) copper sample with its ND aligned along the neutron beam.	99
5.4	<i>Sinpol</i> simulated goss texture ideal component pole figures (a) with associated inverse pole figure (b) and corresponding neutron transmission simulation for a copper sample with its RD aligned along the neutron beam (c), (d) map of sample rotated along the vertical axis, and (e) copper sample with its ND aligned along the neutron beam.	101

5.5	<i>Sinpol</i> simulated brass texture ideal component pole figures (a) with associated inverse pole figure (b) and corresponding neutron transmission simulation for a copper sample with its RD aligned along the neutron beam (c), (d) map of sample rotated along the vertical axis, and (e) copper sample with its ND aligned along the neutron beam. .	102
5.6	<i>Sinpol</i> simulated copper texture ideal component pole figures (a) with associated inverse pole figure (b) and corresponding neutron transmission simulation for a copper sample with its RD aligned along the neutron beam (c), (d) map of sample rotated along the vertical axis, and (e) copper sample with its ND aligned along the neutron beam.	103
5.7	<i>Sinpol</i> simulated S texture ideal component pole figures (a) with associated inverse pole figure (b) and corresponding neutron transmission simulation for a copper sample with its RD aligned along the neutron beam (c), (d) map of sample rotated along the vertical axis, and (e) copper sample with its ND aligned along the neutron beam.	104
5.8	Ex-situ deformation rolling textures of Al-2%Mg alloy obtained at VULCAN neutron diffractometer (a) pole figures with associated inverse pole figure (b) and corresponding neutron transmission simulation for Al-2%Mg sample with its RD aligned along the neutron beam (c), and (d) Al-2%Mg sample with its ND aligned along the neutron beam.	107
5.9	Ex-situ recrystallization textures of Al-2%Mg alloy obtained at VULCAN neutron diffractometer (a) pole figures with associated inverse pole figure (b) and corresponding neutron transmission simulation for Al-2%Mg sample with its RD aligned along the neutron beam (c), and (d) Al-2%Mg sample with its ND aligned along the neutron beam. . .	108
5.10	Illustration of number grains contributing to [111] Bragg-edge for a copper sample.	109

5.11	Pole figures representing the filtering of orientation space in a copper sample, (a) [111] Bragg-edge, (b) [200] Bragg-edge, (c) [220] Bragg-edge, and (d) [311] Bragg-edge.	111
5.12	Comparison of simulated neutron transmission of Inconel-718 to neutron transmission measurement of Inconel-718.	113
5.13	Pole figures of (111), (200), (220) and (311) planes of the Inconel-718 sample with cube texture obtained by neutron diffraction texture measurements at VULCAN	114
5.14	Comparison of simulated neutron transmission of Inconel-718 sample with cube texture using ODF from <i>Sinpol</i> and MTEX and neutron transmission measurement of Inconel sample with cube texture as a function of sample rotation from 0 degrees to 90 degrees in 15 degrees	115
6.1	Coordinate system used to calculate strain in <i>Sinpol</i>	120
6.2	Simulation of neutron transmission spectra of single crystal Inconel 718.	122
6.3	Simulation results for single crystal Inconel 718 subject to uni-axial strains along the x direction.	124
6.4	Simulation results for single crystal Inconel 718 subject to uni-axial strains applied along the y direction.	124
6.5	Simulation results for single crystal Inconel 718 subject to uni-axial strains applied along the z direction.	124
6.6	Simulation results for single crystal Inconel 718 subject to bi-axial strains applied along the x and z direction.	125
6.7	Simulation results for single crystal Inconel 718 subject to hydrostatic strains.	126
6.8	Simulation results for single crystal Inconel 718 subject to uni-axial strains applied along the X direction.	127
6.9	Simulation results for single crystal Inconel 718 subject to uni-axial strains applied along the Z direction.	127

6.10	Simulation 111 Bragg-edge transmission spectra of powder Inconel 718 for four strain conditions.	129
6.11	Simulation 200 Bragg-edge transmission spectra for cube textured Inconel 718 for four strain conditions.	130
6.12	Simulation of 111 Bragg-edge under with 7000 $\mu\epsilon$ uniformly applied while sample is rotated from 0 to 90 degrees.	131
6.13	Simulation of 111 Bragg-edge under with 7000 $\mu\epsilon$ along the Y_1^S axis. At rotation angle of $\rho = 0$ degrees the strain is orthogonal to the neutron beam in compression and tension.	132
6.14	Simulation of 111 Bragg-edge under with 7000 $\mu\epsilon$ along the Y_3^S axis. At rotation angle of $\rho = 0$ degrees the strain is parallel to the neutron beam in compression and tension.	132
6.15	Simulation of 111 Bragg-edge under with 7000 $\mu\epsilon$ along the Y_3^S axis and 1000 $\mu\epsilon$ along the Y_1^S axis.	132
6.16	Simulation of neutron transmission of single crystal Inconel 718 peaks with 1000 Mpa stress applied along the beam direction.	137
6.17	Simulation of neutron transmission of powder Inconel 718 Bragg-edges with 1000Mpa stress applied along the beam direction.	141
6.18	Lattice strain distributions in the 316 stainless steel simulated with 111, 200, 220, and 311 as a function of tilt angle relative to the loading direction with applied stress 264.35 Mpa (Elastic), 315.23 Mpa (Plastic), 584.75 Mpa (Max Plastic), and 21.36 Mpa (residual).	145
6.19	Simulated lattice strain of the 111, 200, 220, and 311 Bragg-edge in the 316 stainless steel sample.	147

Nomenclature

τ	Reciprocal lattice vector
ϵ_{ij}	Strain tensor
γ	Neutron magnetogyric ratio
\hbar	Planck's constant
λ	Wavelength
$ f\rangle$	Final state of nucleus
$ i\rangle$	Initial state of nucleus
μ	Attenuation coefficient
μ_M	Magnetic moment
μ_N	Nuclear magneton
Ω	Solid angle
ϕ	Vertical Angle
Φ_N	Neutron flux
ψ	Tilting angle
Ψk_1	Scattered plane

Ψk_o	Incident plane
$\rho(E_1)$	Density of states
Σ	Macroscopic cross-section
σ_{abs}	Absorption cross-section
Σ_a	Macroscopic absorption cross-section
$\sigma_{coherent}$	Coherent cross-section
σ_{el}	Elastic cross-section
σ_{ij}	Stress tensor
$\sigma_{incoherent}$	Incoherent cross-section
σ_{inel}	Inelastic cross-section
Σ_{sd}	Macroscopic diffuse cross-section
Σ_s	Macroscopic scattering cross-section
σ_t	Total cross-section
\mathbf{k}	Scatter wave vector
\mathbf{k}_o	Incident wave vector
\mathbf{Q}	Scattering vector
\mathbf{v}	Velocity vector
θ	scattering angle
θ_B	Nominal Bragg scattering angle
Θ_D	Debye Temperature

a	Side of box
b	Scattering length
C_{ijkl}	Stiffness tensor
d_{hkl}	lattice spacing
e	Elementary Charge
E_1	Scattered energy
E_f	Final energy
E_o	Incident energy
F_τ	Unit cell structure factor
F_j	Force components
I	Final Intensity
I_o	Initial Intensity
K_B	Boltzmann's constant
L	Distance to detector
m_A	Nuclear mass
m_n	Neutron rest mass
m_P	Proton rest masss
N_c	Number of unit cell per volume
p_a	Probability of absorption
p_{ds}	Probability of diffuse scattering

p_i	Weight per state
p_s	Probability of scattering
s	Neutron spin
S_{ijkl}	Compliance tensor
S_j	Surface components of sample
t	Time
T_m	Moderator temperature
T_{tof}	Neutron time-of-flight
V	Interaction potential
V_o	unit cell volume
W	Debye factor
W_{k_0,k_1}	Probability
X_i	Sample coordinate
X'_i	Laboratory coordinate

Chapter 1

Introduction

Soon after the first demonstration experiment of neutron diffraction [1], the problem of neutron transmission through crystalline materials was first theoretically approached by Halpern, Hamermesh and Johnson [2]. However, the first experimental results were published only after the second world war by Fermi, Sturm and Sachs [3]. They reported the energy dependence of neutron transmission through polycrystalline Be and BeO, characterized by “violent fluctuations for small changes in the energy” (Bragg-edges). This behavior was successfully reproduced based on neutron coherent elastic scattering calculations pioneered by the previous authors [2]. As the main purpose of these initial works was to determine material properties accounting for the interaction with neutrons (impacting the reactor physics), some sources of errors have also been envisioned from the beginning: extinction and preferential orientation (crystallographic texture). Later, the neutron transmission through crystals and polycrystals became a concern of neutron optics, in high demand for the emerging neutron scattering field, in need of neutron monochromators and filters [4]. It is strange that the idea of using neutron transmission as a tool for materials studies was advanced only in the late 1980s by Bowman & Priesmeyer. With the advent of pulsed neutron sources, after pioneering real-time experiments at LANSCE [5], the neutron time-of-flight transmission method received a larger audience and benefited

from a sound theoretical background and software development [6]. Two seminal papers [7, 8], published at the beginning of the century, defined the field, followed by many others.

Simultaneously, the improvement in the technology of neutron detectors ensured a tremendous increase of spatial resolution and neutron imaging became a mainstream technique for neutron applications [9]. In this environment, the idea of using an energy dispersive method in neutron imaging was enthusiastically welcomed. A few demonstration studies, performed with a low spatial resolution, assessed the possibility of performing 3D imaging (tomography) of phase content [10] or strain [11] by analyzing the energy dependence of transmission images. Two efficient experimental approaches were developed soon after: (1) at steady-state research reactors, using double crystal monochromators [12] (13.5 μm spatial resolution and 3% wavelength resolution); and (2) at pulsed neutron sources, using the time-of-flight method [13] (55 μm spatial resolution and 0.4% wavelength resolution).

The complexity of obtaining tomographic information for strain, particle size and orientation are well documented within the literature. Woracek [14] has shown the feasibility of obtaining crystalline phases via energy-selective neutron computed tomography (CT). For strain tomography and texture analysis, the directional nature of these parameters results in a voxel within the sample having a cross section that varies with viewing direction, and as a result prevents the use of traditional CT reconstruction techniques that assume constant cross section for all orientations in the neutron beam. For further understanding of the transmission models and to create general CT capabilities, both measurements and simulations are needed.

The studies on attenuation of thermal and cold neutrons beams in large single crystals were inspired by the necessity of predicting the performance of neutron filters (see Adib [15] and references therein). In these studies, the crystals are

considered ideally imperfect (mosaic) and the reflecting power of each crystallographic plane is evaluated under a secondary extinction assumption [16] (Darwin equation). In fact, the reflectivity expressions used for crystal plates were first deduced by Bacon & Lowde [17] (in Bragg geometry) and Dietrich & Als-Nielsen [18] (in Laue geometry). The effect of diffraction on transmission was evaluated by subtracting the reflectivity from unity, and the other contributions to attenuation (absorption, inelastic scattering) were considered independently. However, the exact solutions of the Darwin equation for transmissivity through a single crystal plate were later reported by Sears [19], and it was shown that, in the Bragg geometry, the non-diffractive attenuation cannot be decoupled from the diffraction attenuation (anomalous absorption).

The neutron cross section modeling under a powder assumption [20] proved to be suitable for treating the transmission data in a similar way as the Rietveld approach [6], which is extensively used in powder diffraction. The Rietveld-type codes include extinction corrections [21] inspired by an earlier work of Sabine [22]. In this approach, only the primary extinction plays a role in polycrystalline materials and secondary extinction ‘has no meaning’, as ‘all orientations of mosaic blocks are present with equal probability’. Such an assertion is valid only if the number of mosaic blocks (coherent domains) per each grain is quite small; it may be true for brittle materials but not for metals, for which each grain includes significantly smaller blocks (usually well below 1 μm). In general, the primary extinction length exceeds a few μm even for the most powerful diffraction lines; this is why the primary extinction corrections are rarely used in neutron powder diffraction. The primary extinction corrections were automatically extended to the Rietveld-type transmission codes [23] and are used to estimate ‘grain size’ in ductile materials. On the other hand, the secondary extinction is clearly necessary to predict the neutron transmission through single crystals but is not considered for polycrystals. It is true that the secondary extinction length is usually in the submillimeter or millimeter range for normal diffractometer

arrangements, but it can reach μm values close to back reflection. Thus, as the secondary extinction length can become comparable to or less than grain size (tens of μm), there are instances when it should be considered in transmission, even for polycrystalline samples.

In his dissertation, Vogel [6] presented a summary of the advantages gained using the neutron transmission Bragg-Edge measurement technique for polycrystalline materials. Compared to the conventional diffraction technique Neutron Bragg-Edge experiments use a higher neutron flux which improves count statistics at the detector and shortens exposure time when compared to the conventional diffraction technique. This shortened exposure time can be used to resolve structural sample parameters as exemplified by [24] using a single neutron pulse to determine the (211) reflection position of steel.

The conventional approach to resolve the crystal structure of polycrystalline samples using X-ray or neutron diffraction is to measure a wavelength dependent intensity pinned at some angle to the direction of the beam. Under such a set up, a sizable percentage of neutrons remain unused as only a small percent of the solid angle is covered with detectors while the neutrons are scattered over the whole solid angle. A greater yield is ascertained with the neutron transmission set up which requires neutron source, sample and detector system placed on a single axis. The neutrons traveling through the sample without interaction are detected, and scattered neutrons that would be detected in a diffraction experiment leave a distinctive pattern in the incident intensity spectrum. There is no need for a precise alignment of the sample in this set up, unlike conventional diffraction experiment in which precise alignment is necessary. Furthermore, calibration procedures in neutron transmission experiments are very simple.

Preferred orientation (texture) in metals was first measured by Wever [25] in 1924 and later using pole figure measurements by Schultz [26]. Texture measurements are necessary to validate models which leads to understating of texture development during material processing. Utilizing X-rays or electrons for quantitative texture measurements of bulk materials requires careful sample preparation to minimize surface effects. In addition, corrections for absorption maybe required and this is generally cumbersome for large-grained samples. These issues are usually avoided when using neutrons for bulk texture measurements. Due to their low attenuation by most materials, neutrons penetrate deeply into most materials, making surface/sample preparation or absorption effects negligible in most cases. Both X-rays and neutrons use pole measurements followed by pole figure inversion for diffraction texture analysis, a similar approach can be taken to utilize the neutron transmission technique for texture analysis. Boin [20] in his dissertation focuses on the feasibility of quantitatively measuring crystallographic properties using the neutron Bragg-edge technique. His work includes the integration of the calculation of theoretical neutron cross section for crystalline samples into MCstas [27], a Monte Carlo program. He demonstrates for a fiber textured aluminum sample that neutron transmission measurements taken at ISIS and CONRAD can be used to quantitatively resolve the degree of texture for a given projection.

Similar to neutron diffraction strain measurement, neutron Bragg-edge strain measurement makes use of Bragg’s law to obtain the inter planar distance for the set of grains with lattices that are properly oriented to contribute to the diffraction intensity. This inter planar spacing can then be used as an intrinsic strain gauge by comparing the spacing of a stressed sample with that of an unstressed one. The transmission technique uses Bragg’s law to obtain the inter planar spacing of grains. Each Bragg-edge is directly related to a particular lattice spacing; therefore, a change in Bragg-Edge position corresponds to a change of the lattice spacing for the planes in the beam’s direction and enables the determination of strain in that direction. The error associated with the lattice spacing, d , from Bragg’s law is given by

$$d = \frac{\lambda}{2 \sin \theta} \Rightarrow \frac{\Delta d}{d} = \frac{\Delta \lambda}{\lambda} + \arctan \theta \Delta \theta$$

where λ is the neutron wavelengths and θ the Bragg angle. Since the precise location of the Bragg-edge is known to be at $\theta = 90^\circ$ and therefore $\Delta \theta = 0^\circ$, the error associated with the lattice spacing in a transmission experiment is

$$\frac{\Delta d}{d} = \frac{\Delta \lambda}{\lambda}.$$

Therefore, the lattice can be measured with greater precision than that of a diffraction experiment, which corresponds to a greater precision in strain measurement.

The neutron Bragg-edge technique was first demonstrated as a viable strain measuring technique by Santisteban [28] et al, and within the same year by Steuwer [10] et al. Santisteban and his colleagues used neutron transmission to measure the residual elastic strain around a cold expanded hole in a 12 mm thick steel plate (Fig 1.1). Seven years later, Abbey [29] et al were able to show that the projected strain can be resolved to perform strain tomography. Abbey [29] provided a method for extracting both the radial and hoop strain components via a direct reconstruction and matching of the measured average strain profile, in this sample the strain distribution is symmetric in both axis and is reduced to a one-dimensional problem. The same VAMAS plug sample(Figure 1.2) was simulated and measured by Boin [20] and the projected strain in the transmission direction was integrated into the Mcstas simulation, and the resulting simulation was able to predict the expected strain values for CONRAD and ENGIN-X. The experiment also shows the limitations of the Bragg-edge technique for strain, as the recorded strain is averaged through the thickness of the sample.

Neutron Bragg-edge strain measurements [30] [13] (Fig 1.3) and the methods provided by Abbey are proof of concept for Bragg imaging of strain with neutrons through an object in one direction. For general neutron diffraction strain tomography, the work of of Lionheart and Withers [31] demonstrates that strain reconstruction is

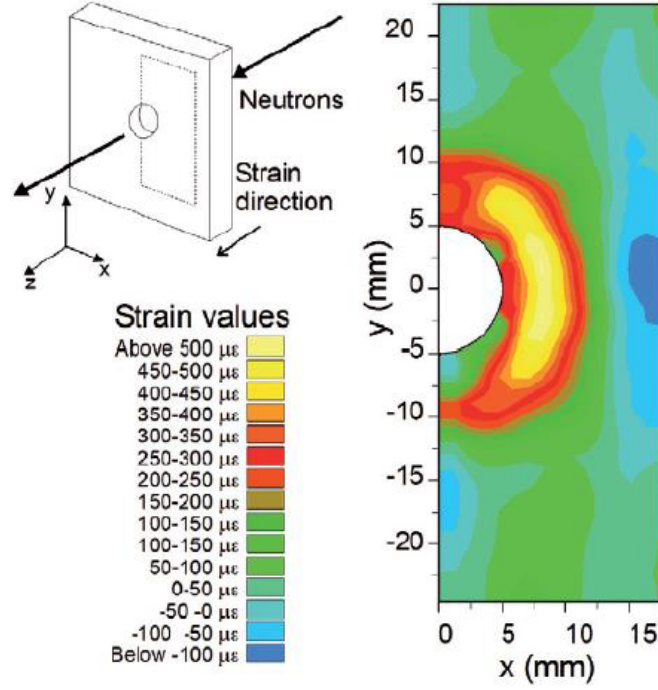


Figure 1.1: Transmission measurement at ISIS showing the residual elastic strain around a cold-expanded hole in a 12 mm thick steel plate. The measured strains correspond to the through thickness average of the out-of-plane strains. [28]

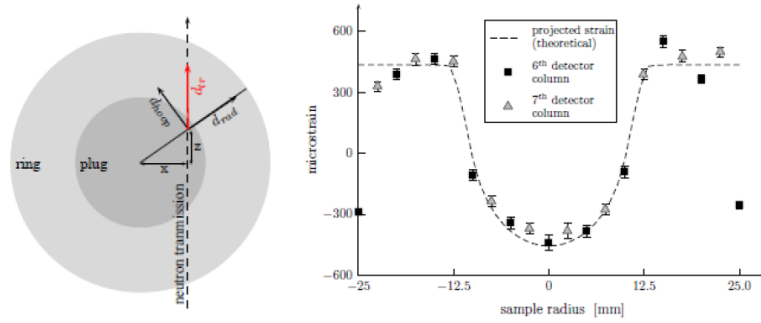


Figure 1.2: Neutron transmission probes the projected strain which for the ring and plug sample consists of a combination of hoop and radial strain components. (b) Projected strain as a function of sample radius and corresponding data collected at ENGIN-X. [20]

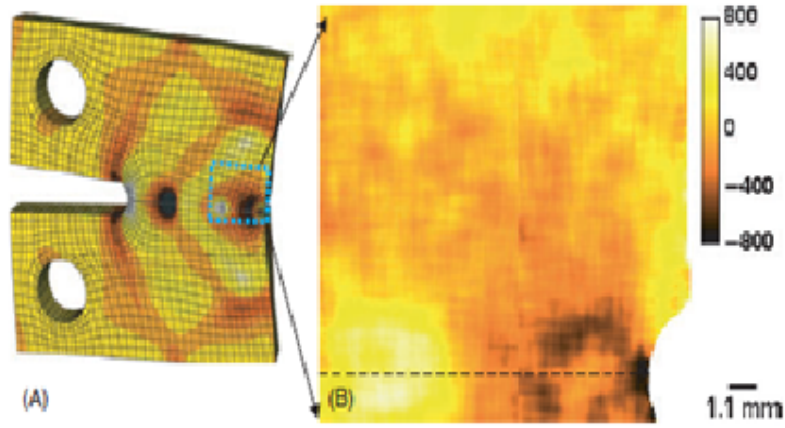


Figure 1.3: Comparison of strain map from modelling (left) and Bragg-edge imaging (right). [13]

not possible in the general sense; however, various special cases may exist. Wensrich [32] has outlined a process by which average triaxial elastic strain tomographic reconstruction is possible and has demonstrated [33] an approach for tomographic reconstruction of three-dimensional strain distributions from Bragg-edge neutron transmission strain images. The work of Abbey and Wensrich supports the feasibility of applying neutron strain tomography as a tool in the analysis of bulk residual elastic strain in material, and this could pave the way for the reconstruction of complex strain distributions in three dimensions. The behavior of Bragg-edges needs to be further studied as applied in three-dimensional neutron strain tomography. It is this work's goal to investigate the behavior of Bragg-edges under rotation when a three dimensional strain is present a material.

The remainder of this chapter is dedicated to presenting the basic properties of the neutron. The generation, moderation, and detection of the neutron are also described. Background of the strain and stress as it relate to this thesis is presented. The motivation for a new neutron transmission simulation engine is discussed and the chapter is finalized with an outline of the structure of this thesis.

1.1 Basic Properties of the Neutron

The neutron is a nuclear particle with a mass that is comparable to that of the proton. It is electrically neutral but it possesses a magnetic moment μ_M coupled antiparallel to its spin, which has the value $s = 1/2$

$$\mu_M = \gamma\mu_N \quad (1.1)$$

where $\gamma = -1.913$ is the neutron magnetogyric ratio and the nuclear magneton μ_N is given by

$$\mu_N = \frac{e\hbar}{m_P} \quad (1.2)$$

where e is the elementary charge, \hbar the reduced Planck constant, and m_P the proton rest mass.

Neutrons interact with matter in two ways, interaction with nuclei via the strong nuclear force and with magnetic moments via the electromagnetic force (which is not in the scope of this thesis). The interactions of neutrons with matter can be either scattering or absorption reactions. Both are described in terms of quantities known as cross section which are defined as the interaction rate per atom in the target per unit intensity of the incident beam [16]. A neutron can have many types of interaction with a nucleus, and each interaction with that nucleus is associated with a specific cross section. The sum of the cross-sections of all the capture reactions is known as the absorption cross section and is denoted by σ_{abs} . The elastic scattering is described by the elastic scattering cross section, σ_{el} , inelastic scattering by the inelastic scattering cross section, σ_{inel} . Both elastic cross section and inelastic cross section are summation of coherent and incoherent contributions. The summation of the elastic cross-section (σ_{el}), the inelastic cross-section (σ_{inel}), and the absorption-cross section (σ_{abs}) is the

total cross-section (σ_t), which is the probability that an interaction of any type will occur when neutrons strike a target.

$$\sigma_t = \sigma_{el} + \sigma_{inel} + \sigma_a \quad (1.3)$$

In this thesis, neutron transmission Bragg-edges are simulated by modeling the elastic coherent cross section, the neutron transmission background is simulated by modeling the absorption cross section and elastic incoherent cross section.

1.2 Neutron Generation

Neutrons are produced in a many ways. Naturally free neutrons are created in secondary radiation of cosmic radiation, and since neutrons are β active and have average halflife of 888s [34] [35], one may conclude that artificial sources of neutrons are necessary for studies in neutron science. Currently there are artificial sources that can be used to produce neutrons in the laboratory: radioisotope sources, photoneutron sources, accelerator sources, nuclear reactors, and spallation sources. Discussions concerning the first three sources are treated in reference [36], as for this work a brief discussion is presented on the research nuclear reactor and the spallation sources.

In nuclear reactors, neutrons are generated by a neutron induced nuclear fission process in which the nucleus captures a neutron and splits into two nuclei of approximately equal mass. In such research reactors, an assembly of ^{235}U alloy plates is used to release an average 2.5 neutrons for every fission event. The neutrons produced within that process have energies measured in MeV and have wavelengths that are too small to be used in neutron scattering experiments. A moderator comprised of hydrogenous material such as light water or heavy water is employed to slow down the neutrons from fission. The neutrons approach thermal equilibrium at the moderator's constant temperature. They form a Maxwellian wavelength

distribution appropriate to the moderator’s temperature. Modifying the moderator’s temperature changes the center of the distribution, such that neutrons with different energies can be provided for various types of neutron instruments [37] for experiment purposes.

At spallation sources, pulsed neutrons are produced when protons are accelerated to high energy and directed to a heavy metal target (e.g. liquid mercury at SNS). The protons are usually accelerated in bursts to 800Mev using a synchrotron and excite target nuclei to “boil off” neutrons and lighter particles in a “evaporation” process [38]. At the SNS, each incident burst produces a pulse of highly energetic neutrons (up to 2.5Mev) and 20 to 30 neutrons are “spalled” or thrown off dependent on proton energy. The source at the SNS produces peak neutron fluxes in the order of 10^{17} neutrons per second per cm^2 [39] which is currently the most powerful pulsed neutron source in the world. During the spallation process energy is consumed not released therefore the spallation process is not restricted to a few types of nuclides. In contrast to reactor sources, the provision of energy to be consumed is expensive; however, the process immediately stops as soon as the energy supply is switched off. This allows for the production of neutrons within practically any time structure and with more relaxed safety provisions which are not possible at reactor sources. In reactors a filter is required to separate the wavelengths necessary for spectral neutron measurements while in pulse sources the separation is achieved in time.

1.3 Neutron Moderation

As seen in the previous section, neutrons produced at both spallation sources and reactor sources have energies in the order of a few Mev which exceeds the energies necessary for studying atomic arrangements in solids. If used in investigations of atomic arrangements in solids, their velocity must be decreased such that their wavelength is in the order of inter-atomic distances [40]. The fast neutrons undergo many collisions within a moderating material (at SNS it is liquid mercury) and

achieve thermal equilibrium with their surroundings [41]. The maximum intensity is determined by the moderator's temperature T_m and is described by the following equation [42]:

$$E = k_B T_m \quad (1.4)$$

where K_B is Boltzmann's constant. The moderator temperature varies the center of energy distribution, such that neutrons with different energies can be provided for various types of neutron instruments. According to the energy of a neutron and its moderation, neutrons are usually classified by their temperature and named as cold, thermal and epithermal [43]. More energetic neutrons are classified by their velocities as fast or slow neutrons. Despite the lack of sharp division between neutron categories [44] [9], a classification table based on neutron energies is shown in Table 1.1.

1.4 Neutron Detection

The neutron has a mass but does not have an electric charge thus it cannot directly produce ionization in a detector and so it cannot be directly detected. This means that detectors must rely on the conversion of neutrons to charged particles which

Table 1.1: Classification of neutrons [45]

Name	Neutron energy
Cold	0-0.025ev
Thermal	0.025ev
Epithermal	0.025-0.4ev
Cadmium	0.4-0.6ev
EpiCadmium	0.6-1ev
Slow	1-10ev
Resonance	10-300ev
Intermediate	300 eV- 1Mev
Fast	1-20 Mev
Ultrafast	>20Mev

in turn can be detected electronically. The conversion involves an incident neutron interacting with a nucleus to produce a detectable charged particle. To detect thermal neutrons, scintillation counters or gas counters are used. Windsor [43] for example, presents an overview of the most important nuclear reactions for the detection of a neutron n , which are described by the following equations:

$$n + {}^3\text{He} \rightarrow {}^1\text{H} + {}^3\text{H} + 0.765\text{Mev} \quad (1.5)$$

$$n + {}^6\text{Li} \rightarrow {}^1\text{H} + {}^4\text{He} + 4.78\text{Mev} \quad (1.6)$$

$$n + {}^{10}\text{B} \rightarrow {}^7\text{Li} + {}^4\text{He} + 2.79\text{Mev}. \quad (1.7)$$

In ${}^3\text{He}$ gas proportional detectors, helium enriched with ${}^3\text{He}$ is placed in a metal cylinder with a thin wire anode that is positively charged and collects the electrons from the ionization process. The neutron is absorbed according to the exothermic reaction given by equation 1.5, while the detected charge is measured as a function of the anode voltage. In scintillation counters, the neutron is absorbed by one of the exothermic reactions described by equations 1.6 and 1.7 and followed by fluorescent radiation which is a by product of the emitted charged particle ionizing the working media. The emitted light can be detected by high sensitivity Charge Coupled Devices cameras, whose electrical signals are used to capture a two-dimensional picture. In the case of time of flight neutrons, photomultipliers coupled with fiber optics are used to amplify the current produced by the incident light.

1.5 Neutron Wavelength

The wavelength of neutrons used at nuclear reactor sources are typically monochromatized by diffracting a single crystal with controlled orientation in the incident neutron

beam. Given scattering angle θ_B , the reflected neutrons will have wavelengths obeying Bragg's law;

$$n\lambda = 2d_{hkl} \sin \theta_B \quad (1.8)$$

where λ is the neutron wavelengths and d_{hkl} is the interplanar distance within the crystal. This process requires multiple detectors and collimators, and many different angles typically have to be probed.

At spallation sources the time (T_{OF}) of flight technique is used. This technique assumes that the time T_{OF} it takes for a neutron to travel from the emission point to a given distance L to the detector location. From the de Broglie-relation $p = \hbar k$ the neutron wavelength can be written as

$$\lambda = \frac{hT_{OF}}{m_n L} \quad (1.9)$$

For a diffraction experiment the TOF is given as:

$$T_{OF} = \frac{2m_n d_{hkl} \sin \theta_B L}{h} \quad (1.10)$$

The interplanar spacing of the specimen is obtained by holding the scattering angle $2\theta_B$ fixed at the detector and scanning the wavelengths. The reflected neutrons will have energies

$$E_n = \frac{n^2 \hbar^2}{8m_n d_{hkl}^2 \sin^2 \theta_B}. \quad (1.11)$$

Since the reflected intensity is inversely proportional to the energy, the higher-order reflections have lower intensities. It follows then that the intensity of the n th reflection will be lower by a factor of n^2 than the first-order intensity. Additionally the first order reflection usually involves thermal neutrons near the maximum of the incident spectrum, while neutrons corresponding to higher reflection orders lie in the tail of the Maxwellian distribution, with a corresponding reduction in their relative intensity [16].

1.6 Neutron Strain Measurements

Residual stresses in engineering material or solid material are stresses present in the absence of an external force. Typical sources of residual stresses are machining, heat treatment and the welding process. Heat treatment/welding are processes that create phase change and structural deformation of a component. The residual stress of material can arise from those manufacturing processes which imparts permanent inhomogenous deformation into a material [38].

It is commonly accepted that residual stresses can be classified into three distinct categories based on the range of coverage within the material [46] [47] [48]. Residual stresses are referred to as type I, type II and type III residual stress. Type I residual stresses are homogeneous over large areas of several grains of a material, they are equilibrated with a distance that is comparable with the macroscopic dimension of the sample. These are known as macrostresses. Type II residual stresses were termed “pseudo-macro stresses” by Cullity [49]. They are homogenous within a small domain of a grain or phase of a material and are equilibrated over a distance that is comparable to the grain domain. They occur due to small scale anisotropy in the material, for example the mismatch in coefficient of thermal expansion (CTE). Type III residual stresses are homogeneous over a few interatomic distances, the smallest crystal domain of a material. Both types II and III are known as microstresses [50].

In engineering materials, the residual stress state at a point comes from the superposition of the macrostresses and microstresses [51] [52] [53] [54], and is described by a symmetric second-rank tensor σ_{ij} :

$$\sigma_{ij} = \sigma_{ji} = \frac{\partial F_i}{\partial S_j} = \begin{pmatrix} \sigma_{11} & \sigma_{12} & \sigma_{13} \\ \sigma_{21} & \sigma_{22} & \sigma_{23} \\ \sigma_{31} & \sigma_{32} & \sigma_{33} \end{pmatrix} \quad (1.12)$$

where F_i are the components of the force in the X_i direction that act on the volume attributed to the surface S_j .

All techniques of stress measurement whether applied or residual rely on the measurement of the strain in the material. Strain measurements are classified as either destructive or non-destructive. Destructive strain measurements are based on the release of the macro-strain by drilling, cutting shaving or chemical milling the sample, while non-destructive strain measurement leaves the sample stress state unperturbed. The stress measurement is reliant on some of the intrinsic properties of the material. Among non-destructive methods, X-ray diffraction and neutron diffraction use the inter-planar atomic spacing as a strain gauge. The sample to be measured is illuminated usually with a monochromatic beam with wavelength comparable to that of the atomic spacing. Using Bragg's law (equation 1.8), the strain along the reciprocal lattice vector hkl , with knowledge of a stress-free lattice parameter d_o^{hkl} , and the strain $\epsilon_{\phi\psi}^{hkl}$ is acquired by the following equation:

$$\epsilon^{hkl} = \frac{d_{\phi\psi}^{hkl} - d_o^{hkl}}{d_o^{hkl}} \quad (1.13)$$

where $d_{\phi\psi}^{hkl}$ is the lattice spacing determined by the Bragg angle θ and the wavelength λ in case of an angle and energy dispersive mode respectively. With reference to a sample coordinate system, the measurement direction of the strain value $\epsilon_{\phi\psi}^{hkl}$ is defined by the azimuth angle ϕ and the tilt angle ψ as demonstrated in Figure 1.4.

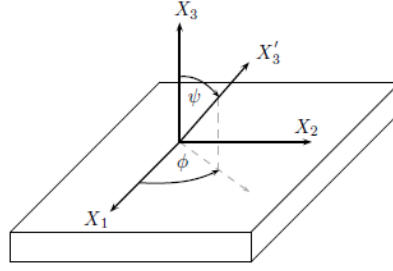


Figure 1.4: Coordinate system used to measure strain with diffraction. The laboratory coordinate system X'_i is related to the sample coordinate system X_i by the orientation angles ψ , ϕ .

This value is a component of the strain tensor, $\epsilon_{ij}(\mathbf{r})$, which depends on the sample's coordinate system, \mathbf{r} , and for elastic strain is connected to the stress tensor by Hookes law [53]:

$$\epsilon_{ij} = S_{ijkl}(\mathbf{r})\sigma_{kl}(\mathbf{r}) \quad (1.14)$$

where $S_{ijkl}(\mathbf{r})$ is the local compliance tensor, which can vary both inside the grain and at the grain boundaries. For isotropic polycrystal consisting of isotropic grains, averaging over the coordinate establishes the ratio between the average strain in the sample, $\epsilon_{ij} = \langle \epsilon_{ij}(\mathbf{r}) \rangle$ the evaluated macroscopic stress $\langle \sigma_{kl} \rangle$, and the compliance tensor S_{ijkl} .

1.7 Grain-Interaction Models

The relationship between the stress and the strain inside each grain is described by Hooke's law. Bragg-edges or Bragg peaks are formed by the signals coming from a number of grains within a distribution, and each grain within that distribution is subjected to a different microscopic strain or microscopic stress which differ from the macroscopic values to be measured. Hence the relationship between the

strain, $\epsilon_{ij}(\phi_1, \Phi, \phi_2)$, where ϕ_1, Φ and ϕ_2 are Euler angles defined in chapter 3; on a single grain having orientation $g(\phi_1, \Phi, \phi_2)$ and the macroscopical average stress $\langle \sigma_{ij} \rangle$ have to be established. This relationship will help to find the dependence between macroscopic stress in a sample and measured experimentally by neutron diffraction strain. Within the framework of linear elasticity theory, this relationship is expressed in equation 1.14. The elastic behavior in a polycrystal sample is dependent on the elastic constant of the single crystal and also the interaction between each grain. Historically several models [55, 56, 57, 58, 59] have been proposed to study the elastic response in materials, in the section a review of the Voigt model, Reuss model, and Hill model is presented.

1.7.1 Voigt Model

The grain interaction model proposed by Voigt [55] assumes that each grain develops the same strain ϵ_{ij} independent of its orientation. As a result, the microscopic strain for a single grain is equal to the macroscopic strain $\langle \epsilon_{ij} \rangle$ averaged over the entire sample :

$$\epsilon_{ij} = \langle \epsilon_{ij} \rangle \quad (1.15)$$

and thus is related to the stress tensor in grains with orientation g by

$$\sigma_{ij}(g) = C_{ijkl}(g) \langle \epsilon_{kl} \rangle \quad (1.16)$$

where $C_{ijkl}(g)$ is the stiffness tensor of grains with orientation g in the sample coordinate system. To determine the average stress tensor, equation 1.16 has to be averaged over all grains with orientation g within a distribution of grains. The Voigt [55] model is a fairly rough approximation of grain interaction. The strains are continuous at the boundaries of grains; however, the stresses suffer from the discontinuity. The totally opposite situation occurs in a Reuss [56] model.

1.7.2 Reuss Model

Unlike the Voigt [55] model, the Reuss [56] model assumes all grains have the same stress σ_{ij} independent of orientation, resulting in the microscopic stress of a single grain being equivalent to the macroscopic stress averaged over the whole sample

$$\sigma_{ij}(g) = \langle \sigma_{ij} \rangle \quad (1.17)$$

and the strain tensor of a grain with orientation g is :

$$\epsilon_{ij} = S_{ijkl}(g) \langle \sigma_{kl} \rangle \quad (1.18)$$

where $S_{ijkl}(g)$ is the compliance tensor of grains with orientation g the sample coordinate system. To determine the average strain tensor, equation 1.18 has to be averaged over all grains with orientation g within a distribution of grains. In this model, the stresses are continuous at the grain boundaries while the strains are discontinuous.

1.7.3 Hill Model

The Voigt and Reuss model calculate the upper and lower bounds of the elastic moduli respective, the actual value lies in between the two. Hill [58] proposed that the average of the elastic moduli predicted by the two aforementioned model would provide satisfactory values for most material. For grains with crystal cubic symmetry, the Voigt compliance S_{ijkl}^V is the average of the local compliance C_{ijkl} and can be written as

$$C_{ijkl}^V = \langle C_{ijkl} \rangle \quad (1.19)$$

and the Reuss average stiffness can be expressed as the inverse of the average of the compliance tensor

$$C_{ijkl}^R = \langle S_{ijkl} \rangle^{-1}. \quad (1.20)$$

Following Kisi [60], the Hill estimate is the arithmetic average of the Voigt and Reuss averages and can be written as

$$c_{ijkl}^H = \frac{1}{2}(c_{ijkl}^V + c_{ijkl}^R). \quad (1.21)$$

Finally the strain in Hill's estimation can be expressed as

$$\langle \epsilon_{ij} \rangle^H = \frac{1}{2} \left(\langle \epsilon_{ij} \rangle^V + \langle \epsilon_{ij} \rangle^R \right). \quad (1.22)$$

Equation 1.22 is an average which works well for samples with relative low anisotropy, for sample with large anisotropy a weighted value is introduced into equation 1.22.

1.8 Why Another Bragg-Edge Simulation Package

The cost of neutron experiments are quite high, so it is customary to have a software package that simulates the measurement to be undertaken. The simulations are often used to help with experiment preparation and to calculate neutron interaction cross-sections that can be used in refinement and fitting routines to achieve consistent results. Since there are several well-established neutron cross-section calculation programs, it might be worth investigating the possibility of repurposing an existing package for this work's goal. The current state of the art neutron Bragg-edge simulation packages revolve around polycrystalline material. One of the more prominent codes is Cripo [61], a command line FORTRAN program written in 1977 which calculates the neutron cross section for a mono-atomic system. A more recent program, BETMAN [6], allows multiple atoms cross-sections calculation; however, it

is a Rietveld Bragg-Edge fitting package which requires the value of each cross-section calculated to be exported to a text file. The more complete nxs library developed by [62] is a collection of routines for calculating neutron scattering and absorption cross sections on the basis of crystal structure. The nxs library makes a crude calculation of texture using the March-Dollase approximation, and also calculates the cross-section with strain added. However, this strain calculation is made uniformly in all directions. All these calculations assume a powder approximation to study Bragg-Edges under rotation while a material is being stressed. A new simulation would have to move away from the powder assumption and cross-section calculation to encompass physics that include grain size, mosaic distribution per grain, unique grain orientation distributions, and general strain models on these grain systems. A new simulation also needs to include studies of voxel size versus the grain size (Chapter 4) to evaluate spatial resolution. Furthermore, the new simulation moves away from the basic assumption of the Bragg-edge analysis technique, that the material is a powder made of many, small, and randomly oriented grains. In this sense, the model presented in this work would allow the use of energy-resolved neutron transmission for the analysis of oligocrystals (Chapter 4) (materials composed by a relatively small number of crystals).

1.9 Structure of Thesis

Chapter 2 describes the general aspects of the neutron scattering by assemblies of nuclei in solids. The theoretical basis of the diffraction of neutrons by crystalline matter is discussed. The attenuation of thermal neutrons by a crystalline solid is described using an additive formula. The main terms of the formula are: Thermal Diffuse Scattering, Bragg Scattering. Chapter 3 describes the implementation of the neutron transmission calculation into a simulation tool called *Sinpol*. Chapter 4 presents comparisons of neutron transmission simulation results to data published in literature and to experimental data, studies of extinction effect on neutron

transmission intensities of single crystal and polycrystal, and studies of the effects of the distribution of grain size within a voxel. Chapter 5, shows simulation examples of preferred orientation (texture) on neutron transmission for several texture components. In chapter 6, the effect of strain on single crystal and polycrystal neutron transmission is considered, a calculation to simulate the movement of Bragg-edges is presented, and simulations of the effect rotation on a strained sample are studied for the purpose of computed tomography. The chapter is finalized by considering a phenomenological model to describe the effect of plastic deformation on lattice strains. Finally, chapter 7 gives a conclusion, and a discussion of future work.

Chapter 2

Neutron Interaction with Crystalline Material

The theory of neutron diffraction, like the theory of x-ray diffraction, is well developed in the kinematic and dynamic limits. In the kinematic limit, the crystal is treated as a perturbation and the diffracted intensities are valid for only sufficiently small crystals. Current Bragg-edges simulations make use of the kinematical approach by assuming the polycrystal material is made up of many small, randomly oriented grains. The transmission is then calculated using the Beer-Lambert law given below

$$I = I_0 e^{-n\sigma_t t} \tag{2.1}$$

where n is the number of atoms per cubic centimeter, t is the effective thickness of the crystal, and σ_t is the total cross section determining the neutron attenuation by the crystalline solid being illuminated. The quantity, σ_t , depends on the scattering lengths of the elements in the sample and structural information can be derived from elastic coherent scattering (also known as Bragg-scattering). In this chapter, a review of the scattering cross section for crystalline material is presented in the limit of the kinematic theory. In the case of a large ideal crystal, multiple scattering of the

incident wave have to be considered and this problem have been treated with the dynamic theory by Darwin [63], Ewald [64] and Von Laue [65]. For large imperfect mosaic crystals which are considered in this work, the neutron transport equations are presented to derive the Darwin differential equations for mosaic crystal. The chapter is finalized with a discussion of attenuation of neutron by crystals.

2.1 Neutron Interaction with Matter

2.1.1 Nuclear Cross Section

To mathematically describe the interaction of a neutron with a nucleus, a neutron with an initial wave vector \mathbf{k}_0 and a De Broglie wavelength of $2\pi/k_0$ is considered. After interaction with a nucleus, the neutron's wave vector has been changed in both direction and magnitude. The neutron is scattered. The scattering vector Q is defined by a difference between the neutron's initial wave vector \mathbf{k}_0 and the neutron's new wave vector after scattering \mathbf{k}_1 as shown in Figure 2.1. The basic quantity measured in a neutron scattering experiment is the partial differential cross section

$$\frac{d^2\sigma}{d\Omega dE_1}. \quad (2.2)$$

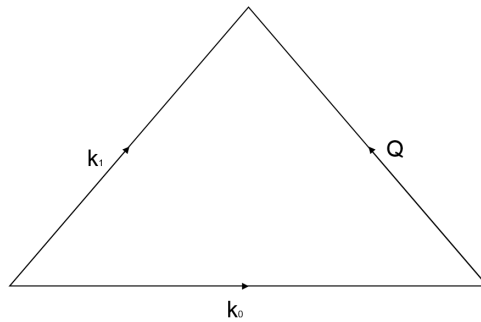


Figure 2.1: The relationship between the incident wavevector k_0 , the final wavevector k_1 , and the scattering vector \mathbf{Q} .

2.1.2 Elastic Cross Section

The partial differential cross section gives the fraction of neutrons of incident energy E_o and wave vector \mathbf{k}_0 scattered into an element of solid angle $d\Omega$ with an energy between E_1 and E_1+dE_1 and with wave vector \mathbf{k}_1 . The incident and scattered neutron states are represented by the two plane waves $\Psi_{\mathbf{k}_0}$ and $\Psi_{\mathbf{k}_1}$. The direction of propagation of the scattered neutron is determined by the angles θ and ϕ as shown in Figure 2.2. When energy is not transferred into the material, the fraction of neutrons scattered in the solid angle $d\Omega$ is describe by the differential cross section $d\sigma$. The differential cross section is determined by Fermi's Golden Rule which gives the probability per unit time of a transition for a neutron state described by $\Psi_{\mathbf{k}_0}$ to a final neutron state $\Psi_{\mathbf{k}_1}$ due to interaction of a potential V which cause the transition.

$$d\sigma = \frac{W_{\mathbf{k}_0, \mathbf{k}_1}}{\text{incident flux}}. \quad (2.3)$$

The differential cross section is directly proportional to the probability of transition $W_{\mathbf{k}_0, \mathbf{k}_1}$ which can be derived from number of quantum mechanic books [66] [67] [68] [69]. The initial and final state are denoted in the bracket notation is $|i\rangle$ and $|f\rangle$

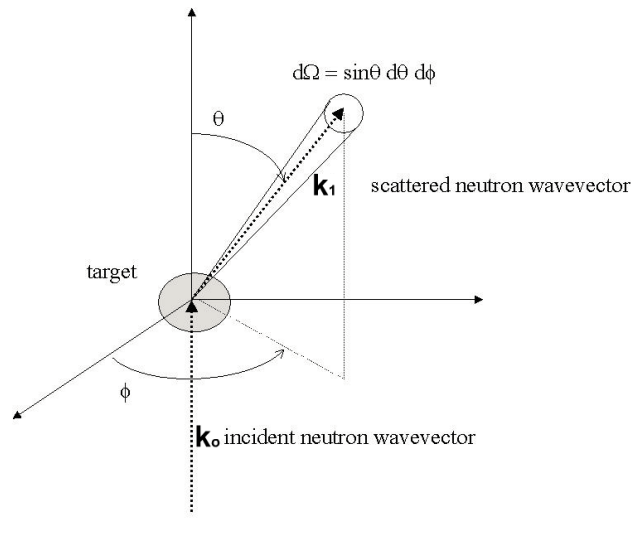


Figure 2.2: Geometry of scattering.

respectively. The case of the neutron plus the nucleus can then be represented as $|\mathbf{k}_0 i\rangle$ and $|\mathbf{k}_1 f\rangle$. This means Fermi's Golden rule can be written as:

$$W_{\mathbf{k}_0, \mathbf{k}_1} = \frac{2\pi}{\hbar} |\langle f \mathbf{k}_1 | V | \mathbf{k}_0 i \rangle|^2 \rho_{\mathbf{k}_1}(E_1) \quad (2.4)$$

The density of states per unit energy range is $\rho_{\mathbf{k}_1}(E_1)$. Estimating a small interaction between the neutron and nucleus, the Born approximation is used to write the initial and final state of the system in terms of the individual part of the neutron and the system, hence $|\mathbf{k}_0 i\rangle$ is written as $|k_o\rangle|i\rangle$ and $|\mathbf{k}_1 f\rangle$ as $|k_1\rangle|f\rangle$. $|k_o\rangle$ and $|k_1\rangle$ are eigenfuctions of the momentum operator and therefore can be normalized (see [66] for details). Assuming the neutrons are confined to a box of volume a^3 the density of states is

$$\rho_{\mathbf{k}_1}(E_1) = \left(\frac{a}{2\pi}\right)^3 \frac{mk_1}{\hbar^2} d\Omega \quad (2.5)$$

and the differential cross section is given as

$$\frac{d\sigma}{d\Omega} = \frac{W_{\mathbf{k}_0, \mathbf{k}_1}}{\Phi_N} = \left(\frac{a^3 m}{2\pi \hbar^2}\right)^2 \left| \int \Psi_{\mathbf{k}_1}^*(\mathbf{r}) V \Psi_{\mathbf{k}_0}(\mathbf{r}) d\mathbf{r} \right|^2 = |\langle f | V | i \rangle|^2. \quad (2.6)$$

2.1.3 Scattering Length

The neutron nucleus interaction is governed by the strong nuclear force. This force is known to be short range with maximum interaction distance for order 10 times less than the nuclear radius and much less than the neutron wavelengths used in scattering [70]. The scattering is considered to be isotropic and characterized by a single parameter b , called the scattering length. The Fermi pseudo potential is used describe the interaction between the neutron and the nucleus sitting fix at \mathbf{R}_j .

$$V = \sum_j \left(\frac{2\pi \hbar^2}{m}\right) b_j \delta(\mathbf{r} - \mathbf{R}_j) \quad (2.7)$$

The scattering length can be a complex quantity and its value depends on the particular nucleus involved in the scattering and on the relative orientation of the neutron and the nuclear spin (if it exists) [70]. The scattering length of different isotopes belonging to the same atomic species can have different values. The imaginary part of b represents absorption by the nucleus. Inserting 2.7 into 2.6, the differential cross section is

$$\frac{d\sigma}{d\Omega} = |b|^2 \quad (2.8)$$

and the total cross section

$$\sigma = 4\pi |b|^2. \quad (2.9)$$

2.1.4 Interaction with Crystals

A crystal can be described by a lattice with a group of atoms allocated at every lattice point. Consider this rigid array of N nuclei with each nucleus sitting at \mathbf{R}_l . The differential scattering cross-section of a rigid crystal lattice (i.e. thermal motion of the nuclei is neglected for now) is given by [71] [72] [73]

$$\frac{d\sigma}{d\Omega} = \left(\frac{d\sigma}{d\Omega} \right)_{coherent} + \left(\frac{d\sigma}{d\Omega} \right)_{incoherent} \quad (2.10)$$

where the coherent scattering cross-section $(d\sigma/d\Omega)_{coherent}$ represents interference between the waves scattered from each nucleus

$$\left(\frac{d\sigma}{d\Omega} \right)_{coherent} = |\langle b \rangle|^2 \sum_l e^{i\mathbf{Q}\cdot\mathbf{R}_l} \quad (2.11)$$

\mathbf{Q} is the momentum transfer of the incident neutron to the scattered neutron, $\langle b \rangle$ is the average scattering length of the contributing nuclei. The sum runs over l which is all the possible lattice vectors. The elastic coherent scattering will provide

information about the mutual arrangement of the atoms only due to the phase factor [74]. If \mathbf{Q} is not equal to the reciprocal lattice vector $\boldsymbol{\tau}$, the differential cross section will have values that are negligible, however the differential neutron cross section for a Bravais lattice can be written as

$$\left(\frac{d\sigma}{d\Omega}\right)_{coherent} = N \frac{(2\pi)^3}{V_0} |\langle b \rangle|^2 \sum_{\boldsymbol{\tau}} \delta(\mathbf{Q} - \boldsymbol{\tau}) \quad (2.12)$$

where the δ function implies that scattering occurs only for $\mathbf{Q} = \boldsymbol{\tau}$. This condition allows to determine possible \mathbf{Q} graphically with the so-called Ewald construction [75]. The reciprocal lattice vectors $\boldsymbol{\tau}$ are orthogonal to the corresponding Miller reflection planes with distance $d_{hkl} = \frac{2\pi}{|\boldsymbol{\tau}_{hkl}|}$. From this and by using Figure 2.1 the derivation of Bragg's law is possible. The elastic coherent scattering by rigid lattice is also referred to as Bragg scattering. In the general case of more than one atom per unit cell, $\langle b \rangle$ is replaced by the unit structure factor $F_{\boldsymbol{\tau}}$

$$F_{\boldsymbol{\tau}} = \sum_{\mathbf{m}} \langle b_{\mathbf{m}} \rangle e^{i\boldsymbol{\tau} \cdot \mathbf{x}_m} \quad (2.13)$$

which adds the fractions of the scattering amplitude of all the atoms in the unit cell. Where \mathbf{x}_m is the position vector of the m^{th} atom in the unit cell, and is commonly expressed as fractions of the unit cell edge. The final expression for the differential elastic coherent neutron cross section is :

$$\left(\frac{d\sigma}{d\Omega}\right)_{coherent} = N \frac{(2\pi)^3}{V_0} \sum_{\boldsymbol{\tau}} \delta(\mathbf{Q} - \boldsymbol{\tau}) |F_{\boldsymbol{\tau}}|^2. \quad (2.14)$$

The incoherent elastic scattering cross section $(d\sigma/d\Omega)_{incoherent}$ is isotropic and yields a constant background and is given by:

$$\left(\frac{d\sigma}{d\Omega}\right)_{incoherent} = N (\langle |b|^2 \rangle - |\langle b \rangle|^2). \quad (2.15)$$

2.1.5 Inelastic Cross Section

Again, the partial differential cross-section is used to described the inelastic scattering cross section. The neutron energy change is usually denoted by $\hbar\omega$. The state of the system is denoted by the symbols i and f , its energy is E_i and E_f and the state of the neutron and sample system is represented by a $|k_0 i\rangle$ and $|k_1 i\rangle$. The partial differential cross-section is approximated by applying the perturbation theory and the following average is obtained:

$$\frac{d\sigma}{d\Omega dE_1} = \frac{k_1}{k_0} < \sum_{f,i} p_i | \langle k_1 f | V | k_0 i \rangle |^2 \delta(\hbar\omega - E_f + E_i) \quad (2.16)$$

where p_i is a weight for the state $|i\rangle$. The partial differential cross-section will later be recalled as the inelastic processes due to the vibration of the atoms in crystals.

2.1.6 Absorption Cross Section

The last process that reduces the number of neutrons that are forward scattered by a system of N nuclei, is determined by the absorption cross-section [76] and is expressed as function wavelength number k and the imaginary part of the coherent length b

$$\sigma_{abs} = -N \frac{4\pi}{k} \text{Im}\{b\}. \quad (2.17)$$

A collection of neutron cross-section and scattering lengths has been compiled by Sears and published in Neutron News [19] and [77]. I have used them as a input in the neutrons code in order to be able to calculate cross sections by crystals.

2.1.7 Diffraction of Neutrons by a Polycrystalline Element

A polycrystal element contains a random distribution of crystals, therefore neutrons are scattered in all possible directions. The total scattering cross cross section σ_t is obtained by integrating equation 2.10 over all the possible angles in space. The total

incoherent cross section part is an integration of equation 2.15 and is given by :

$$\sigma_{incoherent} = 4\pi N \left(\langle |b|^2 \rangle - |\langle b \rangle|^2 \right). \quad (2.18)$$

The total number of neutrons that are scattered coherently over all angles in the case of a polycrystal sample is obtained via the integration of equation 2.11 and following [78]. The total coherent scattering cross section over all possible angles is given by:

$$\sigma_{coherent} = \frac{\pi N_c}{2k^2} \sum_{hkl} 4\pi F_{hkl}^2 d_{hkl} \quad (2.19)$$

the summation runs over all the planes capable of giving Bragg reflection for the neutron energy used, in terms of wavelength for all planes that have spacing $d_{hkl} \geq \lambda/2$. N_c is the number of unit cells per volume N/V_o . F_{hkl}^2 is the square of the structure factor of the unit cell for the (hkl) Bragg reflection and is given by:

$$F_{hkl}^2 = \left| \sum \langle b \rangle \exp \left[2i\pi \left(\frac{hx}{a} + \frac{ky}{b} + \frac{lz}{c} \right) \right] \right|^2. \quad (2.20)$$

Turning attention back to equation 2.19 and replacing the wave number with $2\pi/\lambda$, the elastic coherent neutron cross section can be written in the alternative form as:

$$\sigma_{coherent} = \frac{N_c \lambda^2}{2} \sum_{d_{hkl} \geq \lambda/2} F_{hkl}^2 d_{hkl}. \quad (2.21)$$

From equation 2.18 and equation 2.21 the total neutron cross section for polycrystal material can be written as derived by Bacon [40]:

$$\sigma_t = \frac{N_c \lambda^2}{2} \sum_{d_{hkl} \geq \lambda/2} F_{hkl}^2 d_{hkl} + 4\pi N \left(\langle |b|^2 \rangle - |\langle b \rangle|^2 \right). \quad (2.22)$$

At very short wavelengths, which are comparable to inter-atomic separations, it can be shown that the coherent scattering cross section is isotropic and for each atom is

equal to 2.9. At wavelengths longer than the cut-off wavelength ($\lambda > 2d_{max}$), the coherent cross section goes to zero.

Following Guerich and Tarasov [79], Figure 2.3 presents the behavior of the scattering cross section of a rigid lattice as a function of neutron energy. In the region below the Bragg cut-off energy or the minimum energy E_{min} , the incoherent part of the cross section dominates while the coherent part of the cross section does not contribute. The distinct peaks found at energies above the Bragg energy are gradually decreasing as lattice distances for new families of crystal planes are included in the scattering process. This is due to the presence of the $\frac{1}{k^2}$ factor as illustrated by the broken curve in Figure 2.3. At very large neutron energies and wavelengths less than the inter-atomic distance of the crystal the cross section tends to the limit $4\pi(b_{coherent}^2 + b_{incoherent}^2)$ [40]. At very small neutron energies and wavelengths beyond the cut-off wavelength, the total scattering reduces to $\sum \sigma_{incoherent}$.

2.1.8 Debye Waller Factor

The discussion thus far has assumed a rigid lattice with each nuclei having infinite mass (no recoil). Under those assumptions the scattering process corresponds to a classical elastic collision of a particle with a wall, without the possibility of energy transfer between the neutron and the target nucleus. We can now generalize the results given in the preceding section to the case of elastic scattering of neutrons by

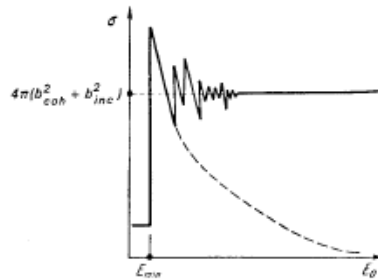


Figure 2.3: Total scattering cross section for a rigid lattice [79].

a real crystal, in which the nuclei are not infinite, and instead of being rigid in their atomic sites; they oscillate because of their thermal energy.

For evaluation of elastic scattering, the generalized form found in 2.10 is rewritten to include the Debye-Waller factor to take crystal vibrations into account

$$\frac{d\sigma}{d\Omega} = \left(\frac{d\sigma}{d\Omega} \right) e^{-2W}. \quad (2.23)$$

The factor e^{-W} , also known as thermal factor in X-ray scattering is given by

$$e^{-2W} = \exp \left[-4 \sin^2 \left(\frac{\theta}{2} \right) \frac{\langle u^2 \rangle}{\lambda^2} \right] \quad (2.24)$$

where $\langle u^2 \rangle$ is the mean square deviation of the lattice nuclei as a result of thermal vibrations, and θ the scattering angle. The Debye-Waller factor is observed as a reduction in scattering intensity due to the lattice vibrations and at given scattering angle θ . The Debye factor decreases as the temperature increases.

For crystals containing one atom per unit, [80] showed that W may be evaluated in the Debye model for specific heat of solids, and that the coherent scattering amplitude is reduced by the factor e^{-W} , where W is

$$W = \frac{6h^2}{m_A k_B \theta_D} \frac{\sin^2 \theta}{\lambda^2} \left[\frac{\phi(x)}{x} + \frac{1}{4} \right]. \quad (2.25)$$

Here h is Planck's constant, m_A is the nuclear mass, k_B is Boltzmann's constant, θ is the scattering angle, θ_D is the Debye temperature of the crystal, and the variable x is defined as $\frac{\theta_D}{T}$, where T is the absolute temperature of the measurement environment, and $\phi(x)$ is given by

$$\phi(x) = \frac{1}{x} \int_0^x \frac{\xi}{e^{-\xi} - 1} dx. \quad (2.26)$$

The effective coherent neutron scattering amplitude which contributes to the Bragg diffraction peaks is written as be^{-W} , where b is previously defined and takes into account the various isotopes, their abundance and nuclear spins [40].

2.2 Neutron Transport Equation in Mosaic Crystals

Two theories are widely used to describe the intensities observed in neutron diffraction by crystals: the kinematic theory and dynamic theory. Current neutron Bragg-edge transmission codes use the kinematic approach to calculate the neutron transmission intensity. The basic kinematic approach, which is also used in powder diffraction, assumes that the neutron wave outside the sample has the same amplitude as the incident neutron waves interacting with nuclei inside the sample [71]. The scattering intensity is assumed to be small enough to be considered a minor contribution to the neutron wave inside the sample and equals to the intensity of the neutron beam outside of the sample. The attenuation of the neutron beam inside the sample is neglected. The kinematic theory is applicable to small samples of imperfect crystals or polycrystalline samples, where only a small fraction of neutrons are scattered. For larger crystals, the interference of the scattered neutron wave with the incident neutron wave must be considered [81]. For a large ideal crystal sample, the multiple scattering is simplified by the periodicity of the crystal; this topic has been treated in some fundamental publications (Darwin [82], Ewald [64] and Von Laue [65]) and these papers form the basis for the dynamic theory of diffraction. In the dynamic approach the interactions of the incident and diffracted waves are considered, such that the neutron waves propagate in the crystal as combinations of an incident and a diffracted wave. The propagation vectors and amplitudes are calculated as solutions of a stationary wave equation, meaning the incident and scattered neutrons are indistinguishable. The coherent, elastic scattered, wave function, includes all the possible multiple scattering effects, which are caused by the interaction of an incident neutron plane wave with the spherical waves scattered by all nuclei of the

crystal. There are two essentially different configurations for diffraction: Bragg setting, when the diffracted beam exit through the crystal surface exposed to the incident beam, or Laue setting, when the incident and diffracted beam exit through the same crystal surface. In the Bragg case, both incident and diffracted intensities are strongly extinguished under the crystal surface and their penetration depth is referred to as primary extinction length. In the Laue case, the neutron waves extend over the bulk of the crystal and the primary extinction length is determining the oscillating period of the coherent waves propagating through the crystal. Finally, the diffracted and transmitted intensities depend of the crystal thickness and the wave vector, resulting in a very fine oscillating angular pattern for a strictly monochromatic neutron beam. In both cases, the diffracted intensity is restricted to a narrow angular range around the Bragg condition, which corresponds to seconds of arc. In practice, there are very few perfect crystals (Si, Ge, etc.) which illustrate the dynamic diffraction theory. Any crystallographic defect will disturb the ideal coherent pattern and the influence of various structural distortions remains an active field of fundamental and applicative research. Single crystals used as samples in neutrons experiments are mostly mosaic crystals or imperfect crystals. An imperfect crystal is composed of mosaic blocks that are slightly misaligned. Each block slightly mis-oriented mutually is assumed to be a perfect crystal. Primary extinction may not occur in a mosaic crystal, if the mosaic block's thickness is less than the primary extinction length. In a thick crystal, the neutron or X-ray beam will progress through an ample number of similarly aligned mosaic blocks which cause the scattered waves in the crystal to be out of phase. The resulting destructive interference summation of the scattered neutron amplitudes is negligible, and thus the beam attenuation can be considered in kinematic approximation (secondary extinction).

The dynamic theory and Schrödinger equations are used to describe the scattering of neutrons by ideal crystals, while for mosaic crystals the scattering interaction is described by the transport equation. Here, a review of Sears [76] derivation of the

transport equation is shown and then applied to mosaic crystals. The transport equation yield the generalized Darwin equations which were derived by Darwin [82] [63] for X-ray diffraction. The generalized Darwin equations were later applied to a mosaic crystal planar slab by [83] for a single Bragg reflection, which resulted in a pair of coupled differential equations called the Ordinary Darwin equations. The transport equations which yields to Darwin's equation were shown to also be applicable to neutrons by Werner [81]. For planar crystals, the Ordinary Darwin coupled differential equation can be solved in one-beam or two-beam case to give the ratio of neutron current that is Bragg reflected or simply transmitted.

To derive the transport equations for neutrons, we consider neutrons illuminating a mosaic crystal of arbitrary size and shape. The average number of neutrons in a volume element $d\mathbf{r}$ with wave vector $d\mathbf{k}$ at time t and point \mathbf{r} is given by the probability density function $f(\mathbf{r}, \mathbf{k}, t)$. The quantity \mathbf{k} is related to the classic neutron velocity, \mathbf{v} , by the de Broglie relation $\hbar\mathbf{k} = m_n\mathbf{v}$ where m_n is the mass of the neutron.

For an ensemble of neutrons where the j^{th} neutron is at position \mathbf{r}_j and has wave number \mathbf{k}_j the probability density is written as the average of the ensemble

$$f(\mathbf{r}, \mathbf{k}, t) = \left\langle \sum_j \delta(\mathbf{r} - \mathbf{r}_j) \delta(\mathbf{k} - \mathbf{k}_j) \right\rangle. \quad (2.27)$$

The change of $f(\mathbf{r}, \mathbf{k}, t)$ with time using the chain rule yields the sum of the variations of \mathbf{r}_j and \mathbf{k}_j in time. The time variation of the probability density gives the transport equation:

$$\frac{\partial f(\mathbf{r}, \mathbf{k}, t)}{\partial t} = \left\langle \sum_j \left[\frac{\partial \mathbf{r}_j}{\partial t} \frac{\partial}{\partial \mathbf{r}_j} + \frac{\partial \mathbf{k}_j}{\partial t} \frac{\partial}{\partial \mathbf{k}_j} \right] \delta(\mathbf{r} - \mathbf{r}_j) \delta(\mathbf{k} - \mathbf{k}_j) \right\rangle. \quad (2.28)$$

The transport equation can be describe in two terms: the streaming effect

$$\left(\frac{\partial f(\mathbf{r}, \mathbf{k}, t)}{\partial t}\right)_s = \left\langle \sum_j \frac{\partial \mathbf{r}_j}{\partial t} \frac{\partial}{\partial \mathbf{r}_j} \delta(\mathbf{r} - \mathbf{r}_j) \delta(\mathbf{k} - \mathbf{k}_j) \right\rangle \quad (2.29)$$

and the collision effect

$$\left(\frac{\partial f(\mathbf{r}, \mathbf{k}, t)}{\partial t}\right)_c = \left\langle \sum_j \frac{\partial \mathbf{k}_j}{\partial t} \frac{\partial}{\partial \mathbf{k}_j} \delta(\mathbf{r} - \mathbf{r}_j) \delta(\mathbf{k} - \mathbf{k}_j) \right\rangle. \quad (2.30)$$

The stream effect in equation 2.29 can also be expressed in term of velocity

$$\left(\frac{\partial f(\mathbf{r}, \mathbf{k}, t)}{\partial t}\right)_s = \left\langle \sum_j (\mathbf{v}_j \cdot \nabla) \delta(\mathbf{r} - \mathbf{r}_j) \delta(\mathbf{k} - \mathbf{k}_j) \right\rangle \quad (2.31)$$

assuming only the strong nuclear force, \mathbf{F} , acting on the neutrons, the collision effect in equation 2.30 can be expressed as

$$\left(\frac{\partial f(\mathbf{r}, \mathbf{k}, t)}{\partial t}\right)_c = \left\langle \sum_j \frac{\mathbf{F}_j}{\hbar} \frac{\partial}{\partial \mathbf{k}_j} \delta(\mathbf{r} - \mathbf{r}_j) \delta(\mathbf{k} - \mathbf{k}_j) \right\rangle. \quad (2.32)$$

The collision term can further be expressed by scattering transition probabilities, but first let's denote the wave number for the incident wave outside of the mosaic crystal as \mathbf{k}_0 . Upon entering the mosaic crystal, the wave is scattered to wave vector \mathbf{k} . The scattered vector with number \mathbf{k} becomes the incident wave for another scatter process \mathbf{k}_0 which scatters to another wave vector \mathbf{k} . This process continues inside the mosaic crystal until the neutrons absorbed or exit the crystal. The transition probability per unit time for a neutron with wave number \mathbf{k} in the differential k-space volume $d\mathbf{k}_0$ to scatter to wave vector \mathbf{k}_0 is expressed as $p_s(\mathbf{k} \rightarrow \mathbf{k}_0)$, similarly the transition probability per unit time for a neutron with wave number \mathbf{k}_0 to scatter to wave vector \mathbf{k} is expressed as $p_s(\mathbf{k}_0 \rightarrow \mathbf{k})$, the probability for absorption per unit time is expressed

as $p_a(\mathbf{k})$. The collision term expressed in term of transition probabilities is

$$\left(\frac{\partial f(\mathbf{r}, \mathbf{k}, t)}{\partial t}\right)_c = \int \left[p_s(\mathbf{k} \rightarrow \mathbf{k}_0) f(\mathbf{r}, \mathbf{k}, t) - p_s(\mathbf{k}_0 \rightarrow \mathbf{k}) f(\mathbf{r}, \mathbf{k}_0, t) \right] d\mathbf{k}_0 - p_a(\mathbf{k}). \quad (2.33)$$

Substituting equation 2.31 and equation 2.33 into equation 2.28, and dividing both sides of the results by the velocity magnitude v , the neutron transport equation becomes

$$\left(\frac{1}{v} \frac{\partial}{\partial t} + \hat{\mathbf{v}} \cdot \nabla\right) f(\mathbf{r}, \mathbf{k}, t) = \int \left[p_s(\mathbf{k} \rightarrow \mathbf{k}_0) f(\mathbf{r}, \mathbf{k}, t) - p_s(\mathbf{k}_0 \rightarrow \mathbf{k}) f(\mathbf{r}, \mathbf{k}_0, t) \right] d\mathbf{k}_0 - p_a(\mathbf{k}). \quad (2.34)$$

Integrating equation 2.34 over \mathbf{k} yields the continuity equation

$$\frac{\partial n(\mathbf{r}, t)}{\partial t} + \nabla \cdot \mathbf{J}(\mathbf{r}, t) = s \quad (2.35)$$

where $n(\mathbf{r}, t)$ is the neutron number density,

$$n(\mathbf{r}, t) = \int f(\mathbf{r}, \mathbf{k}, t) d\mathbf{k} \quad (2.36)$$

$\mathbf{J}(\mathbf{r}, t)$ is the neutron current density,

$$\mathbf{J}(\mathbf{r}, t) = \int \mathbf{v} f(\mathbf{r}, \mathbf{k}, t) d\mathbf{k} \quad (2.37)$$

and s is the neutron sink density,

$$s(\mathbf{r}, t) = \int p_a(\mathbf{k}) f(\mathbf{r}, \mathbf{k}, t) d\mathbf{k}. \quad (2.38)$$

2.2.1 Scattering and Absorption Probabilities

It is possible to express the neutron transport equation in terms of macroscopic cross section per unit volume. The macroscopic cross section per unit volume $\Sigma_s(\mathbf{k}_0)$ is the integration of equation 2.2 over a solid angle, Ω , and energy, E_1 . $\Sigma_s(\mathbf{k}_0)$ is the scatter cross section σ divided by the sample's volume V , $\Sigma_s(\mathbf{k}_0)$ can also be describe as the ratio of the scatter probability per unit time $p_s(\mathbf{k}_0)$ for the incident neutron with wave vector \mathbf{k}_0 divided by v the neutron velocity.

$$\Sigma_s(\mathbf{k}_0) = \frac{p_s(\mathbf{k}_0)}{v} = \frac{\sigma}{V} = \frac{1}{V} \int dE_1 \int d\Omega \frac{d^2\sigma}{dE_1 d\Omega} \quad (2.39)$$

$p_s(\mathbf{k}_0)$ is the probability per unit time for scatter of a neutron with wave vector \mathbf{k}_0 and is obtained by the integration over \mathbf{k} of the neutron transition probability for scatter from incident wave vector \mathbf{k}_0 to scattered wave vector \mathbf{k} and is written as

$$p_s(\mathbf{k}_0) = \int d\mathbf{k} p_s(\mathbf{k}_0 \rightarrow \mathbf{k}). \quad (2.40)$$

Similarly the macroscopic absorption cross section per unit time $\Sigma_a(\mathbf{k}_0)$ is defined as the the ratio of the scatter probability per unit time $p_a(\mathbf{k}_0)$ for the incident neutron with wave vector \mathbf{k}_0 divided by v the neutron velocity.

$$\Sigma_a(\mathbf{k}_0) = \frac{p_a(\mathbf{k}_0)}{v} = \frac{\sigma_a}{V} = \frac{1}{V} \int dE_1 \int d\Omega \frac{d^2\sigma}{dE_1 d\Omega}. \quad (2.41)$$

The total neutron cross section per unit volume $\Sigma(\mathbf{k}_0)$, is the sum of equation 2.39 and equation 2.41 which is the summation of the scattering and absorption components and is written as

$$\Sigma(\mathbf{k}_0) = \Sigma_s(\mathbf{k}_0) + \Sigma_a(\mathbf{k}_0). \quad (2.42)$$

The cross section per unit volume has units of inverse length (i.e cm^{-1}) like the linear attenuation coefficient $\mu(\mathbf{k}_0)$ in material. For neutrons and x-rays, the linear absorption coefficient is the product of attenuation per unit cross section $\sigma(\mathbf{k}_0)$ and the atom number density ϱ , where attenuation coefficient per unit volume is Σ_a thus

$$\mu(\mathbf{k}_0) = \varrho\sigma_t(\mathbf{k}_0) = \varrho V\Sigma(\mathbf{k}_0). \quad (2.43)$$

$\mu(\mathbf{k}_0)$ depends solely on the material's cross section and atom number density, and it is independent of whether the material is in a liquid, solid, gas, crystalline or amorphous state.

The scatter cross section in a crystal is the summation of two components, the diffracted and the diffuse scatter. For example, if a mosaic crystal as N unit cells, $\Sigma_s(\mathbf{k}_0)$ is now the sum of N diffracted terms of the lattice vectors $\Sigma_{s,hkl}(\mathbf{k}_0)$, which is indexed by integer hkl , and the diffuse terms $\Sigma_{sd}(\mathbf{k}_0)$, where

$$\Sigma_s = \sum_{hkl=1}^N \Sigma_{s,hkl}(\mathbf{k}_0) + \Sigma_{sd}(\mathbf{k}_0). \quad (2.44)$$

The total cross section per unit volume in the mosaic crystal is

$$\Sigma = \sum_{hkl=1}^N \Sigma_{s,hkl}(\mathbf{k}_0) + \Sigma_{sd}(\mathbf{k}_0) + \Sigma_a(\mathbf{k}_0). \quad (2.45)$$

$\Sigma_{s,hkl}$ most important property is that it is nonzero only when the Bragg condition is met, that is only if \mathbf{k}_0 lies on or very near the Brillouin zone boundary which bisects the reciprocal lattice vector $\boldsymbol{\tau}_{hkl}$. Thus

$$\Sigma_{s,hkl}(\mathbf{k}_0) \neq 0 \rightarrow \mathbf{k}_0 \cdot \boldsymbol{\tau}_{hkl} = \frac{1}{2}\tau_{hkl}^2. \quad (2.46)$$

$$\Sigma_{s,hkl}(\mathbf{k}_0) = 0 \rightarrow \mathbf{k}_0 \cdot \boldsymbol{\tau}_{hkl} \neq \frac{1}{2}\tau_{hkl}^2. \quad (2.47)$$

The approximation of the probability density per unit time that an outgoing neutron with wave vector \mathbf{k} will be scattered into the incident wave vector \mathbf{k}_0 , $p_s(\mathbf{k} \rightarrow \mathbf{k}_0)$, can be summed in terms of the diffraction scatter components and the diffuse scatter components. The diffraction scatter term is the summation of the scatter cross section per unit volume, $\Sigma_{s,hkl}(\mathbf{k})$ for the outgoing neutrons and the wave vector \mathbf{k} over the τ_{hkl}^{th} reciprocal lattice vectors $\boldsymbol{\tau}_{hkl}$. The diffraction components for outgoing neutrons with wave vector \mathbf{k} , is added to the diffuse terms $p_{sd}(\mathbf{k} \rightarrow \mathbf{k}_0)$, where

$$\frac{1}{v}p_s(\mathbf{k} \rightarrow \mathbf{k}_0) \cong \sum_{hkl=1}^N \Sigma_{s,hkl}(\mathbf{k}_0)\delta(\mathbf{k} - \mathbf{k}_0 - \boldsymbol{\tau}_{hkl}) + \frac{1}{v}p_{sd}(\mathbf{k} \rightarrow \mathbf{k}_0). \quad (2.48)$$

Assuming the neutron velocity and its waves are identical in direction with a magnitude of unity, the neutron transport equation becomes.

$$\left(\frac{1}{v}\frac{\partial}{\partial t} + \hat{\mathbf{k}}_0 \cdot \nabla + \Sigma(\mathbf{k}_0)\right)f(\mathbf{r},\mathbf{k},t) = \int [p_s(\mathbf{k} \rightarrow \mathbf{k}_0)f(\mathbf{r},\mathbf{k},t)]d\mathbf{k} \quad (2.49)$$

In the case of steady state or time independence, the time derivative remove from the neutron transport equation and thus equation 2.49 is simplified to

$$\left(\hat{\mathbf{k}}_0 \cdot \nabla + \Sigma(\mathbf{k}_0)\right)f(\mathbf{r},\mathbf{k},t) = \int [p_s(\mathbf{k} \rightarrow \mathbf{k}_0)f(\mathbf{r},\mathbf{k},t)]d\mathbf{k} \quad (2.50)$$

substituting equation 2.45 and equation 2.49 into equation 2.50, the neutron transport equation is expressed in terms of macroscopic cross section

$$\begin{aligned}
& \left(\hat{\mathbf{k}}_0 \cdot \nabla + \sum_{hkl=1}^N \Sigma_{s,hkl}(\mathbf{k}_0) + \Sigma_{sd}(\mathbf{k}_0) + \Sigma_a(\mathbf{k}_0) \right) f(\mathbf{r}, \mathbf{k}, t) = \\
& \int \left[\sum_{hkl=1}^N \Sigma_{s,hkl}(\mathbf{k}_0) \delta(\mathbf{k} - \mathbf{k}_0 - \boldsymbol{\tau}_{hkl} + \frac{1}{v} p_{sd}(\mathbf{k} \rightarrow \mathbf{k}_0)) \right] d\mathbf{k}.
\end{aligned} \tag{2.51}$$

A zero value for the reciprocal lattice index hkl corresponds to the neutrons being Bragg reflected in the same direction as the incident beam therefore are transmitted, a nonzero value for the reciprocal lattice index hkl corresponds the neutrons which are Bragg reflected in a different direction than the incident beam.

2.2.2 Generalized Darwin Equation

Now consider a mosaic crystal with arbitrary shape and size submerge in a collimated mono-energetic beam of incident neutrons with wave vector \mathbf{k}_0 . To find a solution for the neutron transport equation at positions \mathbf{r} inside of the mosaic crystal for all wave vector \mathbf{k} , the trial solution $f(\mathbf{r}, \mathbf{k})$ is proposed

$$f(\mathbf{r}, \mathbf{k}) = \sum_{hkl} n_{hkl}(\mathbf{r}) \delta(\mathbf{k} - \mathbf{k}_{hkl}) + f_d(\mathbf{r}, \mathbf{k}). \tag{2.52}$$

For $hkl = 0$, the variable $n_o(\mathbf{r})$, is the neutron number in the transmitted beam with wave vector \mathbf{k}_0 , and for $hkl \neq 0$, $n_{hkl}(\mathbf{r})$ is the neutron number density in the beam that is Bragg reflected via the lattice vector $\boldsymbol{\tau}_{hkl}$ and have wave vector $\mathbf{k}_{hkl} = \mathbf{k}_0 - \boldsymbol{\tau}_{hkl}$. The phase-space distribution for the diffuse scattered neutrons is $f_d(\mathbf{r}, \mathbf{k})$. Inserting the trial solution $f(\mathbf{r}, \mathbf{k})$ of equation 2.52 into the neutron transport equation of equation

2.51 for the mosaic crystal, which then becomes

$$\begin{aligned}
& \sum_{hkl=1}^N \delta(\mathbf{k} - \mathbf{k}_{hkl}) \left\{ \left[\hat{\mathbf{k}}_{hkl} \cdot \nabla + \Sigma(\mathbf{k}_{hkl}) \right] n_{hkl}(\mathbf{r}) - \sum_{hkl' (=hkl)=1}^N \left[\Sigma_{hkl-hkl'}(\mathbf{k}_{hkl'}) \right] n_{hkl'}(\mathbf{r}) \right\} + \\
& \left(\hat{\mathbf{k}}_0 \cdot \nabla + \Sigma_{sd}(\mathbf{k}_0) + \Sigma_a(\mathbf{k}_0) \right) f_d(\mathbf{r}, \mathbf{k}_0) - \frac{1}{v} \sum_{hkl=1}^N p_{sd}(\mathbf{k}_{hkl} \rightarrow \mathbf{k}_0) n_{\tau}(\mathbf{r}) \\
& - \frac{1}{v} \int p_{sd}(\mathbf{k} \rightarrow \mathbf{k}_0) f_d(\mathbf{r}, \mathbf{k}) d\mathbf{k} + \sum_{hkl=1}^N \Sigma_{hkl}(\mathbf{k}_0) f_d(\mathbf{r}, \mathbf{k}_0) - \\
& \Sigma_{-hkl}(\mathbf{k}_0 - \boldsymbol{\tau}_{hkl}) f_d(\mathbf{r}, \mathbf{k}_0 - \boldsymbol{\tau}_{hkl}).
\end{aligned} \tag{2.53}$$

Here $\boldsymbol{\tau}_{hkl-hkl'} = \boldsymbol{\tau}_{hkl} - \boldsymbol{\tau}_{hkl'}$. The third term of equation 2.53 accounts for the neutrons that are Bragg reflected which have already been diffusely scattered and the term is non zero only if the incident wave vector \mathbf{k}_0 of the diffuse scattered neutrons met the Bragg condition found in equation 2.45. The probability for a diffusely scattered neutron with wave vector \mathbf{k}_0 to undergo a second scatter by diffraction to wave vector \mathbf{k} is low, hence one can assume a neutron which enters a mosaic crystal and diffusely scattered will scattered further inside the crystal only by diffuse scatter and not Bragg reflection, thus the third term of equation 2.52 is approximated to zero and can be omitted.

With the omission of the third term, the trial solution for the neutron transport must hold for an arbitrary value of \mathbf{k}_0 . Setting the first term to zero yields

$$\sum_{hkl=1}^N \delta(\mathbf{k} - \mathbf{k}_{hkl}) \left\{ \left[\hat{\mathbf{k}}_{hkl} \cdot \nabla + \Sigma(\mathbf{k}_{hkl}) \right] n_{hkl}(\mathbf{r}) = \sum_{hkl' (=hkl)=1}^N \left[\Sigma_{hkl-hkl'}(\mathbf{k}_{hkl'}) \right] n_{hkl'}(\mathbf{r}) \right\} \tag{2.54}$$

which is the generalized Darwin equation. They are a set of homogeneous equations, which can be solved with applied boundary conditions and yields solutions for the neutron number densities $n_{hkl}(\mathbf{r})$ in the transmitted and Bragg-reflected beams.

Setting the second term of equation 2.52 to zero yields the diffuse scatter equation

$$\begin{aligned} \left(\hat{\mathbf{k}}_0 \cdot \nabla + \Sigma_{sd}(\mathbf{k}_0) + \Sigma_a(\mathbf{k}_0) \right) f_d(\mathbf{r}, \mathbf{k}_0) &= \frac{1}{v} \sum_{hkl=1}^N p_{sd}(\mathbf{k}_{hkl} \rightarrow \mathbf{k}_0) n_{hkl}(\mathbf{r}) \\ &- \frac{1}{v} \int p_{sd}(\mathbf{k} \rightarrow \mathbf{k}_0) f_d(\mathbf{r}, \mathbf{k}) d\mathbf{k}. \end{aligned} \quad (2.55)$$

The diffuse scatter equation is an inhomogeneous linear equation for the phase space distribution of the diffusely scattered neutrons, and the inhomogeneous term accounts for the diffuse scatter in both the transmitted and Bragg-reflected beam.

2.2.3 Darwin Equation for a Mosaic Slab Crystal

For any incident wave vector \mathbf{k}_0 that satisfies the Bragg reflection condition for a particular lattice vector $\boldsymbol{\tau}$, that corresponds to a set of hkl reflection planes in a mosaic crystal, equation 2.54 becomes a pair of Darwin equations at $hkl = 0$ and $hkl \neq 0$

$$\begin{aligned} \left[\hat{\mathbf{k}}_o \cdot \nabla + \Sigma(\mathbf{k}_0) \right] n_o(\mathbf{r}) &= \left[\Sigma_{-hkl}(\mathbf{k}_{hkl}) \right] n_{hkl}(\mathbf{r}) & hkl = 0 \\ \left[\hat{\mathbf{k}}_{hkl} \cdot \nabla + \Sigma(\mathbf{k}_{hkl}) \right] n_{hkl}(\mathbf{r}) &= \left[\Sigma_o(\mathbf{k}_0) \right] n_o(\mathbf{r}) & hkl \neq 0. \end{aligned} \quad (2.56)$$

The macroscopic cross sections per unit volume $\Sigma(\mathbf{k}_o)$ and $\Sigma(\mathbf{k}_{hkl})$ for the incident wave vectors \mathbf{k}_0 and are given respectively

$$\Sigma(\mathbf{k}_0) = \Sigma_{hkl}(\mathbf{k}_0) + \Sigma_{sd}(\mathbf{k}_0) + \Sigma_a(\mathbf{k}_0) \quad (2.57)$$

$$\Sigma(\mathbf{k}_{hkl}) = \Sigma_{-hkl}(\mathbf{k}_{hkl}) + \Sigma_{sd}(\mathbf{k}_{hkl}) + \Sigma_a(\mathbf{k}_{hkl}) \quad (2.58)$$

where \mathbf{k}_{hkl} is the difference between \mathbf{k}_0 and $\boldsymbol{\tau}_{hkl}$. Now consider a mosaic crystal in the form of a slab which are separated by thickness D along the z direction and area S , the lateral dimension of the crystal is assume to be large enough so that edge effects can be neglected. The input mosaic crystal face is in the xy plane , with at $z = 0$ and output $z = D$. It follows that the transmitted neutron density $n_o(\mathbf{r})$ as a function of a vector \mathbf{r} can be replace by the dependence on axial dependence z , therefore is independent of x and y . the neutron densities can be expressed as $n_o(\mathbf{r}) = n_o(z)$ $n_{hkl}(\mathbf{r}) = n_{hkl}(z)$, the incident neutron beam velocity v_o is elastically scattered to the same velocity v_{hkl} .

The neutron beams enters the mosaic crystal slab at the face $z = 0$ with a surface angle ϕ_o which is measured respectively in the xy plane. The Bragg reflected beam angle occurs at angle ϕ relative to surface $z = 0$. The neutron current in the mosaic crystal for input and output surface area S are given

$$I_o(z) = n_o(z)v_o S \sin \phi_o \quad (2.59)$$

$$I_{hkl}(z) = n_{hkl}(z)v_{hkl} S \sin \phi. \quad (2.60)$$

At surface face $z = 0$, the incident neutron current is $I_o(\theta)$, at the transmitted surface $z = D$, the incident neutron current is $I_o(D)$. The neutron current for the Bragg reflected case at surface $z = 0$ is $I_{hkl}(\theta)$, and forward reflection the Laue case, the neutron current at output surface D is $I_{hkl}(D)$. As consequence of the conditions stated above and physical, the general Darwin equation reduces to those given in his

classic paper of 1922, where

$$\left[\frac{d}{dz} + \alpha_0 + \beta_0 \right] I_0(z) = 0 \quad (2.61)$$

and

$$\left[\pm \frac{d}{dz} + \alpha + \beta \right] I_0(z) = 0 \quad (2.62)$$

where the \pm in equation 2.62 refers to the Laue case and Bragg case respectively. The coefficients are given by

$$\begin{aligned} \alpha_o &= \mu \csc \phi_o, & \beta_o &= \Sigma_{hkl}(\mathbf{k}_0) \csc \phi_o \\ \alpha &= \mu \csc \phi, & \beta &= \Sigma_{-hkl}(\mathbf{k}_{hkl}) \csc \phi \end{aligned} \quad (2.63)$$

where μ is the absorption coefficient 2.43.

2.2.4 Solution of the Darwin Equations

First, the boundary conditions for the coupled Darwin equations are to be determined. In the Laue case or the Bragg forward reflection, the Darwin equation are solved for boundary conditions of zero diffracted neutron current at the surface $z = 0$, where

$$I_{hkl}(0) = 0 \quad \text{Laue case.} \quad (2.64)$$

The reflection ratio R and the transmission ration T occurs at index $hkl \neq 0$ and $hkl = 0$. The reflection R is the ratio of Bragg reflected forward neutron current $I_{hkl}(D)$ at $z = D$ divided by the incident neutron current $I_o(0)$, where

$$R = \frac{I_{hkl}(D)}{I_o(0)} \quad \text{Laue case.} \quad (2.65)$$

In the Bragg case of backward reflection, the Darwin equation are solved at zero neutron current $I_{hkl}(D)$ at the surface $z = D$, where

$$I_{hkl}(D) = 0 \quad \text{Bragg case.} \quad (2.66)$$

The reflection R is the ratio of Bragg back reflected neutron current $I_{hkl}(0)$ at $z = 0$ divided by the incident neutron current $I_o(0)$, where

$$R = \frac{I_{hkl}(0)}{I_o(0)} \quad \text{Bragg case.} \quad (2.67)$$

The transmission T is the ratio of the transmitted current $I_o(D)$ at $z = D$ divided by the incident neutron current $I_o(0)$, where

$$T = \frac{I_o(D)}{I_o(0)} \quad \text{Laue and Bragg case.} \quad (2.68)$$

One-Beam (OFF-Bragg)

Consider the one beam-case where the angle of the incident neutron beam at the surface of the mosaic slab, and the angle of the diffracted beam do not meet the Bragg condition so that $\beta = \beta' = 0$. In this case the Bragg reflected current is zero, so that $I_{hkl}(z) = 0$ which eliminates the second Darwin equation, we thus solve for the transmitted beam current $I_0(z)$ using equation 2.61,

$$\left[\frac{d}{dz} + \alpha_0 \right] I_0(z) = 0 \quad (2.69)$$

The solution for equation 2.69

$$I_0(z) = I_0(0) \exp [- \alpha_0 z]. \quad (2.70)$$

The reflection R is zero and the transmission T follows Lambert's law and is written as

$$T = \frac{I_D}{I_0} = \exp[-\alpha_0 D]. \quad (2.71)$$

Two-Beams (Bragg)

Next the two beam case is considered, in this case the incident neutron beam satisfies the Bragg condition, and produces a transmitted and one Bragg reflected beam. The linear attenuation coefficient of neutrons by material μ is usually small when compared to the attenuation of neutrons by secondary extinction. Therefore μ can be neglected and the parameters $\alpha_0 = \alpha = 0$.

The first Darwin equation is simplified to

$$\left[\frac{d}{dz} + \beta_0 \right] I_0(z) = \beta I_{hkl}(z). \quad (2.72)$$

Transposing [2.72](#) returns the first Darwin equation as

$$\frac{dI_0(z)}{dz} = \beta I_{hkl}(z) - \beta_0 I_0(z). \quad (2.73)$$

Repeating the same procedure for the second Darwin equations yields

$$\mp \frac{dI_{hkl}(z)}{dz} = \beta_0 I_0(z) - \beta I_{hkl}(z) \quad (2.74)$$

where the (-) indicates Bragg geometry and the (+) indicates Laue geometry. For the Laue geometry a combination of equation [2.72](#) and [2.74](#) yields

$$\frac{dI_0(z)}{dz} = -\frac{dI_{hkl}(z)}{dz} = \beta I_{hkl}(z) - \beta_0 I_0(z). \quad (2.75)$$

With Boundary conditions $I_{hkl}(0) = 0$ the solutions for equation 2.75 are

$$I_0(z) = I_0(0) \left[\frac{\beta_0 \exp [- (\beta_0 + \beta) z] + \beta}{\beta_0 + \beta} \right] \quad (2.76)$$

$$I_{hkl}(z) = I_0(0) \left[\frac{\beta_0 \left(1 - \exp [- (\beta_0 + \beta) z] \right)}{\beta_0 + \beta} \right]. \quad (2.77)$$

The reflection R in the Laue geometry is written as

$$R = \frac{I_{hkl}(D)}{I_0(0)} = \frac{\beta_0 \left(1 - \exp [- (\beta_0 + \beta) D] \right)}{\beta_0 + \beta} \quad (2.78)$$

as required for neutron conservation in the case of zero absorption $R + T = 1$. Thus the transmission in the Laue geometry is given as

$$T = \frac{\beta + \beta_0 \exp [- (\beta_0 + \beta) D]}{\beta_0 + \beta}. \quad (2.79)$$

For the Bragg geometry a combination of equation 2.72 and 2.74 yields

$$\frac{dI_0(z)}{dz} = \frac{dI_{hkl}(z)}{dz} = \beta I_{hkl}(z) - \beta_0 I_0(z). \quad (2.80)$$

With Boundary conditions $I_{hkl}(D) = 0$ the solutions for equation 2.80 are

$$I_0(z) = I_0(0) \left[\frac{\beta_0 \exp [- (\beta_0 - \beta)(D - z)] - \beta}{\beta_0 \exp [- (\beta_0 - \beta) D] - \beta} \right] \quad (2.81)$$

$$I_{hkl}(z) = I_0(0) \left[\frac{\beta_0 \exp [- (\beta_0 - \beta)(D - z)] - 1}{\beta_0 \exp [- (\beta_0 - \beta) D] - \beta} \right]. \quad (2.82)$$

The reflection R in the Bragg geometry is written as

$$R = \frac{I_{hkl}(0)}{I_0(0)} = \frac{\beta_0 \exp [- (\beta_0 - \beta) D] - 1}{\beta_0 \exp [- (\beta_0 - \beta) D] - \beta}. \quad (2.83)$$

similarly the transmission T is obtained via neutron conservation and is given as

$$T = 1 - \frac{I_{hkl}(0)}{I_0(0)} = \frac{1 - \beta}{\beta_0 \exp [- (\beta_0 - \beta)D] - \beta}. \quad (2.84)$$

The special case of symmetric reflection in which the incident angle and the scattered angle are equal is considered in Bacon and Lowder. In the symmetric Bragg geometry for infinite thickness, the transmission T is zero and the reflection R is one. In the symmetric Laue geometry the reflection R is

$$R = \frac{I_{hkl}(D)}{I_0(0)} = \frac{1 - \exp [2\beta_0 D]}{2}. \quad (2.85)$$

We proceed by detailing the treatment of the attenuation of neutrons by single crystals, the attenuation coefficient μ different from zero.

2.3 Attenuation of Neutrons by Crystals

The total cross-section determining the attenuations μ of neutron by matter is the sum of three parts.

$$\sigma_{total} = \sigma_{abs} + \sigma_{tds} + \sigma_{Bragg}. \quad (2.86)$$

2.3.1 Absorption Cross Section

The nuclear absorption cross-section σ_{abs} does not depend on the temperature and has a simple dependence on energy; except for some well known resonant cases the absorption cross section is given by

$$\sigma_{abs} = \frac{\sigma_o \sqrt{E_o}}{\sqrt{E}} \quad (2.87)$$

σ_o is the absorption cross section at thermal energies E_o , E_o is 0.0253 eV, and E is neutron energy. From this equation, the temperature independent absorption cross section is directly proportional to the neutron wavelength and for most materials follows the $\frac{1}{v}$ law.

2.3.2 Thermal Diffuse Scattering

Single Phonon Scattering Cross Section

The second contribution to σ_{total} is the thermal diffuse scattering cross section σ_{tds} . Following Freund [84] σ_{tds} can be calculated using the Debye model which permits the prediction of transmission properties of materials over a wide range of neutron energies absent of the details of the corresponding phonon spectra. σ_{tds} can be written in two terms, a single phonon scattering cross section σ_{sph} , and a multiple phonon scattering cross section σ_{mph} . The former is paramount in the domain of $E \ll k_B\Theta_D$ and is determined by the phonon annihilation processes which are described by the series

$$\sigma_{sph} = \left(\frac{\sigma_{bat}}{36A}\right)\left(\frac{\Theta_D}{E}\right)^{\frac{1}{2}} \begin{cases} R & x \leq 6 \\ 3.3x^{-7.2} & x > 6 \end{cases} \quad (2.88)$$

where σ_{bat} is the sum of the coherent and incoherent scattering cross section of the bound atom, A is the atomic mass number, Θ_D is the Debye temperature, $x = \Theta_D/T$ (T is the experimental temperature) and

$$R = \sum_{n=0}^{\infty} R_n \quad (2.89)$$

$$R_n = \frac{B_n x^{n-1}}{n!(n + \frac{5}{2})} \quad (2.90)$$

where B_n are the Bernoulli numbers.

Multiple Phonon Scattering Cross Section

The second term contributing to σ_{TDS} is dominant in the range $E \gg k_B\Theta_D$ where down-scattering and multiple phonon processes occur. The multiple phonon cross section σ_{mph} is deduced on first approximation dependent on the conservation of the number of incident and scattered neutrons, σ_{mph} is given by

$$\sigma_{mph} = \sigma_{free}\{1 - \exp[-(B_0 + B_T)C_2E]\} \quad (2.91)$$

where σ_{free} is the free atom cross section and is given by

$$\sigma_{free} = \sigma_{bat} \left[\frac{A}{(A+1)} \right]^2. \quad (2.92)$$

The term B_0 and B_T are given by

$$B_0 = \frac{3h^2}{(2k_B\Theta_D A)} \quad (2.93)$$

$$B_T = \frac{4B_0\varphi(x)}{x} \quad (2.94)$$

$$(2.95)$$

in which h is Planck's constant and

$$\varphi(x) = x^{-1} \int_0^x \frac{\xi}{e^{-\xi} - 1} d\xi. \quad (2.96)$$

C_2 is a constant which is dependent on the scattering material and given by equation $C_2 = 4.27 \exp(A/61)$ [84].

2.3.3 Bragg Scattering Cross Section

Bragg Scattering by Single Crystal

The diffraction profiles of mosaic crystals display peaks that are broader and lower in peak intensity when compared to the diffraction profile of perfect crystals. Zachariasen [85] and Bacon [86] have calculated the reflection powers for imperfect crystals. Both assumed a symmetrical approach where the incident and the diffracted beams make the same angle at the surface of the crystal slab, in which case the reflecting planes are either parallel or perpendicular to the surface of the crystal. In the case where the reflecting planes are neither parallel nor perpendicular to the surface, the reflection power has been calculated by Dietrich and Nielsen [18]. A more general solution of these equations has been formulated by Sears [19]. Sears equations for reflected R_{hkl} and transmitted T_{hkl} beam intensity in the Bragg geometry are given by

$$R_{hkl}(\lambda) = \frac{b}{\frac{(a+b)}{\Gamma} + A \coth(A)} \quad (2.97)$$

$$T_{hkl}(\lambda) = \frac{\sqrt{\frac{(a+b)^2}{\Gamma^2}} e^{-\left(\frac{a+b}{G}\right)}}{\frac{(a+b)}{\Gamma} \sinh(A) + \sqrt{\frac{(a+b)^2}{\Gamma^2} - \frac{b^2}{\gamma_o \gamma_H}} \cosh(A)} \quad (2.98)$$

and in the Laue case by

$$R_{hkl}(\lambda) = \frac{e^{-\left(\frac{a+b}{\Gamma}\right)} b \sinh(S)}{S} \quad (2.99)$$

$$T_{hkl}(\lambda) = e^{-\left(\frac{a+b}{\Gamma}\right)} \left[\cosh(S) - \frac{a+b}{G} \sinh(S) \right]. \quad (2.100)$$

The following auxiliary quantities are used in the Sears [19] solutions:

$$a = \frac{\mu\tau}{\gamma_o} \quad (2.101)$$

$$b = \frac{\sigma\tau}{\gamma_o} \quad (2.102)$$

$$\frac{1}{G} = \frac{1}{2} \left(\frac{1}{\gamma_o} - \frac{1}{\gamma_H} \right) \quad (2.103)$$

$$\frac{1}{\Gamma} = \frac{1}{2} \left(\frac{1}{\gamma_o} + \frac{1}{\gamma_H} \right) \quad (2.104)$$

$$A = \sqrt{\frac{(a+b)^2}{\Gamma^2} - \frac{b^2}{\gamma_o\gamma_H}} \quad (2.105)$$

$$S = \sqrt{\frac{(a+b)^2}{G^2} + \frac{b^2}{\gamma_o\gamma_H}} \quad (2.106)$$

where the crystal's thickness τ , the attenuation coefficient μ , and the Bragg reflection coefficient σ are the physical quantities that govern diffraction by mosaic crystals. $\sigma = QW[\theta - \theta_B]$ is the cross section per unit volume for Bragg reflection, where $Q = \lambda^3 F_{hkl}^2 N_c^2 / \sin 2\theta_B$, with λ the neutron wavelength, F_{hkl} the structure factor and N_c the number of unit cells per unit volume. $W[\theta - \theta_B]$ is the mosaic distribution usually assumed to be Gaussian, with θ being the angle formed by the incident beam and the Bragg planes and θ_B is the nominal Bragg angle. When there are no Bragg reflections present, R is zero in both Bragg and Laue geometry, and the transmission T is the recognizable Lambert law:

$$T_{hkl}(\lambda) = e^{-(\mu(\lambda)\tau)}. \quad (2.107)$$

Multiple Lattice Planes

For single crystals, Sears treated the case in which there is solely one reciprocal lattice plane on the Ewald sphere. As shown by Renniger [87] and Moon & Shull [88], there are instances in which the incident beam will interact with multiple lattice planes. Following Rossmanith's [89] approach to Renninger's [87] kinematic approximation

in the three-beam case, the total reflection can be approximated as

$$P^{\text{three-beam}}(\lambda) = P_o(k_{(hkl)} + k_{(hkl)'} - 2k_{(hkl)}k_{(hkl)'}) \quad (2.108)$$

where P_o is the power of the incident beam and $k_{(hkl)}, k_{(hkl)'}$ are partial reflectivities. In the case where absorption is not present, equation (2.108) can be written in terms of transmission as

$$T_i(\lambda) = T_{hkl}T_{hkl'} + (1 - T_{hkl})(1 - T_{hkl'}). \quad (2.109)$$

$T_{(hkl)}$ and $T_{(hkl)'}$ are the partial transmission coefficients calculated for the two-beam case. The approximation of equation 2.108 is valid only when $k_{(hkl)}$ and $k_{(hkl)'}$ are small, rendering equation 2.109 valid only when transmission values $T_{(hkl)}$ and $T_{(hkl)'}$ are large (0.5 or greater). In the region where the transmission values $T_{(hkl)}$ and $T_{(hkl)'}$ are small (less than 0.5), equation (2.109) gives an unphysical result, and a correction to the Renniger approximation has to be implemented as

$$P^{\text{three-Beam}}(\lambda) = P_o(k_{(hkl)} + k_{(hkl)'} - xk_{(hkl)}k_{(hkl)'}) \quad (2.110)$$

which modifies the transmission formula to

$$T_i(\lambda) = T_{(hkl)}T_{(hkl)'} + (x - 1)(1 - T_{(hkl)})(1 - T_{(hkl)'}) \quad (2.111)$$

The solution for the coefficient x must go to 1 for small transmission values, and at large transmission values x must approach the value of 2. We consider a simple solution for x and is given as

$$x = \frac{T_{(hkl)} + T_{(hkl)'}}{T_{(hkl)} + T_{(hkl)'} - T_{(hkl)}T_{(hkl)'}} \quad (2.112)$$

Substituting x into equation 2.111 and generalizing for the j^{th} lattice plane, which lies near the Ewald sphere, the transmission for a grain can be approximated using

$$T_i(\lambda) = \frac{1}{\sum_j (\frac{1}{T_j} - 1) + 1}. \quad (2.113)$$

Bragg Scattering by Polycrystal

A polycrystal solid is composed of many crystallites of varying size and orientations. The total transmission is a combination of the transmission from each grain. In this section, we demonstrate the approach to combine transmission for grains in a serial arrangement as well as for grains in a parallel arrangement within a voxel. In this work a polycrystal is defined by means of segmenting an infinite plate into columns consisting of N orientations with grain size defined as the ratio of number of orientation in a column to the thickness of the plate as illustrated in Figure 2.4. The transmission of each individual column with N orientations with the neutron beam is written as

$$T_c(\lambda) = \prod_{i=1}^N T_i(\lambda). \quad (2.114)$$

The transmission for a plate segmented into a number of columns A is written as the average over all the columns.

$$T_{total}(\lambda) = \frac{\sum_{j=1}^A \prod_{i=1}^N T_{i,j}(\lambda)}{A} \quad (2.115)$$

and the Bragg cross section σ_{Bragg}

$$\sigma_{Bragg} = \frac{V_o}{n} \ln \frac{1}{T_{total}(\lambda)}. \quad (2.116)$$

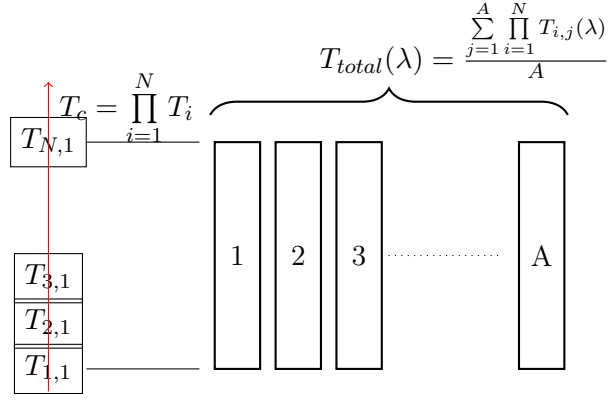


Figure 2.4: Segmented plate with A columns and with columns containing N distinct grain orientations. Each grain transmission is calculated, a distribution of grains is aggregated to form voxel transmission; with voxel transmission, a sample's transmission can be calculated.

By implementing equation 2.115, the simulator allows users to study partial volume effects.

Chapter 3

Implementation

In this chapter the implementation of the neutron transmission calculation as a computer program called *Sinpol* is described. Figure 3.1 shows a high level flow chart for the general approach to the simulation algorithm. The dashed line area in the flow chart contains the different input blocks that are required for the simulation of the neutron transmission spectra, the crystal and sample orientation block describes the necessary transformation to orient the crystal within the sample and the sample to the laboratory system, the single crystal neutron transmission calculation block contains the necessary physics calculations for the neutron transmission of a single grain, and finally the total transmission calculation block illustrates the manner in which the neutron transmission values for each grain in a population are combined to calculate the neutron transmission spectra through a voxel. The following subsections describe the component of the flow chart in Figure 3.1 followed by discussions of use for polycrystal and computing considerations.

3.1 Input Parameters

The content of the three input boxes necessary for neutron transmission spectra are discussed and some examples are shown. The Crystal Data input parameters that

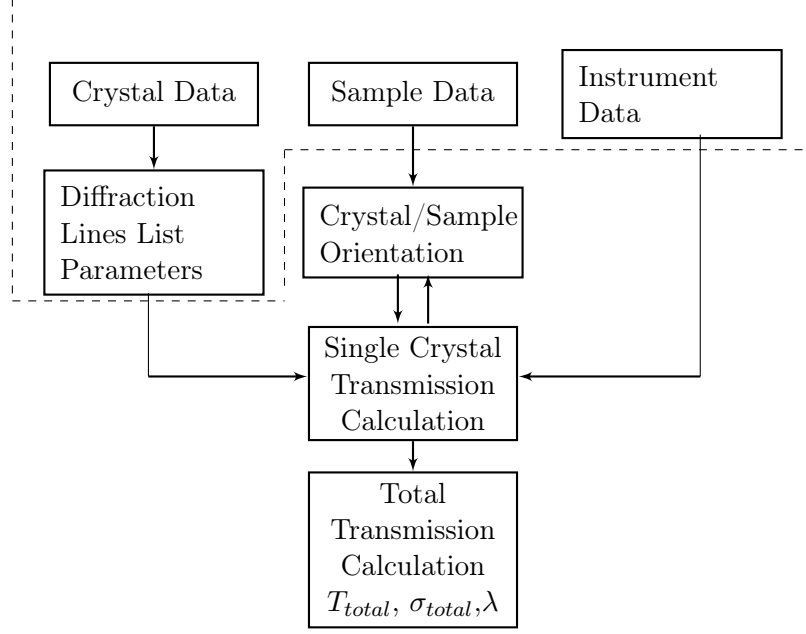


Figure 3.1: Schematic of *Sinpol* architectural organization.

contain structural, neutronic, mesoscale modelling and mosaic information are entered to calculate the diffraction lines list parameters that are essential for single crystal neutron transmission calculation are presented. Next the sample data parameters that contain the crystal orientation distribution within the sample, and the instrument data parameter that contains wavelength distributions and the relationship between the sample and laboratory system are presented.

3.1.1 Crystal Data

Prior to the neutron transmission calculation, the crystal data is defined and entered. First, the crystal unit cell as well as the lattice reflections are computed using the Computational Crystallography Toolbox [90](cctbx), a C++ programming language by Grosse-Kunstleve et al., 2002. The unit cell's crystal system is identified by one of three notations, space group number, Schönflies symbols, or Hermann-Mauguin symbols. Upon identifying the unit cell's crystal system, the hkl lattice reflection are initialized with the function *createHKL* and a list of crystal lattice reflections

up to a given maximum index number $hklmax$ is generated according to the defined space group. Crystal unit cell lattice parameters are read from a crystallographic information file (cif), or you can enter the lattice parameters with a .nxs file, which *Sinpol* uses. Lattice spacing values are calculated using the *dhklCalc* function, and unit cell volume is calculated using the function *volume*. The occupancy positions of the atoms inside the unit cell are entered in terms of *xyz*-coordinates and are obtained based on the space group using the Atomic Simulation Environment [91] package.

Once an element is chosen and a unit cell is generated, the following properties are assigned for calculation of the absorption cross section σ_{abs} , the scattering bound cross section σ_b , the coherent length b_{coh} , the atomic mass M , and the Debye temperature Θ_D . The cross section properties are read from the look up file *sinpol.dat* which was created by obtaining the cross section values from the NIST [77] website. Therefore it is necessary to update the *sinpol.dat* to ensure the most up to date values are used. The Debye temperature values can be read from several table found in literature. The mosaicity is implemented by calculating an angular spread in the current Bragg angle, θ , relative to the nominal Bragg angle, θ_B , using a normalized two-dimensional Gaussian function. In this thesis the width of the mosaic distribution, η , is quantified by its full width at half maximum (FWHM) value. The standard deviation(η) is entered in radians, Figure 3.2 show simulation results of a 1 cm thick copper plate with varying standard deviation. It demonstrates the influence of mosaic on the neutron transmission intensity, as the std. increases the neutron dips get wider and move away from the kinematical approximation.

3.1.2 Sample Data

The sample data parameters for the current simulation tool includes the crystal orientation distribution, the plate thickness, and grain size. The crystal orientation distribution defines whether a single crystal or a polycrystalline material is simulated.

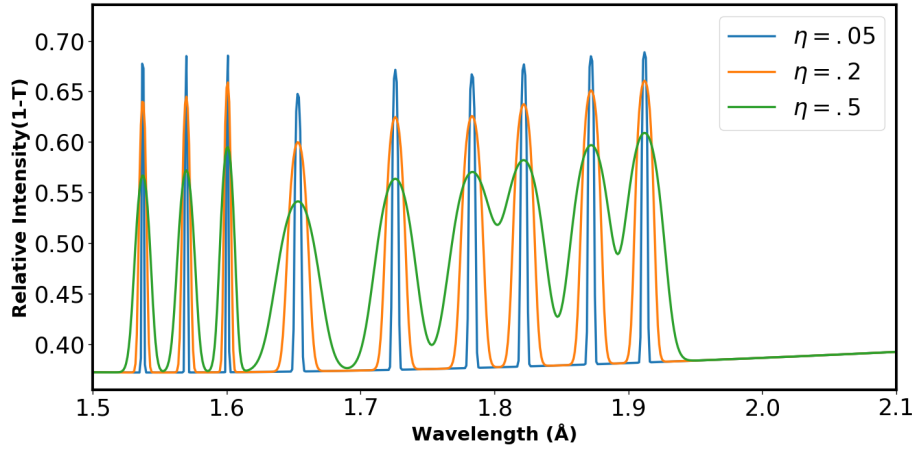


Figure 3.2: Neutron transmission simulation of a copper crystal for various mosaic spreads.

Each single crystal orientation is entered as three Euler angles defining the crystal orientation, \mathbf{g} , within the sample. The three Euler angles are the orientation of the crystal in relation to the neutron beam, therefore lattice planes of a crystal with different Euler angles will diffract at different wavelengths as illustrated by Figure 3.3. The plate thickness is the simulated path length of the sample in neutron beam. Figure 3.4 shows simulation results of five different plate thicknesses for a copper single crystal. This study was done to demonstrate the influence of plate thickness on neutron transmission intensity, in this work simulations assume a 1 cm plate thickness. For polycrystalline samples the grain size is defined as the ratio of the plate thickness to the number of grain orientations for a uniform grain distribution (see Figure 4.3), for varying grains in a distribution a log-normal distribution to generate thicknesses is implemented (see Figure 4.6).

The *Sinpol* software provides two possibilities to input a phase description: Its own .nxs format and the well-established CIF (Crystallographic Information File) format. Example of the nxs input file is shown in appendix, similarly the cif file is shown in appendix.

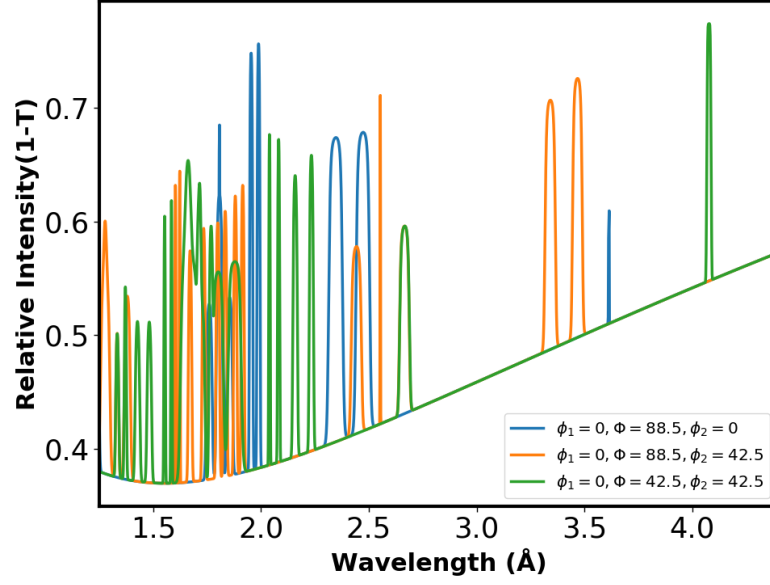


Figure 3.3: Neutron transmission simulation of a copper single crystal for various orientations.

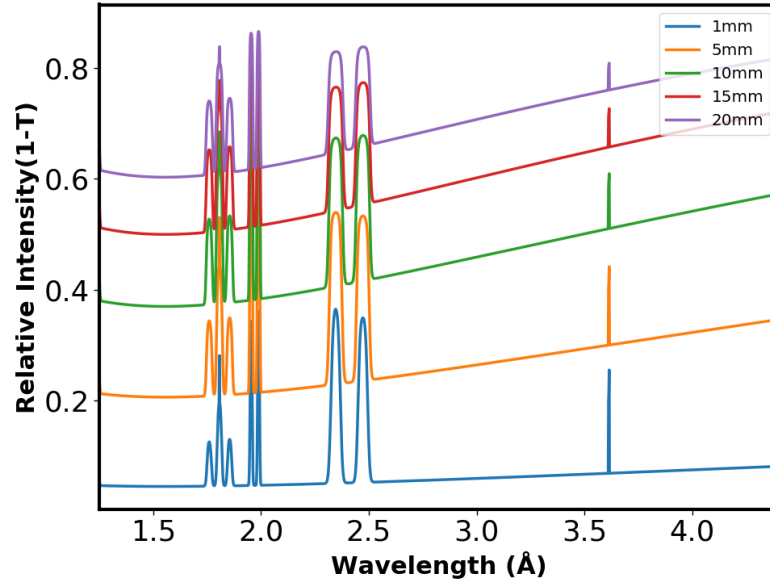


Figure 3.4: Neutron transmission simulation through different thickness of single crystal copper.

3.1.3 Instrumentation Data

The instrument data input includes a wavelength distribution defining the neutron source (the incident neutron wavelength and the incremental wavelength steps necessary for the neutron transmission calculation), the wavelength resolution of the instrument, and an angle ρ that defines the sample orientation within the instrument coordinate system.

3.2 Crystal/Sample Orientation

In order to simulate neutron transmission spectra, it is necessary to define the orientation of the crystals within the voxel and the orientation of the voxel in the neutron beam. These three dimensional rotations are performed in the crystal/sample orientation block of the flow chart. Two rotations are necessary to calculate the direction cosine of the incident beam γ_o and the diffracted beam γ_H , which are essential for transmission calculations. The next subsections describe the rotation of grains in a sample, rotation of the sample in the instrument, and calculations of the angular directions for each lattice plane in a grain.

3.2.1 Crystals in Sample's Coordinate System

The Euler angles refer to three rotations which, when performed in the correct order, transform the sample coordinate system into the crystal coordinate system. There are several convention in which to express the Euler angles. Here in this thesis, the sample geometry is described by three mutually perpendicular directions, normal direction (ND), transverse direction (TD), and rolling direction (RD). Furthermore, a grain in a cubic material is defined by three mutually perpendicular axes [001], [010] and [100]. The orientation of the crystal in the neutron beam is determined by three rotations that transform the sample's coordinate system into the crystal's coordinate system. I use the series of three rotations, suggested by Bunge [92], which are as follows (see

Figure 3.5).

1. A first rotation by an angle φ_1 is to be given around ND, which will take RD to the position RD' and TD to TD'. The amount of the angle φ_1 should be such that RD' will be perpendicular to the plane formed by ND and [001].
2. A second rotation by an angle Φ is to be given around RD'; the amount of Φ should be such that ND becomes coincident with [001]. By this process, TD' will assume the position TD''.
3. A third rotation by an angle φ_2 is to be given around (ND = [001]), the amount of φ_2 being such that by this rotation RD' goes to [100] and TD'' into [010].

According to the scheme proposed by Bunge, a set of $(\varphi_1, \Phi, \varphi_2)$ values signifies the orientation of a crystal. the three rotations are expressed analytically as

$$\mathbf{g}_{\varphi_1} = \begin{pmatrix} \cos \varphi_1 & \sin \varphi_1 & 0 \\ -\sin \varphi_1 & \cos \varphi_1 & 0 \\ 0 & 0 & 1 \end{pmatrix} \quad (3.1)$$

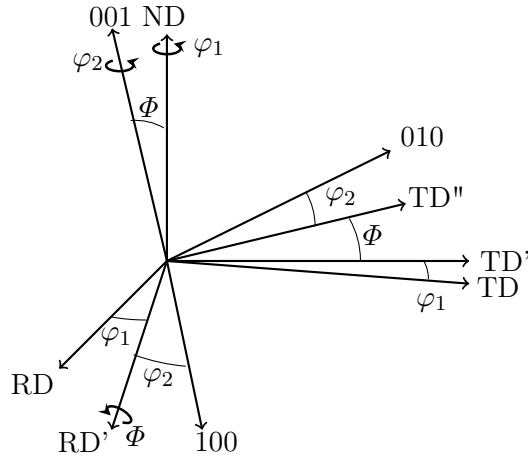


Figure 3.5: Schematic representation of Euler angles, as defined by Bunge[92].

$$\mathbf{g}_\Phi = \begin{pmatrix} 1 & 0 & 0 \\ 0 & \cos \Phi & \sin \Phi \\ 0 & -\sin \Phi & \cos \Phi \end{pmatrix} \quad (3.2)$$

$$\mathbf{g}_{\varphi_2} = \begin{pmatrix} \cos \varphi_2 & \sin \varphi_2 & 0 \\ -\sin \varphi_2 & \cos \varphi_2 & 0 \\ 0 & 0 & 1 \end{pmatrix}. \quad (3.3)$$

The multiplication of these matrices in order results in an expression which links the rotation matrix to the Euler angles. The product matrix multiplication is expressed in notation described by Popa [93]

$$\mathbf{a} = \mathbf{g}_{\varphi_1} \cdot \mathbf{g}_\Phi \cdot \mathbf{g}_{\varphi_2} \quad (3.4)$$

where the elements of the rotation matrix are given in terms of the Euler angles

$$\begin{aligned} a_{11} &= \cos \varphi_1 \cos \varphi_2 - \sin \varphi_1 \sin \varphi_2 \cos \Phi \\ a_{12} &= \sin \varphi_1 \cos \varphi_2 + \cos \varphi_1 \sin \varphi_2 \cos \Phi \\ a_{13} &= \sin \varphi_2 \sin \Phi \\ a_{21} &= -\cos \varphi_1 \sin \varphi_2 - \sin \varphi_1 \cos \varphi_2 \cos \Phi \\ a_{22} &= -\sin \varphi_1 \sin \varphi_2 - \cos \varphi_1 \cos \varphi_2 \cos \Phi \\ a_{23} &= \cos \varphi_2 \sin \Phi \\ a_{31} &= \sin \varphi_1 \sin \Phi \\ a_{32} &= -\cos \varphi_1 \sin \Phi \\ a_{33} &= \cos \Phi. \end{aligned} \quad (3.5)$$

Equation 3.4 is the orientation matrix that links the crystal reference vector basis to the sample vector basis as shown by Bunge [92]. Thus the rotation of a lattice vector

with reciprocal lattice coordinates h, k, l into the sample frame of reference Y_j^S can be performed and the lattice vector \vec{h} can be written as

$$\vec{h} = \sum_j \tilde{h}_j^S Y_j^S; \quad \tilde{h}_j^S = \sum_i \tilde{h}_i a_{ij} \quad (3.6)$$

where \tilde{h}_i is the normalized direction cosines corresponding to the hkl Miller indices. For crystals with cubic symmetry, the components of the reciprocal space vector \vec{h} in the sample coordinate system, h_j^S , are given as

$$h_1^S = \frac{ha_{11} + ka_{21} + la_{31}}{\sqrt{h^2 + k^2 + l^2}} \quad (3.7)$$

$$h_2^S = \frac{ha_{12} + ka_{22} + la_{32}}{\sqrt{h^2 + k^2 + l^2}} \quad (3.8)$$

$$h_3^S = \frac{ha_{13} + ka_{23} + la_{33}}{\sqrt{h^2 + k^2 + l^2}} \quad (3.9)$$

3.2.2 Sample in Laboratory' Coordinate System

While a sample can be positioned in any orientation within the instrument frame, the initial code assumes the simplest case of a rotation about the vertical axis, which mimics the common practice of rotation around a single axis for CT scanning. Thus the reciprocal lattice vector \vec{h} in the laboratory frame is written as

$$\vec{h} = \sum_j \tilde{h}_j^L Y_j^L \quad (3.10)$$

where

$$\tilde{\mathbf{h}}^L = \{\tilde{h}_1^S, \tilde{h}_2^S, \tilde{h}_3^S\} \begin{pmatrix} \cos \rho & 0 & -\sin \rho \\ 0 & 1 & 0 \\ \sin \rho & 0 & \cos \rho \end{pmatrix} \quad (3.11)$$

and ρ is the rotation angle. The reference orientation of the sample in the laboratory (instrument) frame considers the z axis of the sample along the neutron beam and the y axis perpendicular to the horizontal plane.

3.2.3 Calculation of Direction Cosines

The angle between the normal to the crystallographic surface and the neutron beam is the diffraction angle θ_B ; therefore the sine of θ_B is given as

$$\sin \theta_B = -\tilde{h}_1^S \sin \rho + \tilde{h}_3^S \cos \rho. \quad (3.12)$$

Using equation (3.12) Bragg's law can be written as

$$\lambda_B = 2d_{hkl} \sin \theta_B \quad (3.13)$$

where d_{hkl} is the spacing between hkl planes.

The diffraction intensity has dependency on the direction cosines of the incident beam to the crystallographic surface γ_0 , and the direction cosines of the diffracted beam to the crystallographic surface γ_H . Figure 3.6 illustrates the geometry of the incident beam impinging on a crystal hkl plane; \bar{S}_o and \bar{S}_H are respectively the incident beam and diffracted beam. Here the direction cosine of the incident beam is the dot product of the sample's normal vector $\vec{\mathbf{n}}_s$ and the incident neutron beam \vec{S}_o ;

simply put γ_o is written as

$$\gamma_0 = \vec{n}_s \cdot \vec{S}_o = Y_3^S \cdot Y_3^L = \cos \rho. \quad (3.14)$$

The direction cosine of the diffracted beam is the dot product between the sample's normal \vec{n}_s and \vec{S}_H the diffracted beam as

$$\gamma_H = \vec{n}_s \cdot \vec{S}_H = Y_3^S \cdot \vec{S}_H = \cos \rho - 2 \sin \theta_B \tilde{h}_3^S \quad (3.15)$$

γ_H determines the choice between Bragg geometry and Laue geometry, a value greater than zero indicates Laue geometry. In the reference orientation of the sample, Y_3^S is parallel to \vec{S}_o , γ_0 is equal to 1, and γ_H is $\cos 2\theta_B$.

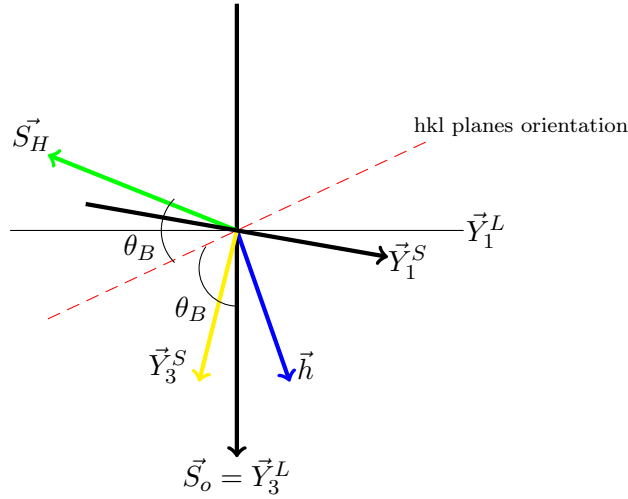


Figure 3.6: Scattering path in a plane-slab crystal, showing the relationship between the diffraction beam \vec{S}_H and the incident beam \vec{S}_o , and the relationship between the incident beam \vec{S}_o and the sample's normal \vec{Y}_3^S .

3.3 Single Crystal Transmission

The theory for calculating the neutron transmission for a single crystal has been presented in chapter 2 section 2, moreover the calculation of the neutron transmission for each lattice in a grain using the Sears formulas has presented in section 2.3.3. In the code, once grains have been oriented with the neutron beam, calculation of cross section for each grain is performed by first calculating the transmission for each reciprocal lattice point near the Ewald sphere, this calculation is dependent on diffraction geometry as outlined by the conditions of γ_H in the previous section. For grains in Laue geometry, transmissions and reflections are calculated using equations 2.99 and 2.100. For grains in Bragg geometry, transmissions and reflections are calculated using equations 2.97 and 2.98.

3.4 Total Transmission

Once transmissions for each lattice plane is calculated we then use equation 2.113 to combine the lattice transmissions to get a total transmission grain. When multiple reciprocal lattices are lying near the Ewald sphere, equation 2.113 can also be used to approximate a value for the total transmission. When a distributions of grains is considered the total transmission for a serial as well as parallel arrangement in voxels is described in section 2.3.3.

3.5 Polycrystal Transmission

A polycrystal solid is made up of many crystallites of varying sizes and orientations. The transmission curves for polycrystal solids are calculated based on the single transmission calculation. The code provides two manners to generated a random distribution of grains orientation. First, an orientation distribution function(ODF) is provided and defined in Chapter 5, second a random distribution of orientations is

generated by means of the low-discrepancy multi-dimensional Halton [94] sequence. The sequence is deterministic yet appears to be random for many purposes. In our case, a three dimensional sequence is used to generate a three dimensional array representing the orientation distribution. The distribution contains the three parameters of rotation as coordinates in Euler space. The Euler space is a three dimensional periodic lattice with unit cell $2\pi, 2\pi, 2\pi$; however, the region is restricted by a glide plane and becomes asymmetric with unit cell $\{2\pi, \pi, 2\pi\}$. Thus, the array elements representing φ_1 and φ_2 are multiplied by 2π , while Φ is generated by taking the inverse cosine of twice the array element minus one. Figure 3.7 presents a polycrystal powder neutron transmission simulation for various mosaic spread. Simulations were performed show the effect of mosaic on neutron transmission simulations.

3.6 Computing Considerations

Sinpol is written in Python programming language and has been packaged into a new flexible neutron transmission library. The python package allows for easy installation and use on multiple platforms (e.g. Linux, MacOSX, Windows), which

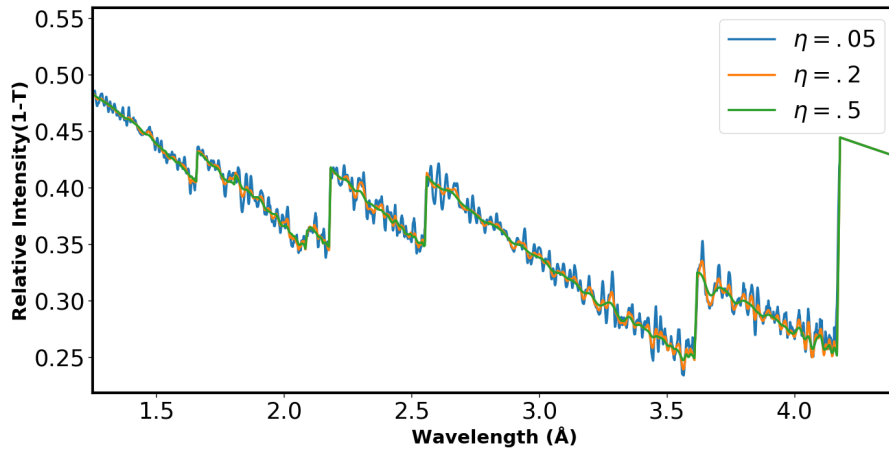


Figure 3.7: Neutron Transmission of a copper powder for various mosaic spreads.

in turn extends the availability of the library. For this thesis, neutron transmission calculations were performed on a 2.50 GHz intel core i5 processor personal laptop. The calculation varies with the number of grains and discretization of wavelengths bin. The calculation time for 10 distinct orientations discretized at one hundredth angstrom is less than a second, similarly the calculation time for 10,000 distinct orientations is 400 seconds. The time scales linearly with the number of distinct orientations used for the transmission calculation. The simulations for 10-million orientations were calculated with a cluster; the code was easily parallelized by sending 10,000 orientations to each node. On personal computers, the code can be parallelized via multiprocessing processes. Parallelization for using GPUs via pyCuda is another possible solution for higher speeds. Currently *Sinpol* calculates one neutron transmission spectrum for a voxel. To simulate an image of multiple voxels, it is necessary to calculate each voxel separately, and a parallel ray tracer can then be used to simulate the final image. Furthermore for computed tomography, the sample can be rotated by the angle ρ to obtain the neutron transmission spectrum for a voxel rotated the angle ρ ; similarly a parallel ray tracer can be used to simulate a final image.

Chapter 4

Sinpol: Testing and Verification

This chapter contains results published in Dessieux et al [95]. The single crystal simulations are bench marked with data found in literature. The polycrystal simulations are bench marked with data found in literature and compared with measurement taken at the Spallation Neutron source (SNS) in Oak Ridge, TN. Studies of the effect of grain size and studies of grain distribution are also presented.

4.1 Single Crystal

The neutron transmission spectra for a large imperfect single crystal of copper plate that is 10 mm thick and has mosaic spread of 0.2 degrees has been simulated. The main physical parameters required in the calculation are crystal lattice parameters, the Debye temperature Θ_D , the neutron coherent scattering length b , the neutron absorption cross section σ_{abs} , and the total bound scattering cross section σ_b . The values for the required physical parameters are shown in Table 4.1. Similar to the measurements presented by Santisteban [7], the simulated crystal is cut along the (110) plane and positioned such that the cosine of the (hkl) normal to the beam direction is given as

Table 4.1: Physical parameters for simulations of Cu, Fe, and Ni samples.

Element	Cu	Fe	Ni
Crystal Structure	fcc	bcc	fcc
Atomic Mass	63.55	55.45	58.69
Lattice Constant(Å)	3.61496	2.8665	3.52
$\Theta_D(\text{k})$	344	477	345
b(fm)	7.718	9.45	10.3
$\sigma_{abs}(\text{barns})$	3.78	2.56	4.49
$\sigma_b(\text{barns})$	8.035	11.62	18.5

$$\sin \theta_B = \frac{\tilde{h} + \tilde{k}}{\sqrt{2}} \quad (4.1)$$

where \tilde{h} and \tilde{k} are the normalized h, k values given below for the cubic crystal structure of copper

$$\tilde{h} = \frac{h}{\sqrt{h^2 + k^2 + l^2}}; \tilde{k} = \frac{k}{\sqrt{h^2 + k^2 + l^2}}. \quad (4.2)$$

Figure 4.1 presents wavelength-dependent transmission simulation results depicting the movement of peak locations and intensity as a function of crystal rotation. The crystal is rotated 180 degrees around the transverse (vertical) direction. These simulation results show the behavior of diffraction hkl peaks during rotation. When hkl peaks are closest to the Bragg-edge condition, they show the highest intensity, and the broadening induced by mosaic is less pronounced. When hkl peaks rotate away from the Bragg-edge condition ($\sin \theta_B = 1$), lower peak intensity and peak broadening due to mosaic are observed. At the Bragg-edge location, the diffraction peak is sharp and can be resolved only by considering the resolution of the instrument. The *Sinpol* simulation uses a Gaussian for the instrument function which is convolved with the simulated intensity. The gray-shaded area in Figure 4.1 corresponds to the range of rotation angles presented by Santisteban [7]. Here the rotation ranges from

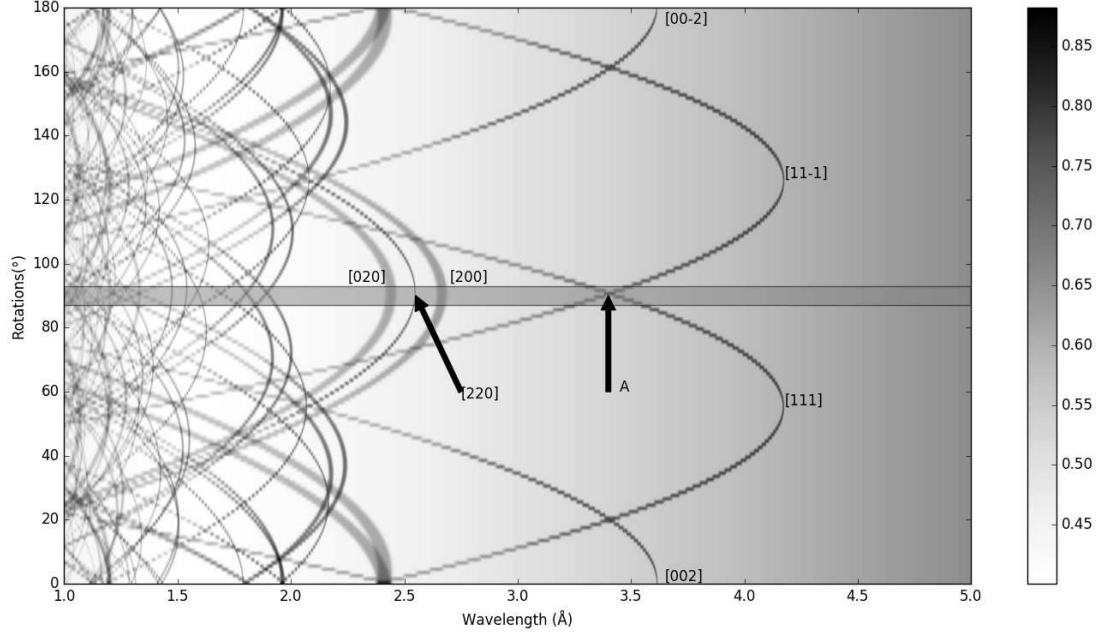


Figure 4.1: Movement of peak locations and intensity as a function of crystal rotation for a single crystal.

88 to 91 degrees. The simulation corresponds well with the initial measurement by Santisteban [7], and the simulated angles of interest are displayed in Figure 4.2. As outlined in Santisteban [7], the reduction of the incident beam intensity is governed by nuclear absorption and thermal diffuse scattering. The temperature-dependent thermal-diffuse scattering dominates at the shorter wavelength, while the temperature independent neutron absorption is linear and dominates at longer wavelengths. The Bragg reflections are seen as sharp peaks at precise wavelengths that can be calculated by using the alternative Bragg equation

$$\lambda_{hkl} = 2d_{hkl} \frac{\tilde{h} + \tilde{k}}{\sqrt{2}}. \quad (4.3)$$

The bottom of Figure 4.2 shows three discrete simulated rotations matching Santisteban's measurements. As the crystal is rotated by one-degree increments, the [200], [220] and [020] peaks remain stationary, as they are at an orientation where

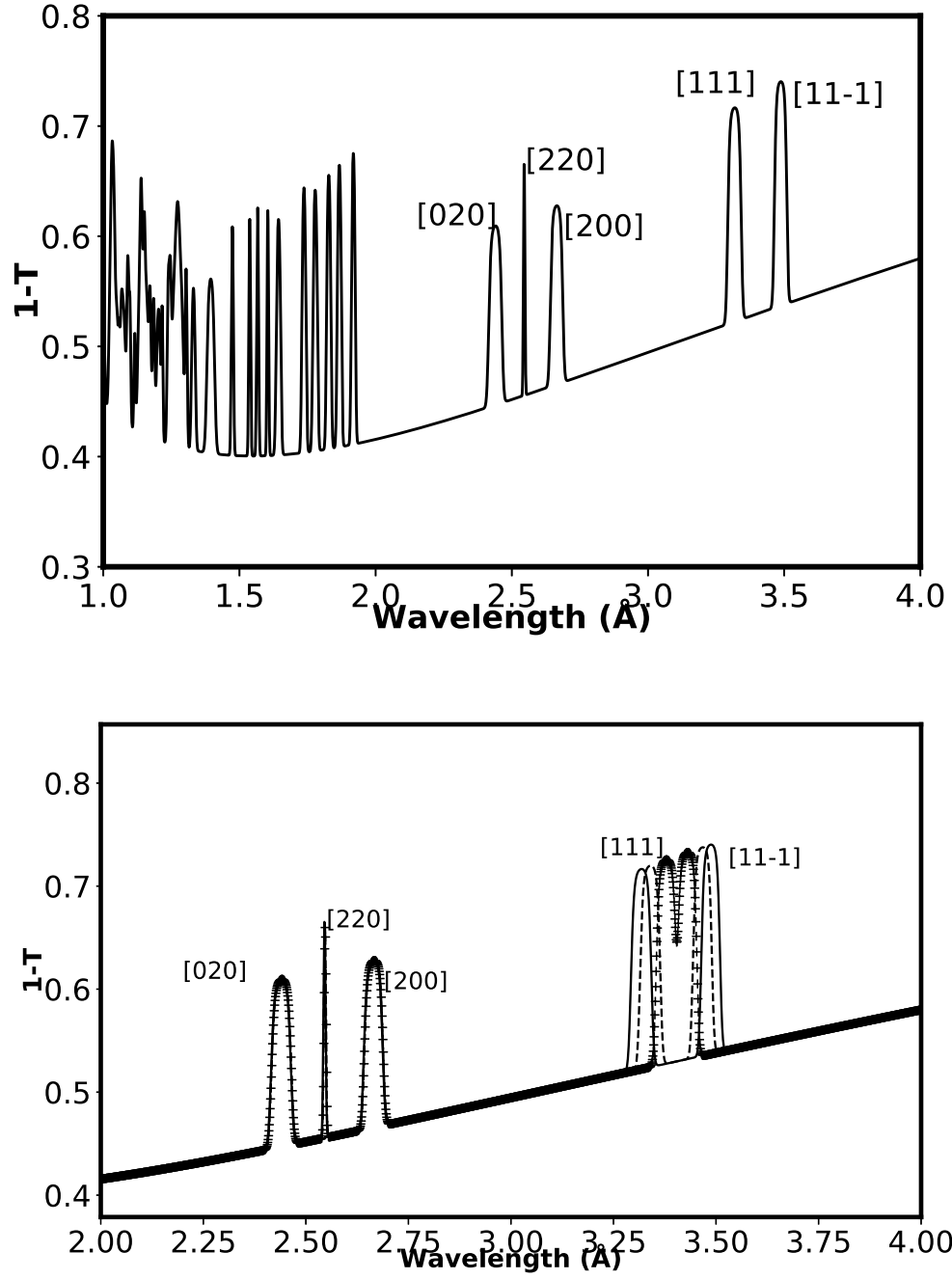


Figure 4.2: (top) Neutron transmission spectra of single copper crystal. (bottom) Shifts in peak position as a result of rotation of sample, solid line the incident beam is aligned with [110] direction, dashed line sample is rotated by 1 and 2 degrees in the transverse direction.

the angle between the reciprocal lattice vector and the neutron beam direction varies slowly with the sample's rotation. Further examination of Figure 4.1 shows that as the crystal is rotated, eventually the [200], [220], and [020] peaks will move toward shorter wavelengths, as the crystal's ND alignment with the beam is not perfect. [111] and [11-1] peaks show a noticeable movement in wavelengths moving toward shorter wavelengths and larger wavelengths respectively. The area labeled A in Figure 4.1 indicates a multi-beam scenario in which multiple Bragg reflections occur at the same wavelength. The transmission intensity is calculated to include contributions from multiple planes, using equation 2.113.

Table 4.2 shows the comparison of the peak locations in wavelengths measured from Santisteban [7] and the peak location from the *Sinpol* simulation. The difference between the *Sinpol*-simulated positions and the experimental positions varies from

Table 4.2: Typical parameters of the peaks observed in (1-T), simulated along the [110] direction of the reference copper sample and compared to measurement by Santisteban [7].

hkl	$\lambda_{hkl}(\text{\AA})$ [7]	$\lambda_{hkl}^{sp}(\text{\AA})$	Θ_B° [7]	Θ_B^{osp}
[111]	3.4366	3.4462	34.456	34.350
[11 $\bar{1}$]	3.3676	3.3621	36.184	36.345
[020]	2.6760	2.6691	42.219	42.409
[220]	2.5521	2.5531	2.74	2.786
[200]	2.4268	2.4372	47.807	47.608
[131]	1.9101	1.9105	28.76	28.789
[13 $\bar{1}$]	1.8917	1.8875	29.752	30.017
[311]	1.8197	1.8261	33.371	33.100
[31 $\bar{1}$]	1.8013	1.8032	34.241	34.189
[222]	1.7179	1.7231	34.567	34.350
[22 $\bar{2}$]	1.6840	1.6811	36.173	36.345
[331]	1.6170	1.6191	12.757	12.530
[33 $\bar{1}$]	1.6062	1.6059	14.347	14.494
[240]	1.5558	1.5551	15.679	15.865
[420]	1.5063	1.5086	21.232	21.058

a maximum of 0.43 percent difference at peak [200] to a minimum difference of 0.01 percent at peak [131], with an average peak difference of 0.062 percent over all peaks. The precision for the simulated peak positions can potentially be improved by adjusting the three Bunge angles to more precisely match the crystal orientation in the measurement.

4.1.1 Extinction

In a later paper, Malamud and Santisteban [96] introduced an extinction factor, which is dependent on the experimental geometry, the divergence of the beam, as well as the mosaicity of the sample. The extinction factor, y_{hkl} , is the ratio of the measured intensity to the predicted kinematical intensity, therefore it represents the reduction in measured intensity due to the effect of extinction. Table 4.3 shows the comparison of the peak locations in wavelengths measured from Malamud [96] and the peak location from the *Sinpol* simulation. The difference between the *Sinpol* simulated positions and the experimental positions varies from a maximum of 2.5 percent difference at peak [204] to a minimum difference of 0.1 percent at peak [111], with an average peak difference of 0.9 percent over all peaks. Column four is the reproduction of the extinction factor y_{hkl} , determined experimentally by Malamud [96]. The extinction factors calculated by *Sinpol* differ slightly from the experimental values reported in Table 4.3 in reference [96]; *Sinpol* uses a gaussian instrumental function to convolve the simulated intensity while Malamud and Santisteban [96] used a truncated exponential convoluted to a gaussian to measure intensity. The difference in the two fit functions may lead to intensity of simulated peaks in *Sinpol* being larger and affecting the extinction ratio. The last two columns present the measured and simulated peak fwhm ω , which are in a good agreement.

Table 4.3: Refined and derived peak parameters for the copper sample and compared to measurement by Malamud [96].

hkl	$\lambda_{hkl}[96](\text{\AA})$	$\lambda_{hkl}^{sinpol}(\text{\AA})$	$y_{hkl}[96]$	y_{hkl}^{sinpol}	$\omega[96]$	ω^{sinpol}
[111]	3.442	3.4439	0.004	0.0033	0.02	0.018
[1-11]	3.358	3.3549	0.004	0.0033	0.021	0.018
[200]	2.72	2.7103	0.007	0.0056	0.019	0.019
[202]	2.55	2.5402	0.006	0.0045	0.008	0.008
[002]	2.38	2.3868	0.010	0.0074	0.021	0.022
[311]	1.928	1.9178	0.020	0.0235	0.01	0.01
[3-11]	1.905	1.8902	0.020	0.0242	0.01	0.012
[113]	1.804	1.7917	0.024	0.0257	0.011	0.011
[1-13]	1.781	1.7707	0.024	0.0306	0.011	0.011
[222]	1.721	1.7107	0.028	0.0326	0.011	0.012
[2-22]	1.679	1.6663	0.025	0.0354	0.011	0.011
[313]	1.617	1.5821	0.023	0.0356	0.006	0.0066
[3-13]	1.604	1.5682	0.023	0.0382	0.006	0.0066
[402]	1.564	1.5315	0.022	0.0425	0.006	0.0066
[204]	1.496	1.4542	0.031	0.0526	0.007	0.007
[220]	1.391	1.3888	0.039	0.0356	0.016	0.015
[400]	1.36	1.3445	0.039	0.0578	0.01	0.01

4.2 Polycrystalline Simulation

The thermal neutron transmission spectra of imperfect single crystals display low-intensity valleys, which are direction-dependent based on the oriented regions of the mosaic blocks; the thermal neutron transmission spectra of polycrystalline materials shows sudden well-defined increase in intensity as a function of neutron wavelength. These steep increases in neutron transmission intensity are normally referred to as Bragg-edges, and these Bragg-edges materialize at wavelength locations that exceed the Bragg condition for coherent scattering by certain lattice planes. The position, height, and slope of the so called Bragg-edges are dependent on the number of crystallites oriented along the line of the neutron beam through the material being investigated. In this work, the simulation of a polycrystal copper sample is represented by segmenting a 1-cm-thick plate into 1000 columns. Each column contains 10,000

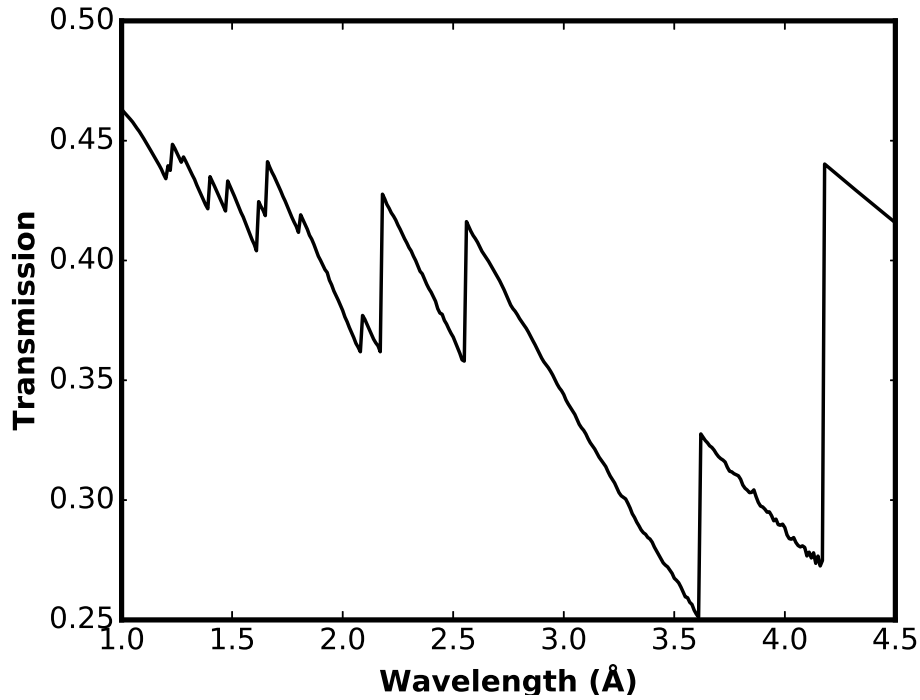


Figure 4.3: Simulated copper neutron transmission with 10 million distinct crystallites orientations.

distinct orientations with a uniform angular distribution. This setup represents the interaction of the neutron beam with a voxel of 10 millions crystallites with distinct orientations, and the simulation result is shown in Figure 4.3. The *Sinpol* simulation shown in Figure 4.3 resembles the neutron transmission spectra for copper measured in Kockelmann [97]; the shape and Bragg-edge locations are comparable. The high-frequency noise observed in the experimental data shown by Kockelmann [97] is due to neutron statistical noise and is not included in the simulations.

4.2.1 Voxel-Grain Ration

Simulations were performed to help determine impact of the number of crystal orientations on simulation results and to illustrate the effect of secondary extinction on polycrystalline neutron transmission. Figure 4.4 presents the calculated neutron

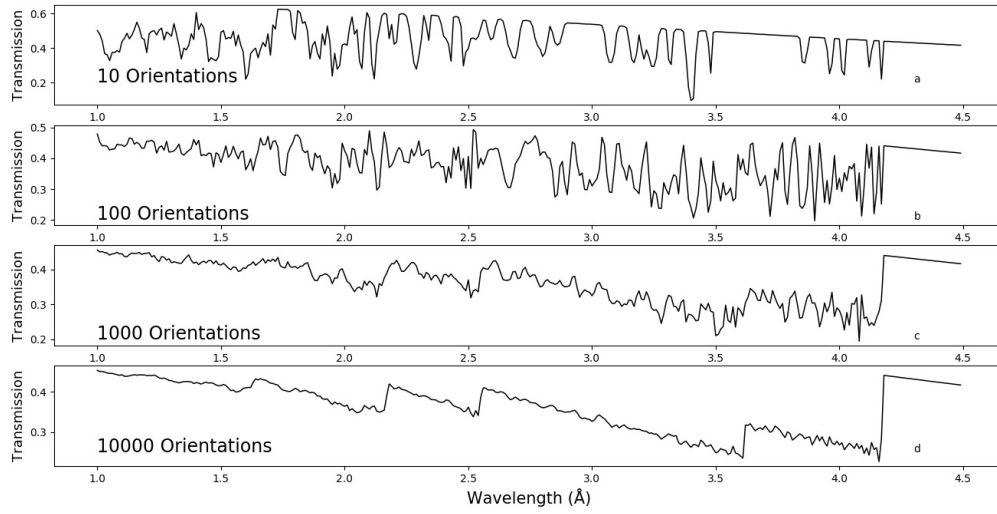


Figure 4.4: Copper neutron transmission for 10 distinct crystallites orientations, 100 distinct crystallites orientations, 1000 distinct crystallites orientations and 10000 distinct crystallites orientations.

transmission spectra for one column of a 1-cm-thick copper plate, with varying numbers of crystal orientations including 10, 100, 1000 and 10,000 orientations. The neutron transmission spectra for 10 and 100 distinct orientations are comparable to single crystal spectra, with well-defined peaks dependent on the crystallite orientations. The neutron spectra for 1000 distinct orientations displays a coarse spectra for a copper powder, with Bragg-edges starting to stand out. The *Sinpol* calculations for 10,000 distinct orientations is consistent with the measured neutron transmission spectra for copper found in Kockelmann [97] and those calculated in Figure 4.3. The high-frequency noise observed in the simulation is a result of the randomness or lack thereof in the distribution. The absence of diffraction above 4.2 angstroms results in a smooth line.

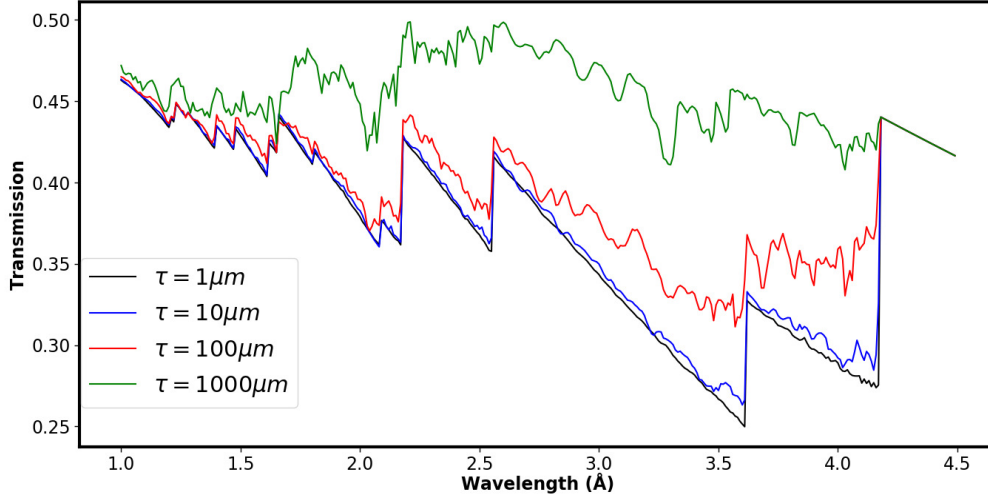


Figure 4.5: Neutron transmission simulations of copper polycrystals, with grain sizes of $\tau = 1000\mu\text{m}$, $\tau = 100\mu\text{m}$, $\tau = 10\mu\text{m}$, and $\tau = 1\mu\text{m}$.

4.2.2 Extinction

Figure 4.5 presents the neutron transmission simulation spectra for a 1-cm-thick copper plate segmented 1,000 times, with each segment consisting of a single column, with varying numbers of distinct crystal orientations including 10,100,1000 and 10,000. The neutron transmission of the four different numbers of orientations of grains per column represents the neutron simulation of polycrystals, with grain sizes of $1000\mu\text{m}$, $100\mu\text{m}$, $10\mu\text{m}$, and $1\mu\text{m}$ respectively. Simulations were performed to help determine the impact of grain sizes on neutron transmission simulation results and to illustrate the effect of extinction on polycrystalline neutron transmission. The difference in simulated neutron transmission intensity shown in Figure 4.5 illustrates the extinction effect on neutron transmission measurements. As the grain size decreases, the transmission intensity decreases. The extinction effect simulated here is less drastic than those reported by Sato [23] and are concentrated about the neutron Bragg-edges.

Based on the simulation data presented in Figure 4.4, it can be concluded that the number of grains probed in neutron transmission measurements may be of concern

for the Bragg-edge imaging method. If we consider 10^4 grains as a threshold value for visualizing the four first Bragg-edges in a fcc material, the extension of the image pixel Δx should surpass a minimum value:

$$\Delta x_{min} = 2.3 \sqrt{\frac{D^3[\text{mm}]}{g[\text{mm}]}}. \quad (4.4)$$

D is the diameter of a grain and g is the thickness of the sample. This means for a grain size of $10\mu\text{m}$ and a slab thickness of 10mm , the imaging resolution can reach $30\mu\text{m}$, whereas a larger grain size of $20\mu\text{m}$ and thinner samples of 1mm will drive the achievable imaging resolution toward $200\mu\text{m}$. The resolution limitations will be more drastic for performing tomographic reconstruction; in that case, the voxel dimension encompassing 10^4 grains will exceed the grain size, with a factor of 20 (at $D \approx 10\mu\text{m}$ voxel size becomes $\Delta x = 200\mu\text{m}$).

4.2.3 Log-normal Distribution of Grains

The polycrystalline simulation presented in Figure 4.4 assumed constant grain size within the material. Figure 4.6 presents neutron transmission simulations through a 1-cm-thick copper plate, using a log-normal distribution to represent the varying grain sizes that are typically found within engineered materials. Log-normal grain size distributions are commonly accepted to represent single-phase fully dense polycrystalline materials. They are parameterized [98] by the mean (c) and standard deviation (b_{LN}). Neutron transmission simulations of polycrystalline materials with varying standard deviation (b_{LN}) for a log-normal distribution are presented in Figure 4.6. Equation C.8 from Appendix C represents the current grain size value generated to follow the log-normal distribution; a relative standard deviation (c_v) of zero is consistent with a constant grain-size. Figure 4.6 presents the neutron transmission

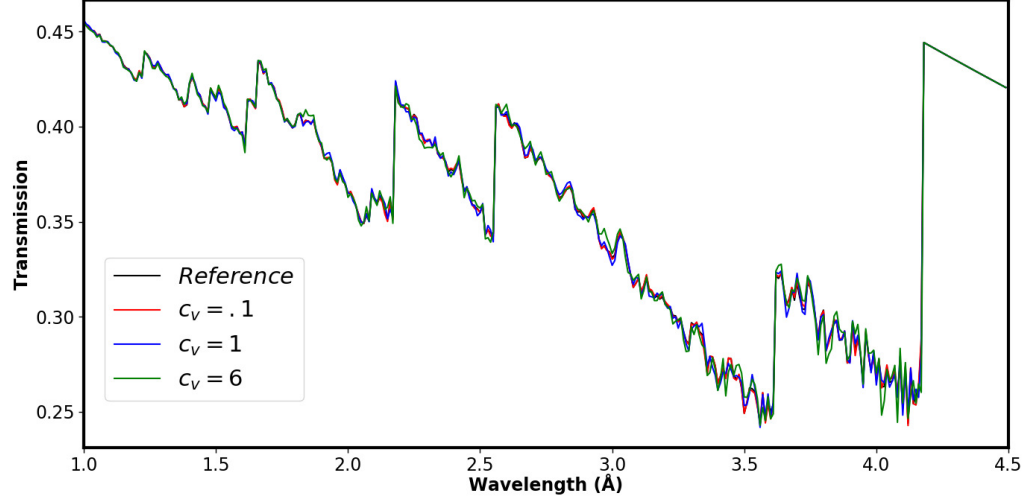


Figure 4.6: Neutron simulation through a 1-cm copper plate using a log-normal distribution to represent the grain size, with varying b_{LN} ; the mean size τ_v was kept to $1 \mu\text{m}$.

simulation of various c_v compared to that of a uniform distribution ($c_v=0$), as c_v increases, the distribution becomes broader, incorporating larger grains into the simulation. The influence of a broader distribution of grain sizes on neutron transmission results in a higher level of “noise”, but the positions and heights of Bragg-edges are preserved, suggesting that the mean grain size makes a good approximation. Figure 4.7 demonstrates the dependence of the standard deviation STD_{NT} of the neutron transmission simulation spectra on the relative standard deviation of the log-normal distribution, c_v . Note STD_{NT} is the standard deviation of the neutron transmission spectrum calculated for a log-normal distribution of grains relative to the reference spectrum corresponding to a constant grain-size. It also illustrates the effect of secondary extinction on the neutron transmission spectra as c_v increases. A c_v of 1 or less guarantees neutron transmission simulation will resemble that of a polycrystalline material. Ultimately a b_{LN} may be chosen that causes c_v to become very large and leads to a log-normal grain-size distribution that contains grains that will be on the order of the voxel size, and thus the neutron transmission simulation will resemble the neutron simulation of a single crystal as shown in Figure 4.8.

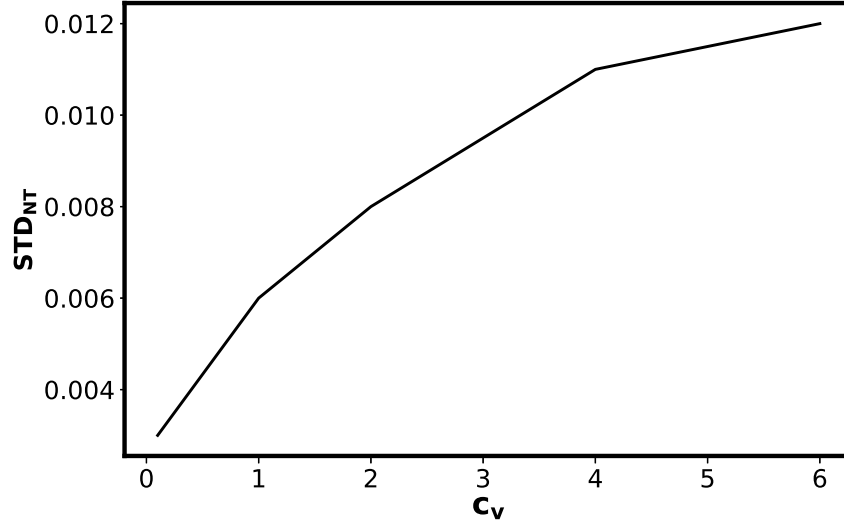


Figure 4.7: The relationship of the standard deviation of the neutron transmission simulation (STD_{NT}) to the relative standard deviation of a log-normal distribution (c_v).

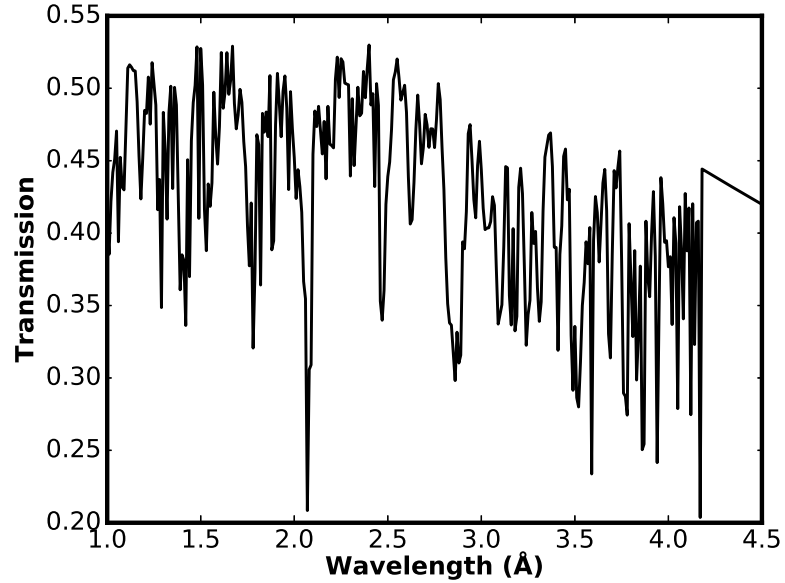


Figure 4.8: As the relative standard deviation (c_v) of the log-normal grain size distribution increases, the grain size population will move toward larger grain sizes. The neutron transmission simulation spectra of a log-normal distribution with $b_{LN} = 10$ resembles the neutron simulation spectra of a single crystal.

4.3 A Comparison with Experimental Results

To provide a direct verification of simulation results for polycrystalline materials, neutron transmission for polycrystalline nickel (fcc) and iron (bcc) was calculated using the simulator and compared with experimental values. The experimental measurements were performed at the VULCAN [99, 100] beam-line at the SNS and the experimental technique is described in a separate publication [101]. Figure 4.9 is the comparison of the relative intensity ($1-T(\lambda)$) for Bragg-edges obtained from experimentally measured spectra and calculated using the *Sinpol* simulator for iron and nickel. The solid black line is the relative neutron intensity for nickel obtained via the experimental measurement, and the red dashed line is relative neutron intensity for nickel calculated with *Sinpol*. The solid blue line is the relative neutron intensity for iron obtained via the experimental measurement, and the green dashed line is relative neutron intensity for iron calculated with *Sinpol*. The main physical parameters required for neutron simulation calculations of Ni and Fe are shown in Table 4.1. Figure 4.9 shows the comparison between experimental measurements and simulated neutron spectra. The calculations were performed for 2.42-mm-thick

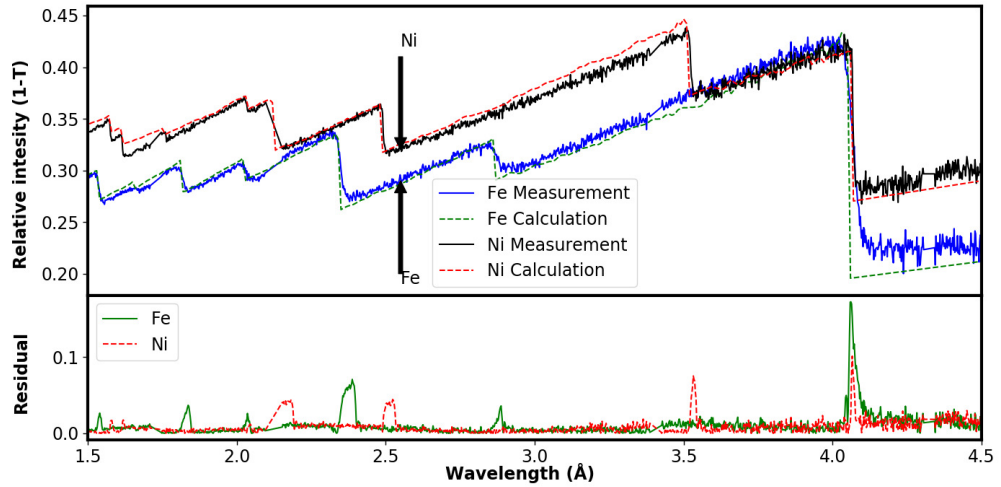


Figure 4.9: Comparison of simulated neutron transmission of Fe and Ni to neutron transmission measurement of Fe and Ni.

Ni plate segmented 500 times, with each segment consisting of a single column of 2420 distinct orientations; similarly calculations were performed for 3.12-mm-thick Fe plate segmented 375 times, with each segment consisting of a single column of 3120 distinct orientations. The lower part of Figure 4.9 shows the difference between the calculated and measured spectra. The errors in Bragg-edge locations are expected to be slightly larger due to the uncertainty surrounding proper binning of wavelength to locate the Bragg-edge. The main cause of differences in shape is likely due to *Sinpol* using a Gaussian instrumental function to convolve with the intensity while the VULCAN instrument function is typically modelled with a convolution of two back-to-back exponentials to a pseudo-Voigt function [102].

4.4 Conclusion

The *Sinpol* library implements the presented neutron transmission calculations for single crystals as a function of crystal structure, neutron energy and crystal orientation. Simulations of a copper single crystal as a function of rotation were performed to study peak locations and intensity. Furthermore, the neutron transmissions through polycrystalline material were simulated by defining a distribution of crystal orientations. Polycrystalline neutron transmission of copper was verified with measurements found in the literature; simulation of Ni and Fe powder were verified with measurements made at ORNL. The number of grains in a grain distribution were varied to study the impact of grain-number statistics on Bragg-edge visibility. A log-normal distribution was presented to study the impact of grain-size distribution on neutron transmission of a polycrystalline material. Effects of secondary extinction were observed on simulation of both single crystal neutron transmission and polycrystalline neutron transmission. The *Sinpol* simulator can be used to illustrate the wavelength dependencies of transmission and cross section to help neutron experimental planning and data analysis. The model does not correspond solely to neutron Bragg-edge transmission for polycrystalline samples

with small random grains, it allows the analysis of wavelength-resolved neutron transmission for single crystal, oligocrystals, and is expected to impact the grain orientation mapping techniques [103].

The *Sinpol* simulator presents the ability for the user to define angular distributions for neutron transmission calculations. Doing so allows for the simulation of a random distribution for powder materials. The ability for the user to define an angular distribution is quite useful, as it enables input of a probability density function to simulate texture for a polycrystalline sample; moreover a strain tensor can also be introduced to simulate three-dimensional strain.

Chapter 5

Extending Sinpol for Texture

This chapter is based on material that has been submitted for publication. Simulations of different texture components on fcc copper are presented, cube texture on Inconel 718 sample is simulated and compared to measurements. Studies of number of grains contributing to Bragg-edges are presented.

5.1 Introduction

Engineered materials are crystalline in the solid state, and most crystalline materials are polycrystalline materials made up of aggregates of single crystal grains. The shape of the grains is dependent on the solidification and the thermomechanical processes, whereas the orientation of the grains largely depends on the different stages of material processing. The material processes lead to the development of non-randomness of the grain orientations in a polycrystalline aggregate known as preferred orientations, or crystallographic textures. The presence of texture affects the behavior of crystalline material since physical, mechanical and chemical properties are often crystallographically anisotropic. Texture can be used to control properties in materials. For example, the values of the Poisson's ratio and the elastic modulus of materials vary with the crystallographic direction. To fully take advantage of the property of anisotropy, it is usually necessary to customize a texture for a particular

purpose. A large amount of research, both industrial and academic, has been published on the development of texture and its influence on mechanical properties [104].

The aim of texture measurement is to map the distribution of crystallographic orientations over as complete a section of orientation space as possible. Numerous techniques are used to collect information about texture with most employing a diffraction technique to measure the intensity of diffraction peaks which depend on the volume fraction of crystals in a sample that are in a diffracting position. A departure in the intensity ratio from the one that can be obtained by the calculation of intensities from structure factor is an indicator of texture in the sample. Diffraction techniques such as electron back-scattered diffraction (EBSD) in conjunction with scanning electron microscopy (SEM) are used to analyze microtexture in local regions [105, 106, 107, 108], while individual grains can be viewed using the technique of transmission electron microscopy (TEM) [109, 110]. These techniques are used for measuring microtexture and are able to directly provide the distribution of crystallographic grain orientation in a sample, but they lack the statistical means to provide orientation distribution in a bulk sample. In order to characterize texture in bulk polycrystalline samples X-ray diffraction or neutron diffraction is used. Since neutrons can penetrate thick specimens, they are ideal for texture measurements deep within samples.

The analysis of neutron diffraction texture measurement is based on pole figure measurement and pole figure inversions. A neutron pole figure measurement is essentially similar to a pole figure measurement by X-ray. It uses a Bragg angle fixed on a reflection of interest and then diffracted intensity is gathered from tilting the sample and rotating the sample through its own axis [104]. The pole figure texture technique is statistical; sizeable number of grains are simultaneous sampled without considering local arrangements and neighboring orientations. It

is a two-dimensional projection of the three-dimensional space and represents the probability of finding a pole to a lattice plane (hkl) in a specific sample direction. They are normalized to express this probability in multiple random distributions (m.r.d.). Pole figures are inherently incomplete as they refer only to the statistical distribution of a single direction. The incompleteness associated with pole figures can be compensated for by a statistical description of the grain orientation distribution using an orientation distribution function (ODF). The crystal orientation distribution function is defined by using two coordinate systems, the crystal's coordinate and the specimen's coordinate. The distribution is defined as a function of the grain orientation g and written as:

$$\frac{dV}{V} = f(g)dg \quad (5.1)$$

where $\frac{dV}{V}$ is the volume fraction of material with grain oriented in an interval g , $g+\Delta g$. Usually several pole figures are required to calculate ODF; however, if only an incomplete pole figure is present, the ODF is calculated using iterative procedures that are readily available in texture analysis software such as WIMV [111], ADC [112], and in the Matlab toolbox for quantitative texture analysis MTEX [113].

Neutron powder diffraction spectra are usually analyzed by software using the Rietveld method. Under the powder assumption, neutron cross section modeling [20] proves to be reasonable for treating neutron transmission data similarly to the Rietveld method [6]. The neutron Bragg-edge transmission is modeled as a function of the path length and the attenuation coefficient of the material. The attenuation coefficient is directly proportional to the total neutron cross section which is described as the summation of the coherent cross section, the thermal diffuse cross section, and the absorption cross section. Rietveld refinement programs simulate the effect of texture by implementing either the direct method or the Fourier method. With the

Fourier method, a finite number of harmonic ODF coefficients are refined in a similar way as crystallographic parameters with a non-linear least square approach. With the direct method, discrete ODF values are directly related to peak intensity values in the diffraction spectra.

The Rietveld codes implement the simplest approaches for texture corrections. Texture is roughly modeled using a textured axis linked to the sample symmetry, the crystallographic direction \vec{h} which tends to align with the previous axis, and to a texturation strength [114]. In neutron transmission models [20, 115] either the March-Dollase [116](MD) model or the R [117] factor has been implemented as an approach to texture correction. For neutron Bragg-edge texture calculation the coherent cross section (which is a function of wavelength, lattice spacing and structure factor) is modified with the March-Dollase preferred orientation function or the R [117] factor. The March-Dollase function is parameterized by the angle between the scattering vector and the preferred orientation axis, and by a refined parameter that describes the level of texture strength. The texture correction assumes a Gaussian distribution of the preferred orientation axis of the individual crystallites about the normal plane of the sample [114]. The MD correction functions assume an axially symmetric orientation distribution around the beam direction, and the formulations are only valid for single component textures. Another approach to modeling texture is to modified the coherent cross section with the more commonly used R factor [117]. It is a line integral around a circle in the pole figure of interest factor. The R factor is parameterized by the wavelength, lattice spacing , and the angle between the beam and the sample's direction. The texture correction is done by calculating the angular distribution of grain orientation by integrating the pole figure around a ring radius for a known sample orientation. It essentially counts the number of grains for which a certain crystal direction makes a specified angle with the incident beam.

In this work we use the *Sinpol* [95] tool to simulate neutron transmission using a single crystal to polycrystal approach, furthermore we try to assess the use of the neutron transmission for texture evaluation. *Sinpol* [95] calculates the neutron transmission for a given grain distribution within a voxel by calculating transmission for each individual grain in the distribution then combining them for a total voxel transmission value. The effect of texture is simulated by calculating the orientation distribution function in the voxel as a Gaussian function centered around an ideal texture component. The preferred orientation is modeled by considering a set of single crystal orientations representative for a specific ODF. The neutron transmission spectra are calculated for a sample that is discretized into voxels of uniform size. Our model calculates the neutron transmission for each grain within a voxel and combines them for a total voxel transmission value [95]. The neutron transmission through the voxel is written as contribution of all the grains

$$T_t(\lambda) = \prod_{i=1}^N T_i(g, \tau, W(\theta - \theta_B), \xi, \zeta, \lambda) \quad (5.2)$$

where T_i is the neutron transmission calculation of a grain as function of the grain orientation g , the grain size τ , the mosaic distribution within the grain W , θ is the angle between the incident beam and Bragg planes, θ_B the Bragg angle, the wavelength λ , the crystal parameters (ξ), and material parameters (ζ). The texture is implemented by entering the grain orientation g for each grain according to the distribution of individual orientations generated for a specific ODF. As an illustration, the calculation is demonstrated for cubic lattice symmetry; however, this ideal can be generalized to other symmetries. Calculations of deformation and recrystallization rolling texture for Al(fcc) are presented. A study of Bragg-edge statistic is realized. Cube texture on Inconel 718 is simulated and compared to experimental data measured at the Vulcan [118] instrument located at the Spallation Neutron Source (SNS) Oak Ridge, Tennessee. The next section describes the calculation of ODF

texture components based on three-dimensional Gaussian distribution functions in the orientation space.

5.2 Orientation Distribution Function

The modern era of texture analysis was initiated with the publication by Bunge [119] and Roe [120] of a mathematical method of pole inversion, which is used to calculate the orientation distribution density of grains in a polycrystal. Bunge [121] proposed the use of series expansion to ODF from experimental pole figures. In this formalism regions of negative values are unavoidable and ghost effects are introduced into the ODF. The ghost effects result from missing information on the odd part of the ODF and also from the series termination [122]. Several methods [123, 124, 125] have been proposed to eliminate the above-mentioned phenomena from ODF but they are beyond the scope of this paper. However, the intensity distribution of isolated texture components usually possesses a bell-shaped structure [126]. This structure can be represented with a standard Gaussian-shaped function. The Gaussian function is defined in orientation space as the orientation distance between a random location and the point in Euler space matching the ideal texture component. Following the argument of Mathies [126], a point in orientation space can be described by a rotation axis \vec{n} and rotation angle ω about the axis. The distance between two points $[\vec{n}_1, \omega_1]$ and $[\vec{n}_2, \omega_2]$ is the rotation angle, $\tilde{\omega}$, about the axis $\vec{n}_1 \times \vec{n}_2$ which transform one point into another. With this notation the standard Gaussian function is defined as:

$$\begin{aligned} f(S, \tilde{\omega}) &= N(S) \exp(\cos(\tilde{\omega})) \\ N(S) &= \frac{1}{I_o(S) - I_1(S)} \end{aligned} \tag{5.3}$$

where I_n are the modified Bessel functions, the value S is governed by the full width at half maximum b and varies between zero and infinity

$$S = \frac{\ln 2}{2 \sin^2(\frac{b}{4})} \quad b \leq 2\pi \quad (5.4)$$

at $S = 0$ the distribution is random and when S approaches ∞ it has the property of a delta function.

In this work the standard Gaussian distribution around an ideal texture component is used for generating a number of individual grain orientations. For rolling texture, the ideal texture component is described by the Miller indices in terms of the rolling plane, $\{hkl\}$, and the rolling direction, $\langle uvw \rangle$. The individual grain orientations are generated according to a simple scheme.

First the ideal texture orientation is expressed in term of the rotation matrix g and is given as:

$$g_{\{hkl\}\langle uvw \rangle} = \begin{pmatrix} \frac{u}{n} & \frac{kw-lv}{mn} & \frac{h}{m} \\ \frac{v}{n} & \frac{lu-hw}{mn} & \frac{k}{m} \\ \frac{w}{n} & \frac{hv-ku}{mn} & \frac{l}{m} \end{pmatrix} \quad (5.5)$$

where m and n are the magnitudes of $\{hkl\}$ and $\langle uvw \rangle$ respectively.

Next, a cumulative standard Gaussian distribution is used to calculate the orientation distances created by integrating equation (5.3),

$$F(s, \tilde{\omega}_o) = N(S) e^S \int_0^{\tilde{\omega}_o} \exp \left(- \ln 2 \frac{\sin^2 \frac{\omega}{2}}{\sin^2 \frac{b}{4}} \right) 4 \sin^2 \frac{\omega}{2} d\omega \quad (5.6)$$

which reduces to

$$F(S, z_o) = \frac{N(S)e^S \left(2 \sin \frac{b}{4}\right)^3}{2\pi} \int_0^{z_o} \frac{\exp(-\ln(2)z^2)z^2}{\sqrt{1 - \sin^2 \frac{b}{4}}} dz \quad (5.7)$$

where z is $\frac{\sin^2 \frac{\tilde{\omega}}{2}}{\sin^2 \frac{b}{4}}$. Equation (5.7) is solved numerically to retrieve $\tilde{\omega}$ the rotation angle. The value obtained for $\tilde{\omega}$ and the direction of the rotating axis \vec{n} expressed in angles φ and ϑ is then used to calculate the rotation matrix, \mathbf{a} , that links the crystal coordinate system to the ideal texture component reference system. The values of $\tilde{\omega}$, φ and ϑ are parameters that characterized the rotation operation g as coordinates in the Euler space. The rotation operation describes all possible orientations between the sample coordinate system and the crystal coordinate system, the space is finite and is characterized by $\tilde{\omega}, \vartheta \in \{0, \pi\}$ and $\varphi \in \{0, 2\pi\}$. The explicit expressions for the elements of the rotation matrix, \mathbf{a} , are given by Mathies [126]

$$\begin{aligned} a_{11} &= (1 - \cos \tilde{\omega}) \sin^2 \vartheta \cos^2 \varphi + \cos \tilde{\omega} \\ a_{12} &= (1 - \cos \tilde{\omega}) \sin^2 \vartheta \cos \varphi \sin \varphi + \sin \tilde{\omega} \cos \vartheta \\ a_{13} &= (1 - \cos \tilde{\omega}) \sin \vartheta \cos \vartheta \cos \varphi - \sin \tilde{\omega} \sin \vartheta \sin \varphi \\ a_{21} &= (1 - \cos \tilde{\omega}) \sin^2 \vartheta \cos \varphi \sin \varphi - \sin \tilde{\omega} \cos \vartheta \\ a_{22} &= (1 - \cos \tilde{\omega}) \sin^2 \vartheta \sin^2 \varphi + \cos \tilde{\omega} \\ a_{23} &= (1 - \cos \tilde{\omega}) \sin \vartheta \cos \vartheta \cos \varphi + \sin \tilde{\omega} \sin \vartheta \cos \varphi \\ a_{31} &= (1 - \cos \tilde{\omega}) \sin \vartheta \cos \vartheta \cos \varphi + \sin \tilde{\omega} \sin \vartheta \sin \varphi \\ a_{32} &= (1 - \cos \tilde{\omega}) \sin \vartheta \cos \vartheta \cos \varphi - \sin \tilde{\omega} \sin \vartheta \cos \varphi \\ a_{33} &= (1 - \cos \tilde{\omega}) \cos^2 \vartheta + \cos \tilde{\omega}. \end{aligned} \quad (5.8)$$

Finally, the rotation matrix transforming the sample coordinates into crystal coordinates is calculated by multiplying the matrices defined by equations 5 and 8.

To generate a finite set of orientations of grains, two arrays u and v containing N random numbers in the range of $[0,1]$ are generated. The two allow to define $\vartheta = a \cos(2u - 1)$ and $\varphi = 2\pi v$. An array, w , of N numbers in the range $[0,\pi]$ is generated with purpose of calculating z as a function of w . The rotation angle $\tilde{\omega}$ is calculated by the intergration of equation (5.7) and interpolation of z . With such an algorithm studies of the minimal grain value of N to reproduce a satisfactory ODF for rolling texture can be considered.

5.3 Neutron Simulation of Texture

For verification of the calculations, simulations for selected ideal orientations of face-centered cubic (fcc) copper samples are presented. The physical parameters required in the calculation are listed in Table 5.1. They are crystal lattice parameters, the Debye temperature Θ_D , the neutron coherent scattering length b , the neutron absorption cross section σ_{abs} , and the total bound scattering cross section σ_b .

Figure 5.1 presents wavelength-dependent neutron transmission spectra results for copper single crystal, copper single crystal neutron peak locations and intensity as a function of sample rotation, copper polycrystal neutron transmission Bragg-edges,

Table 5.1: Physical parameters for simulations of Cu, Al, and Inconel samples.

Element	Cu	Al	Inconel
Crystal Structure	fcc	fcc	fcc
Atomic Mass	63.55	26.98	60.67
Lattice Constant(Å)	3.61496	4.049	3.6
Θ_D (k)	344	429	345
b (fm)	7.718	3.449	10.3
σ_{abs} (barns)	3.78	.231	3.52
σ_b (barns)	8.035	1.503	10.73

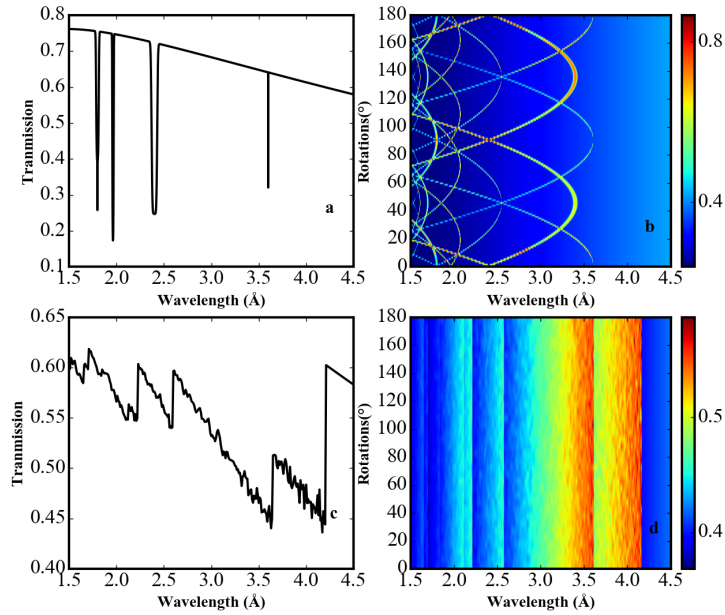


Figure 5.1: *Sinpol* transmission simulation results for copper: (a) single crystal at one orientation, (b) single crystal over rotations round one axis, (c) powder at one orientation, and (d) powder over rotations around one axis.

and neutron Bragg-edges location and intensity as a function of crystal rotation. Figure 5.1-a shows the neutron transmission simulation spectra for a 1-cm thick copper single crystal aligned with the (100) plane normal to the incident beam. Figure 5.1-b neutron transmission Bragg dips intensity and location as a function of rotation angle around a vertical axis. The sample is rotated around the vertical, similar to the case presented in Dessieux [95] et al. As diffraction dips approach their Bragg-edge conditions, higher intensity and less broadening induced by mosaic is observed. Figure 5.1-c shows the neutron transmission spectra for a polycrystal copper sample characterized by a single column containing 10000 distinct orientations as shown by Dessieux [95] et al. The spectra are characterized by Bragg-edges or sudden well-defined increase in intensity at specific wavelengths. This simulation bears resemblance to the neutron transmission spectra for copper measured in Kockelmann [97] in that the shape of the neutron transmission is consistent with the measured

transmission spectra.

Simulations were performed to help determine the minimal value of grains necessary to distinguish the effect of texture on neutron transmission spectra. Figure 5.2 presents the calculated neutron transmission spectra for one column of a 1-cm-thick copper plate, with a varying grain population including 10, 100, 1000, and 10000 grains. The neutron transmission of the four different numbers of orientations of grains per column represents the neutron simulation of polycrystals, with grain sizes of 1000 μm , 100 μm , 10 μm , and 1 μm , respectively. In addition to threshold grain value, effects of extinction are studied on neutron transmission spectra. The four different orientation numbers are compared to a reference neutron transmission that was calculated by segmenting a 1-cm-thick copper plate 10 times, with each segment consisting of a single column of 10000 orientations. An ideal cube texture component, $\{001\}\langle 100 \rangle$ with a FWHM of 10 degrees was considered in these simulations. The neutron transmission spectra for 10 and 100 orientations both show coarse spectra with formation of the Bragg-edge at wavelength 3.62 angstroms and their relative differences when compared to the reference case are 10% and 2% respectively. The 10 orientations spectra shows increase in transmission intensity due to extinction. The neutron transmission spectra for 1000 and 10000 orientations are comparable such that Bragg-edges are identifiable at 1.8 angstroms and 3.62 angstroms; furthermore, the final shape of the curve is readily observed with 1000 orientations. When compared to the reference case the relative difference is less than 1%, 0.9% and 0.3% respectively. To obtain Bragg-edges with random texture, the threshold value has been shown to be 10000 distinct orientations by Dessieux [95] et al. The threshold value decreases by an order of magnitude for texture simulations. The reduction in threshold value can be attributed to sampling statistics since the range in wavelength necessary for Bragg-edge measurement is not as broad as the range needed for neutron transmission texture measurement. Still, in this work we will use the threshold of 10000 orientations for simulations.

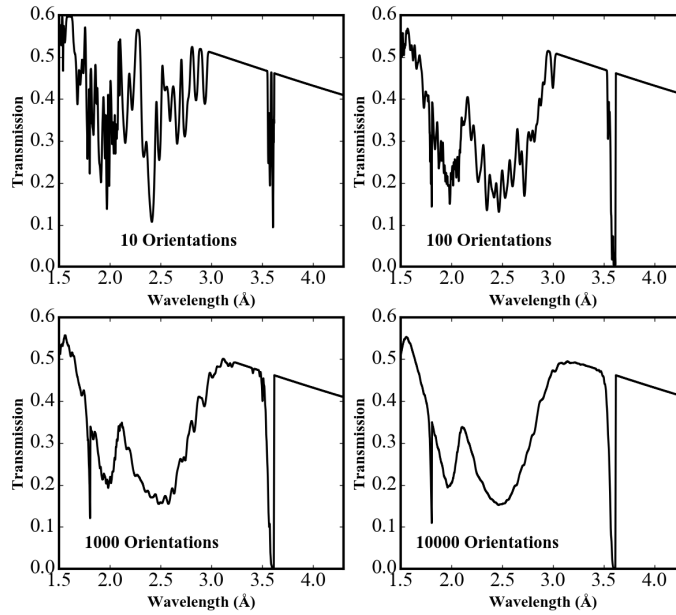


Figure 5.2: Cube texture neutron transmission simulation spectra for copper sample with populations of 10 grains, 100 grains, 1000 grains, and 10000 grains.

Figure 5.3 contain the pole figures and inverse pole figures that demonstrate the grain distribution that will be used to calculate the neutron transmission spectra for the cube component. The pole figures and inverse pole figures were obtain by means of MTEX after generating a population of 10000 grains following the Gaussian shaped distribution for the $\{001\}\langle 100 \rangle$ components. Figure 5.3 presents wavelength-dependent transmission simulation results for cube texture. Figure 5.3c and 5.3e represent the transmissions simulation results at 0 and 90 degrees, which are almost identical. In the Figure 5.3d, the change of the complement of transmission ($1-T$) is shown, when the sample is rotated 90 degrees around the vertical axis. Effects of both single crystal and polycrystalline powder are observed. The observed faint edges located at the Bragg-edge wavelength positions depict the fraction of random grains contributing to the neutron transmission signal. The bright areas are contributions from single crystal; they are low-intensity valleys, which are direction-dependent

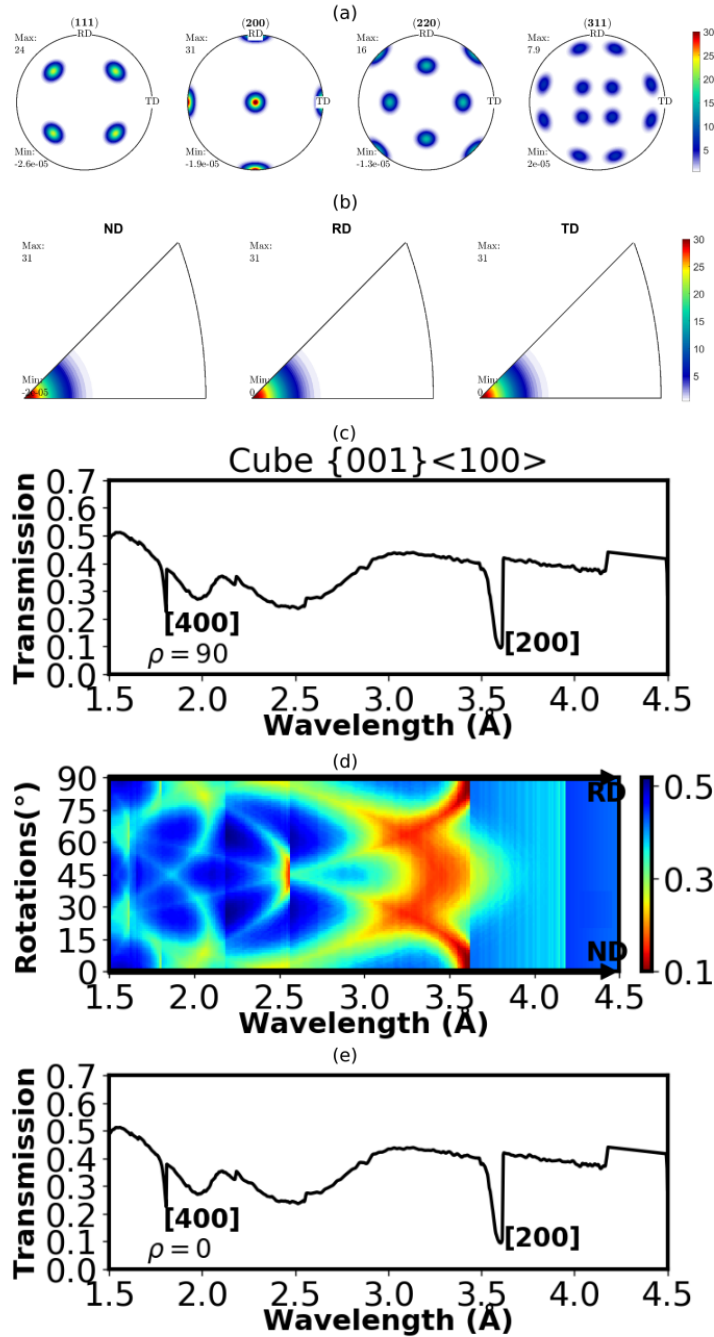


Figure 5.3 *Sinpol* simulated cube texture ideal component pole figures (a) with associated inverse pole figure (b) and corresponding neutron transmission simulation for a copper sample with its RD aligned along the neutron beam (c), (d) map of sample rotated along the vertical axis, and (e) copper sample with its ND aligned along the neutron beam.

based on the oriented regions of the mosaic blocks.

Similar neutron transmission simulations were performed to characterize the goss, brass, copper and S components found in fcc materials. The ideal component for the goss component is represented by $\{011\}\langle 100\rangle$. Note that the goss component differs from the cube component in the rolling plane. The $\{011\}$ pole is aligned parallel to the sample's normal direction and the other poles are tilted 45 degrees from the rolling direction. Figure 5.4a and 5.4b are the pole figures and inverse pole figures obtain by MTEX via the Gaussian distribution calculated by *Sinpol*. Figures 5.4c-e are the transmission simulation results for the neutron beam align with the rolling direction; the wavelength-dependent simulation results as a function of crystal rotation; and the transmission simulation results for the neutron beam align with the normal direction. With neutron beam align along the normal direction, the goss component is identifiable by a sharp dip at the $[220]$ Bragg-edge location. The brass component is very similar to the goss component in that it is also associated with the (011) pole, unlike the the goss component in which the rotation is performed about the normal direction. The ideal component for the brass component is represented as $\{011\}\langle 211\rangle$, Figure 5.5 are the pole figures and inverse pole figures obtain by MTEX via the Gaussian distribution calculated by *Sinpol*. Like the goss component, the brass component is characterized by a sharp dip at the $[220]$ Bragg-edge location and is shown in Figure 5.5e. Figure 5.6a and 5.6b show the pole figures and inverse pole figures for the copper component, which display a low distribution of crystallographic grains along the normal direction $\{112\}$ and higher grain distribution along the rolling directions $\langle 111\rangle$. Figure 5.6e is the neutron transmission simulation for the copper position, it is characterized by a sharp dip in the (422) Bragg-edge location. Figure 5.7 show pole figures and inverse poles figure for the S component, which display lower symmetry crystallographic direction along normal direction and rolling direction ($\{123\}$ and $\langle 634\rangle$). In this case, the transmission features (Fig.5.7c and 5.7e) are less

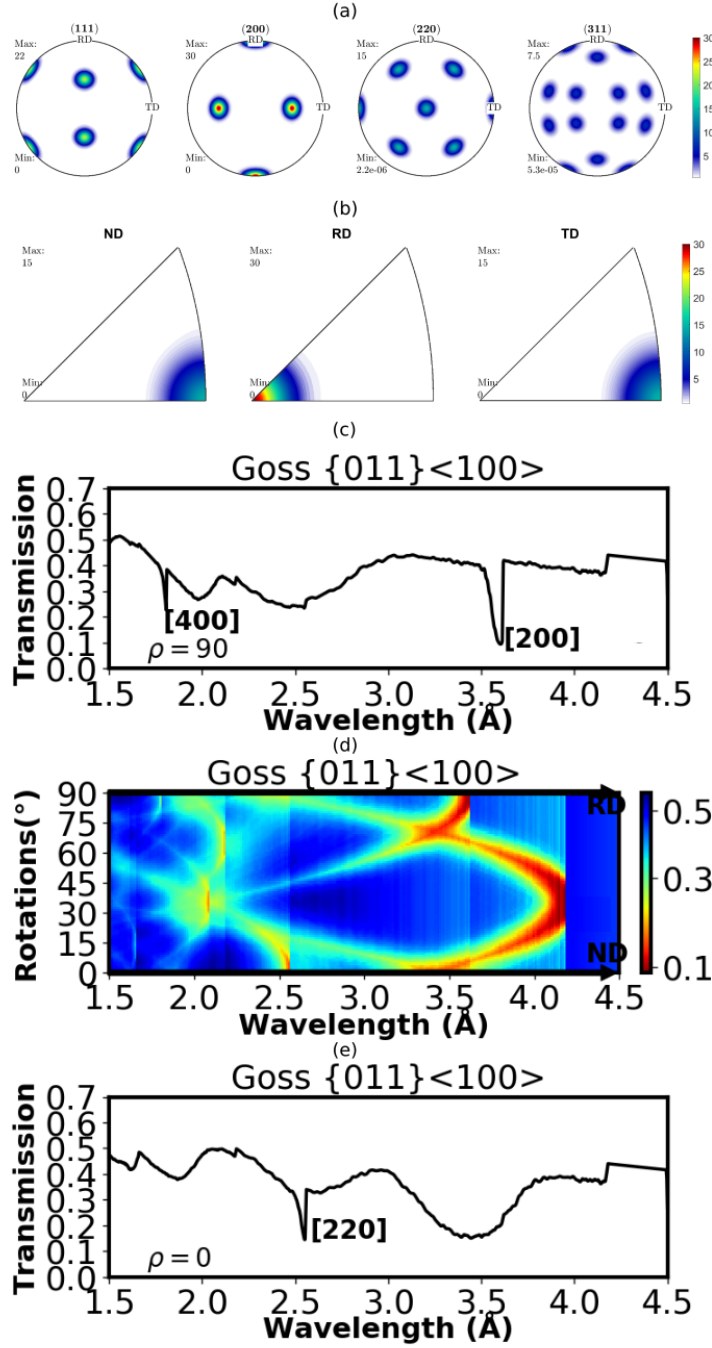


Figure 5.4 *Sinpol* simulated goss texture ideal component pole figures (a) with associated inverse pole figure (b) and corresponding neutron transmission simulation for a copper sample with its RD aligned along the neutron beam (c), (d) map of sample rotated along the vertical axis, and (e) copper sample with its ND aligned along the neutron beam.

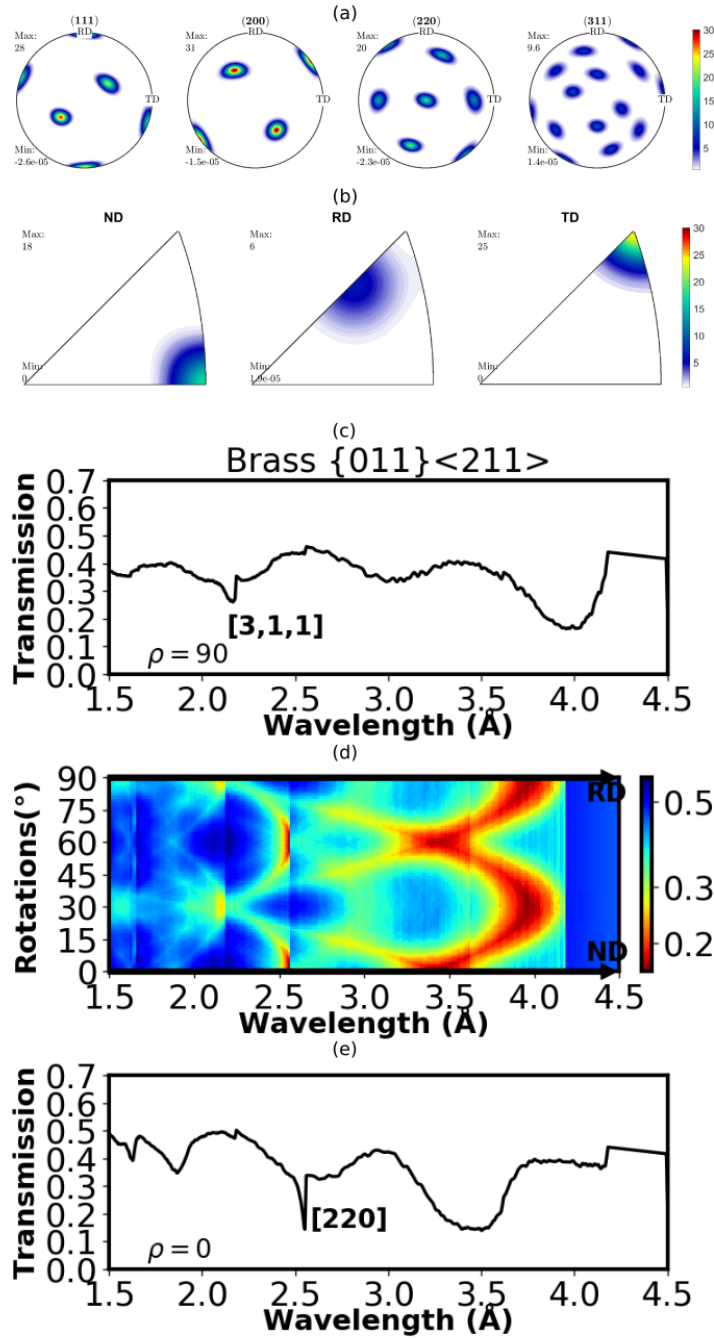


Figure 5.5 *Sinpol* simulated brass texture ideal component pole figures (a) with associated inverse pole figure (b) and corresponding neutron transmission simulation for a copper sample with its RD aligned along the neutron beam (c), (d) map of sample rotated along the vertical axis, and (e) copper sample with its ND aligned along the neutron beam.

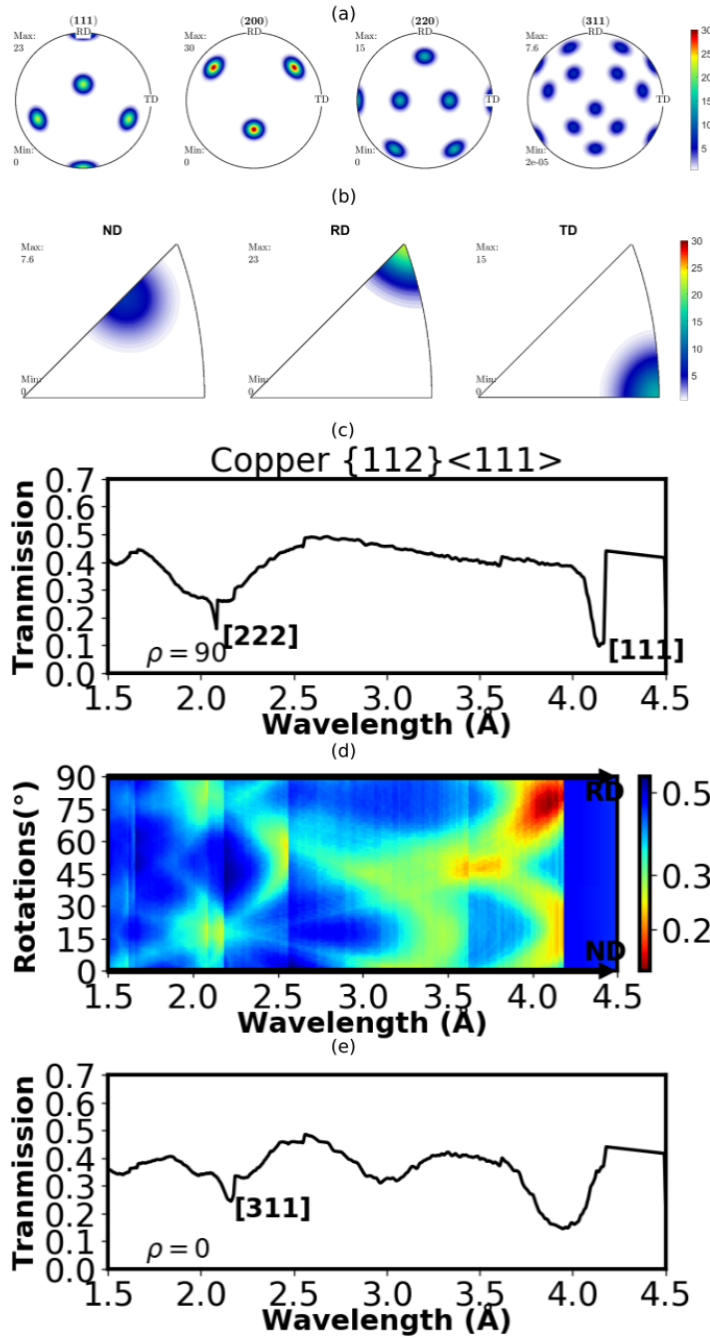


Figure 5.6 Sinpol simulated copper texture ideal component pole figures (a) with associated inverse pole figure (b) and corresponding neutron transmission simulation for a copper sample with its RD aligned along the neutron beam (c), (d) map of sample rotated along the vertical axis, and (e) copper sample with its ND aligned along the neutron beam.

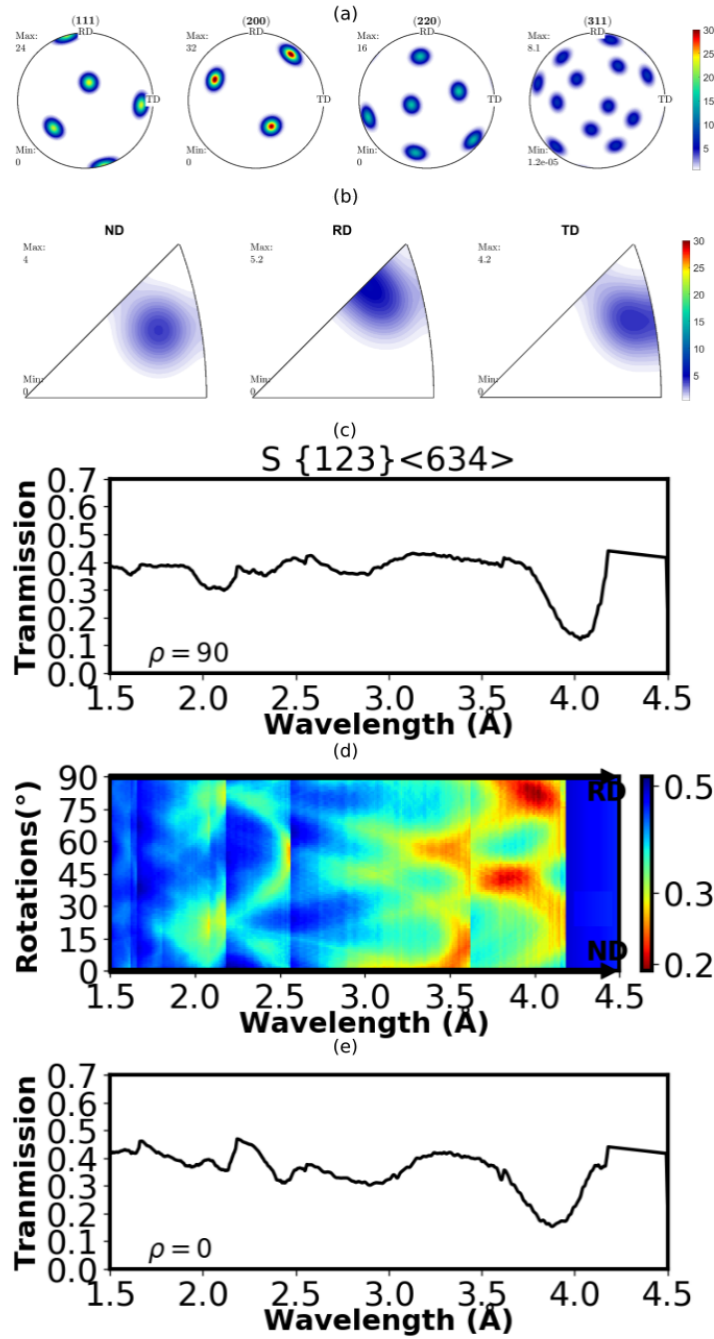


Figure 5.7 *Sinpol* simulated S texture ideal component pole figures (a) with associated inverse pole figure (b) and corresponding neutron transmission simulation for a copper sample with its RD aligned along the neutron beam (c), (d) map of sample rotated along the vertical axis, and (e) copper sample with its ND aligned along the neutron beam.

pronounced and Bragg-edge enhancement are not visible.

Figures 5.3d, 5.4d, 5.5d, 5.6d and 5.7d present the neutron transmission simulations of the cube, goss, brass, copper, and S texture components as the sample is rotated around the vertical direction by the angle ρ from 0 to 90 degrees. At ρ equals to 0 degrees the beam is aligned with the sample's normal direction and at ρ equals to 90 degrees the beam is aligned with the sample's rolling direction. Table 5.2 shows the Bragg-edges and Bragg-edges location which can be used to characterize the texture of interest at ρ equals to 0 degrees and 90 degrees. The rotation of the sample around the vertical enabled the characterization of texture and identification of texture components. Neutron transmission through the sample at 0 degrees correlates with the $\langle hkl \rangle$ indexes of the ND, as at 90 degrees the transmission correlated with the rolling preferential direction $\langle uvw \rangle$.

Characterization of the evolution of texture in materials during the manufacturing process is necessary to ensure that the final product has the required properties. One process, which was often considered, is thermally activated recrystallization in various types of metallic alloys, in particular Al based alloys. In neutron diffraction measurements the characterization of texture evolution is usually two-fold; first the texture components associated with the rolling deformation are identified as shown Li [127] et al, after which the texture components associated with the thermally-activated recrystallization process are identified as exemplified in Sidor [128] et al. Texture evolution during annealing of a cold-rolled Al2%Mg alloy was recently

Table 5.2: Enhanced Bragg-edges for different texture components with the sample at two selected angles.

	$\{001\}\langle 100 \rangle$		$\{011\}\langle 100 \rangle$		$\{011\}\langle 211 \rangle$		$\{211\}\langle 111 \rangle$		$\{123\}\langle 634 \rangle$	
ρ	[hkl]	$\lambda(\text{\AA})$	[hkl]	$\lambda(\text{\AA})$	[hkl]	$\lambda(\text{\AA})$	[hkl]	$\lambda(\text{\AA})$	[hkl]	$\lambda(\text{\AA})$
0	[200]	3.61	[220]	2.56	[220]	2.56	[311]	2.18	*	*
90	[200]	3.61	[200]	3.61	[311]	2.18	[111]	4.174	*	*

reported in a separate publication [129]. The experimental neutron diffraction results were analyzed by using a similar single crystal to polycrystal approach. Here we present the simulation of transmission patterns corresponding to the science case described in the previous publication [129]. Figures 5.8a, 5.8b, 5.9a, and 5.9b show pole figures and inverse pole figures of the deformation and recrystallization cases measured at the VULCAN neutron diffractometer. Figures 5.8c-d and 5.9c-d show neutron transmission simulations obtained using ODFs for deformation and recrystallization cases which were constructed by means of the MTEX tool and used to create a 10000 grains population. Figure 5.8c-d shows neutron transmission simulation spectra for the deformation case. In the normal direction (ND) strong intensities in the case of (311) and (220) are observed while the contributions for (111) and (200) are minimal as shown by the inset in Figure 5.8d. In the rolling direction strong intensities in (111) are observed, both the lack of intensity from (200) and the absence of (220) on the transmission curve is foretold by the inverse pole figure. Figure 5.9c-d shows neutron transmission simulation spectra for the recrystallization case. In both normal direction and rolling direction the neutron transmission spectra is characterized as a cube texture showing a strong preference toward the (200) and strong intensity contributions from the (111) plane primarily in the normal direction. Therefore, when characterizing the evolution of texture in bulk materials the neutron transmission can be used in compliment of the diffraction technique.

5.4 Grain Statistics at Bragg-edges

Dessieux [95] et al have demonstrated that a total of 10000 distinct grain orientations are suitable to simulate Bragg-edges in a 1-cm thick sample. Further studies have been performed to quantify the number of grains that contribute to particular Bragg-edges in random texture and selected texture components. The ODF for each ideal texture component was calculated using 10000 grains and with each grain containing a mosaic of 0.5 degrees. Grains were selected based on the proximity of the diffracting

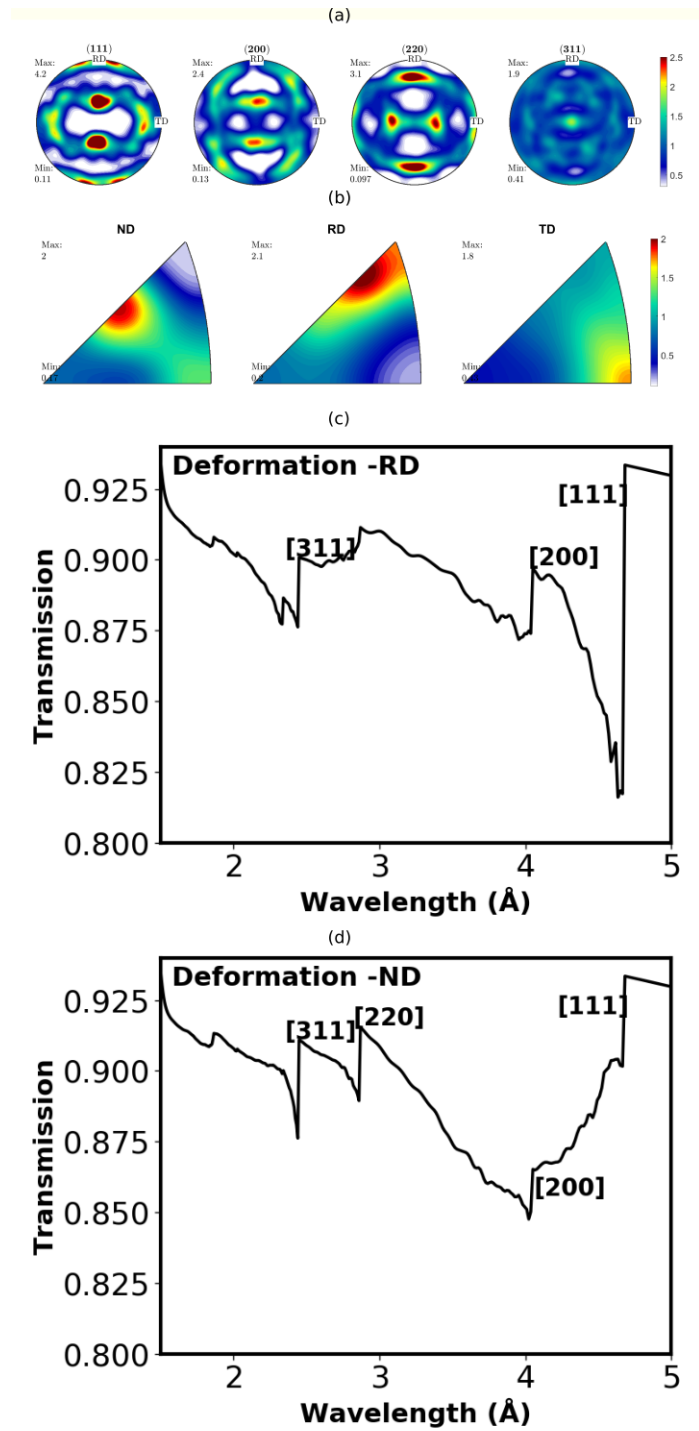


Figure 5.8 Ex-situ deformation rolling textures of Al-2%Mg alloy obtained at VULCAN neutron diffractometer (a) pole figures with associated inverse pole figure (b) and corresponding neutron transmission simulation for Al-2%Mg sample with its RD aligned along the neutron beam (c), and (d) Al-2%Mg sample with its ND aligned along the neutron beam.

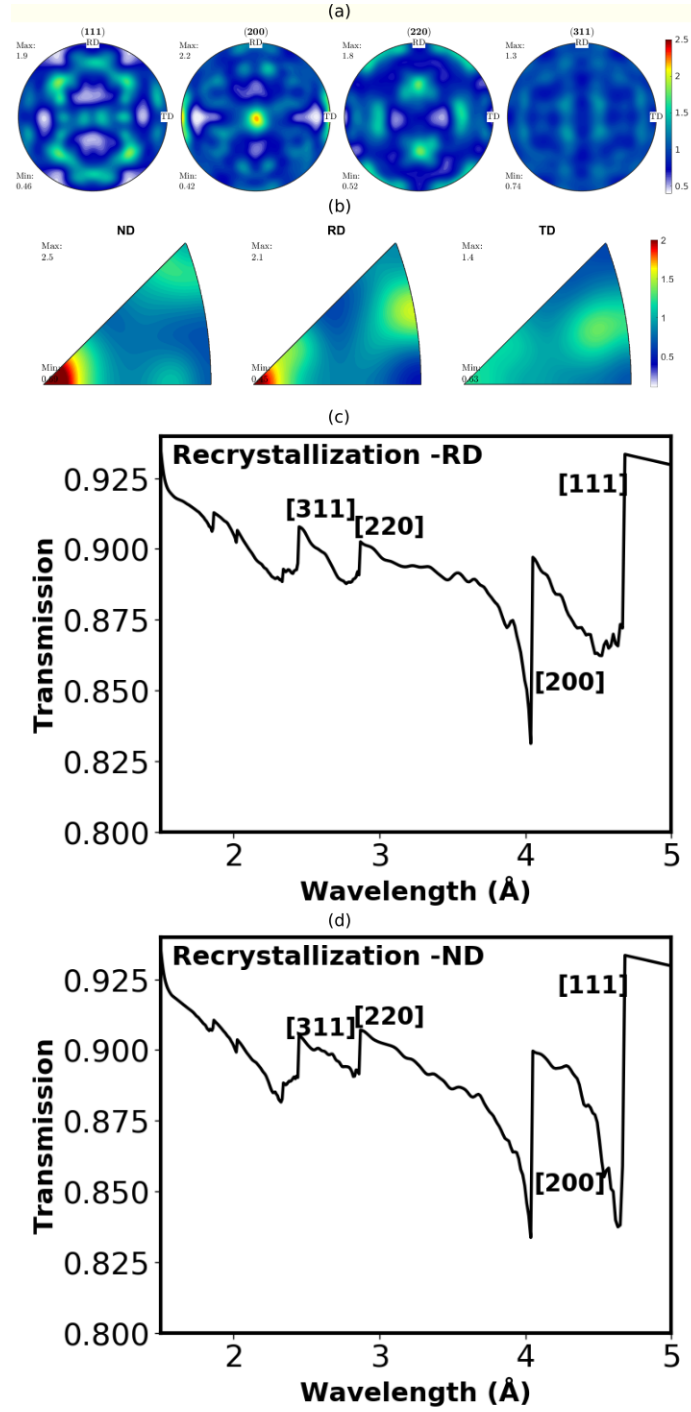


Figure 5.9 Ex-situ recrystallization textures of Al-2%Mg alloy obtained at VULCAN neutron diffractometer (a) pole figures with associated inverse pole figure (b) and corresponding neutron transmission simulation for Al-2%Mg sample with its RD aligned along the neutron beam (c), and (d) Al-2%Mg sample with its ND aligned along the neutron beam.

wavelength to the nominal wavelength value of the [111] Bragg-edge over a range 0.2 angstroms. This was done to evaluate the number of grains necessary to achieve the Bragg-edges' full amplitude. Figure 5.10 presents the relative intensity(1-T) versus wavelengths illustrating the difference in intensities for different number grains contributing to [111] Bragg-edge. It was found that a number of 100 grains are necessary to achieve the full amplitude of the [111] Bragg-edge. To compute the number of grains contributing to each Bragg-edge in the neutron transmission of a random textured sample, a window of 6σ around the nominal wavelength value was imposed. Tables 5.3 and 5.4 show the number of grains contributing to each Bragg-edge for a random textured copper sample at $\rho = 0$ degrees and 90 degrees respectively. Larger number of grains contributing to Bragg-edges located at lower wavelengths is observed. Each Bragg-edge acts as a filter in the orientation space and the corresponding pole figures are shown in Figure 5.11. The same procedure was applied for selected texture components on a copper sample and Tables 5.3 -5.4 demonstrate the dramatic change of grain sampling as textured sample is rotated for two selected angles. The calculation for each texture component was repeated ten times and the standard deviation is presented as the error. The contribution of grains per Bragg-edge as the sample is rotated again shows that to characterize texture with the neutron transmission technique, two measurement are necessary one along the normal direction and the second along the rolling direction.

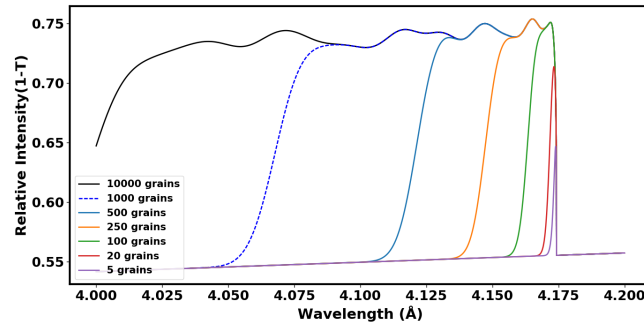


Figure 5.10 Illustration of number grains contributing to [111] Bragg-edge for a copper sample.

Table 5.3: Number of grains contributing to Bragg-edges of different texture components with the sample at $\rho = 0$ degrees.

	[111]	[200]	[220]	[311]	[331]	[420]
Random	116 \pm 19	88 \pm 18	173 \pm 36	341 \pm 63	342 \pm 67	345 \pm 66
{001} \langle 100 \rangle	0	4988 \pm 40	0	0	0	0
{011} \langle 100 \rangle	0	0	4993 \pm 35	0	278 \pm 18	7 \pm 3
{011} \langle 211 \rangle	0	0	5556 \pm 44	0	108 \pm 11	6 \pm 3
{112} \langle 111 \rangle	2 \pm 1	0	0	672 \pm 20	0	0
{111} \langle 112 \rangle	5007 \pm 47	0	0	0	0	0
{123} \langle 634 \rangle	0	0	0	33 \pm 5	346 \pm 20	9 \pm 2

Table 5.4: Number of grains contributing to Bragg-edges of different texture components with the sample at $\rho = 90$ degrees.

	[[111]	[200]	[220]	[311]	[331]	[420]
Random	116 \pm 19	88 \pm 18	173 \pm 36	341 \pm 63	342 \pm 67	346 \pm 65
{001} \langle 100 \rangle	0	4986 \pm 32	0	0	0	0
{011} \langle 100 \rangle	0	4961 \pm 37	0	0	0	0
{011} \langle 211 \rangle	2.9 \pm 1.3	0	0	706 \pm 27	3 \pm 2	0
{112} \langle 111 \rangle	5015 \pm 40	0	0	0	0	0
{111} \langle 112 \rangle	2 \pm 1	0	0	673 \pm 24	2 \pm 1	0
{123} \langle 634 \rangle	26 \pm 6	0	0	46 \pm 3.0	79 \pm 6.0	0

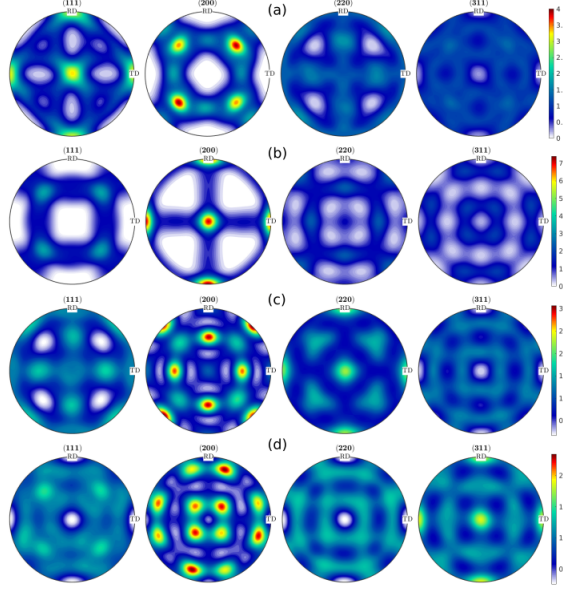


Figure 5.11 Pole figures representing the filtering of orientation space in a copper sample, (a) [111] Bragg-edge, (b) [200] Bragg-edge, (c) [220] Bragg-edge, and (d) [311] Bragg-edge.

5.5 A Comparison with Experimental Results

Cube texture simulation was directly verified by comparison with experimental measurement. The verification shows the feasibility and usefulness of modeling texture in engineered materials with the neutron transmission technique. Neutron transmission measurements were performed on the Ni base super-alloy Inconel 718. The experimental measurements were performed at the VULCAN [118, 130] beam-line at the SNS located in Oak Ridge, Tennessee. Details on the fabrication on the Inconel sample and the technique to control the texture within the sample are described in Dehoff [131] et al. The neutron transmission measurement is described in a separate publication [132]. For compound engineered materials such as Inconel, the cross sections necessary for calculation are dependent on the chemical composition of each atomic species present. Table 5.5 present the weighted fraction for each element present in the Inconel 718 sample so that the theoretical cross sections of the Inconel compound can be calculated using

Table 5.5: Nominal chemical composition of Inconel 718 powder in weight percent (wt.%).

Element	Ni	Fe	Cr	Mo	Nb	Cu	Al	Ti	C
Wt. %	Bal.	18.5	18.5	3	5	0.15	0.5	1	0.05

$$\sigma = \frac{1}{v_m} \sum_j \frac{w_j \sigma_j}{A_j} \bigg/ \sum_j \frac{w_j}{A_j} \quad (5.9)$$

where A_j is the atomic weight of each species, w_j is the weighted fraction of each species, by definition $\sum_j w_j = 1$, σ_j the cross section, and v_m is the normalized molecular volume given by

$$v_m = \sum_j a_j v_j \quad (5.10)$$

with v_j the molecular volume of each component species, and a_j the atomic fraction of each component species. The meso scale cross sections are presented in Table 5.1.

Figure 5.12 shows the comparison of the relative intensity ($1-T(\lambda)$) for Bragg-edges obtained from experimentally measured spectra and calculated using the *Sinpol* simulator for Inconel untextured sample. The calculation was performed for a 5.5-mm-thick Inconel plate segmented two times, with each segment consisting of a single column of 5500 distinct orientations for a total of 11,000 distinct orientations. The lower part of Figure 5.12 shows the difference between the calculated and measured spectra. The errors in Bragg-edge locations are expected to be slightly larger due to the uncertainty surrounding proper binning of wavelength to locate the Bragg-edge. This simulation was performed to calibrate the background parameters before performing the texture calculations.

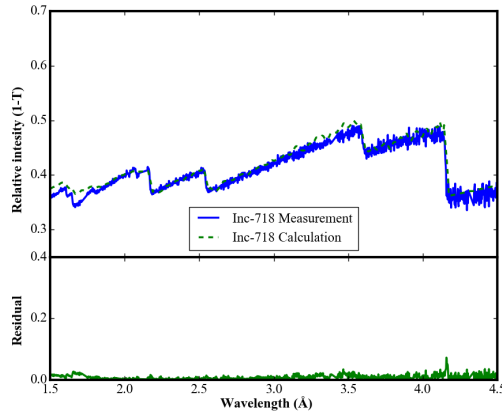


Figure 5.12 Comparison of simulated neutron transmission of Inconel-718 to neutron transmission measurement of Inconel-718.

Figure 5.13 presents pole figures measured at the Vulcan beam line using a two axis goniometer as described in Ma [133] et al. The complete ODF was derived by using the MTEX software. The sample exhibits strong cube texture component visible in the (111) and (200) pole figures which show an asymmetrical broadening around the ideal location of the texture component (see Figure 3). Figures 5.14 displays the relative intensity ($1-T(\lambda)$) as a function of wavelength when the sample is rotated by the angle ρ about the rolling direction from 0 to 90 degrees in steps of 15 degrees. The solid blue line is the relative neutron intensity for Inconel obtained via the experimental measurement, the red dashed-line is relative neutron intensity for Inconel texture simulation using the ODF calculated with the cube Gaussian approximation at 15 degrees FWHM (Ideal PF Sim), and the black dashed-line is relative neutron intensity for Inconel texture simulation using the ODF calculated from measured pole figures using MTEX (Measured PF Sim)).

At the reference angle of 0 degrees the high intensity of the (200) Bragg-edge indicates the grains are preferentially orientated with the (200) plane along the neutron beam. As the sample rotates, significant variations in the shape of the spectra is observed, which reflects the effect of the preferred crystallographic structure in the

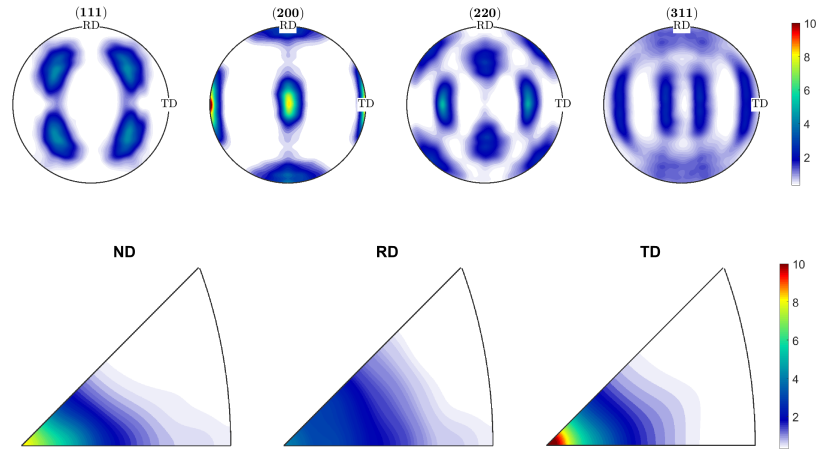


Figure 5.13 Pole figures of (111), (200), (220) and (311) planes of the Inconel-718 sample with cube texture obtained by neutron diffraction texture measurements at VULCAN

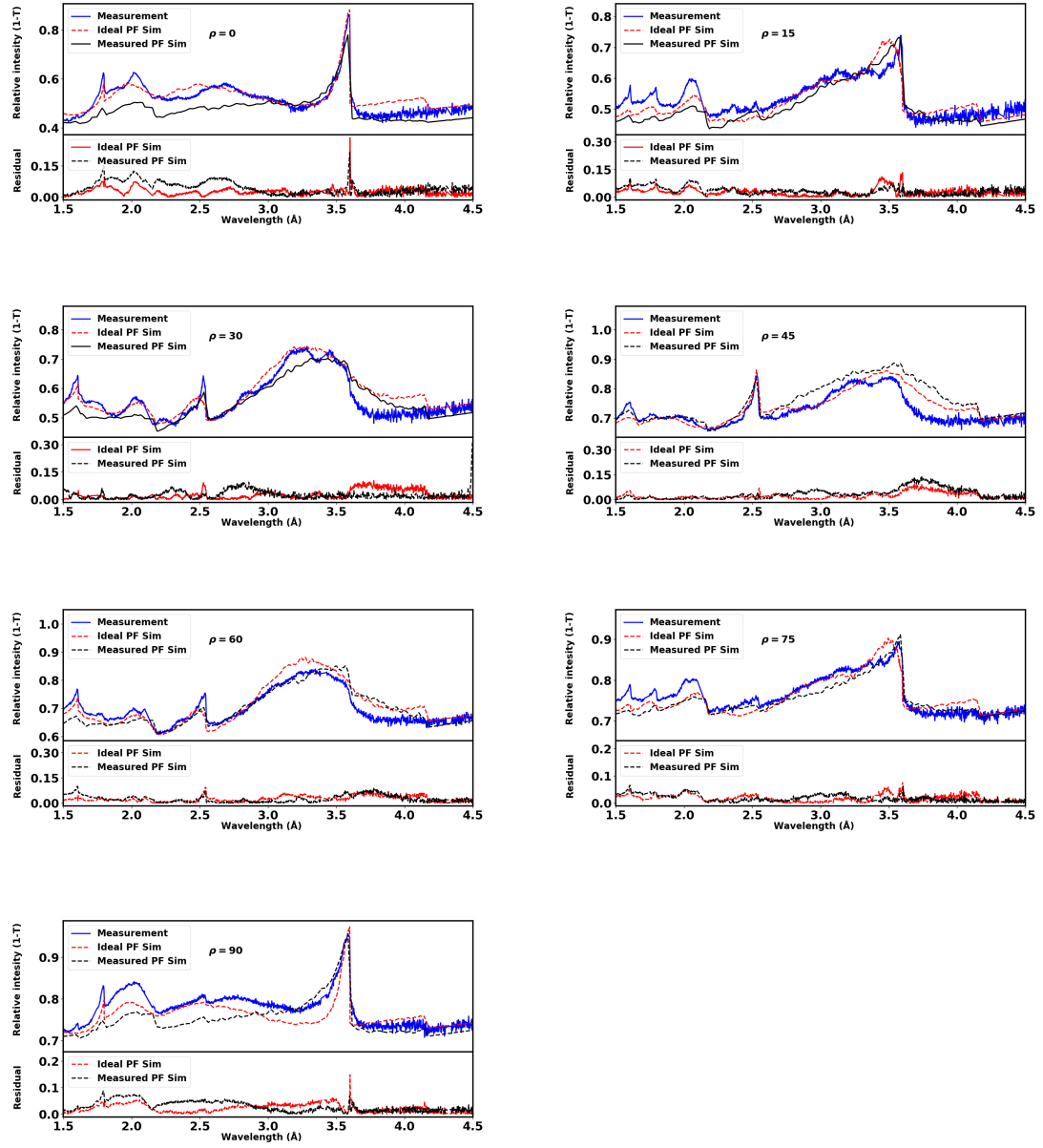


Figure 5.14 Comparison of simulated neutron transmission of Inconel-718 sample with cube texture using ODF from *Sinpol* and MTEX and neutron transmission measurement of Inconel sample with cube texture as a function of sample rotation from 0 degrees to 90 degrees in 15 degrees

sample. The intensity of the (200) Bragg-edge is reduced moderately as the sample rotates, at 45 degrees the (200) Bragg-edge is absent and the spectra is characterized by the high intensity of the (220) Bragg-edge. The (200) Bragg-edge reappears at 75 degrees and is again at high intensity at 90 degrees which resembles the spectra at 0 degrees.

Surprisingly, for some angles, a better fit was obtained by using the simulated Gaussian ODF, rather than MTEX generated ODF from experimental measurements. This effect can be explained either by the fact that the additional spread in pole figures is the result of the instrumental angular broadening, or the average texture in the diffraction measurement differs from that measured in transmission, due to different sampling volumes and locations. As was shown in Ma [133] et al, the texture in additive manufactured specimens changes significantly across the built. In fact, this is a specific field where the transmission measurements can make a difference, as the usual diffraction measurements lack the spatial resolution to allow a pertinent assessment of local texture.

5.6 Summary

The neutron transmission through a textured specimen was calculated using a single crystal to polycrystal approach. This approach allows for the determination of a threshold number of grains necessary for texture simulation in neutron transmission. Furthermore the simulation is based on a single crystal population generated around an ideal texture component described with the Miller indices. Neutron transmission as a function of rotation for a textured bulk sample is simulated to study the intensity change at Bragg-edge locations as well as between them. Additionally, ODFs derived from measured pole figures can be used to calculate the effect of texture on neutron transmission spectra. Neutron transmission for deformation texture and recrystallization texture were simulated for an aluminum sample to demonstrate that

the neutron transmission technique may be an effective tool to characterize texture evolution during recrystallization. Our approach allows also to estimate the number of grains contributing to Bragg-edges in both untextured and textured polycrystals. Simulations of the cube texture component in the Ni super alloy Inconel 718 were compared to the transmission measurements performed at ORNL. The simulated and measured data are in reasonable agreement, but more efforts are needed to assess the accuracy of both grains statistics and instrumental errors.

Chapter 6

Extending Sinpol for Strain Simulation

This chapter deals with the simulation of strain, and the theoretical concepts described in previous chapters are used here to extend *Sinpol* for neutron transmission strain simulation. To speed the development of advanced manufacturing methods for metal components, there is a need to measure intrinsic strain within components. Spectral neutron transmission measurements have the potential to provide three-dimensional strain tensor measurements in polycrystalline materials due to shifting of diffraction peaks and/or Bragg-edges. A number of previous efforts have sought to develop reconstructions for this measurement by fitting Bragg-edges in each pixel of the transmission image [23, 134, 135, 136]. In these works, the strain is simulated by uniformly varying the lattice distance, d_{hkl} , but here the simulation engine I have developed is different from the cited work such that the simulation of neutron transmission through polycrystalline materials is calculated from a distribution of single crystals with the strain applied to each crystal individually. This approach allows the user to define a crystal orientation and strain distribution within the sample. As a result, the tool is capable of investigating transmission through crystalline materials with variations in texture, grain size, mosaic, and type. In this

chapter the simulation tool *Sinpol* has been modified to simulate the effect of strain to Bragg-edge neutron transmission. Considering that the transmission of each grain is calculated within *Sinpol*, the ability to simulate strain is demonstrated using two different methods and those two methods are the first two sections of this chapter. The first section presents the strain starting from a macro-strain. Strain calculations and simulations for single crystal are presented, followed by strain calculation and simulation for polycrystalline Inconel-718. Simulations showing the rotation of a strained sample are shown for the purpose of computed tomography. The second section presents the simulation from a macro-stress in the limit of elastic theory for the single case. For polycrystalline materials, the strain is simulated in both Voigt and Reuss hypothesis and combined to approach the Hill approximation. The final section of the chapter presents a phenomenological model based on strain diffraction data in which both elasticity and plasticity is considered, and corresponding neutron transmission patterns are simulated.

6.1 Macro-Strain to Lattice Strain

In Figure 6.1 the orthogonal coordinate systems used to derive equations are shown. The axes Y_i^S are for the surface of the sample with Y_1^S and Y_2^S on the surface. Y_i^L define the laboratory system where Y_3^L is in the direction of the neutron beam. When a single crystal is in back reflection or when polycrystalline Bragg-edges are observed Y_3^L is in the direction of the normal to the planes (hkl) whose inter-planar spacing d will be measured. Y_1^L makes an angle ϕ with Y_1^S and ρ is the vertical angle describe in chapter 3, it is the angle between Y_3^L and Y_3^S . When the inter-planar lattice spacing d is obtained from the diffraction peak for a given reflection hkl , the strain component along Y_3^L can be obtained using the formula

$$\epsilon(\phi, \rho) = \frac{d_{\phi\rho} - d_o}{d_o} \quad (6.1)$$

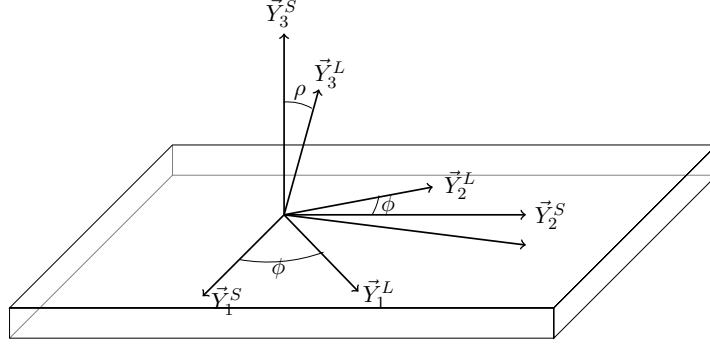


Figure 6.1: Coordinate system used to calculate strain in *Sinpol*

where d_o and $d_{\phi\rho}$ are the strain free lattice, and strained lattice spacing of the hkl plane of interest.

6.1.1 Single Crystal Macro-Strain to Lattice Strain Transformation

For some macro-strain $\bar{\epsilon}_j$ components in the sample system (defined in a six dimension space) the transformation into the crystal's coordinate system gives the micro-strain components [93]:

$$\epsilon_i = \sum_{j=1}^6 Q_{ij} \bar{\epsilon}_j \quad (6.2)$$

where Q_{ij} is a dimensionless (6, 6) matrix fabricated with the elements of the rotation matrix \mathbf{a} and is expressed as:

$$Q_{ij} = \begin{pmatrix} a_{11}^2 & a_{12}^2 & a_{13}^2 & 2a_{12}a_{13} & 2a_{11}a_{13} & 2a_{11}a_{12} \\ a_{21}^2 & a_{22}^2 & a_{23}^2 & 2a_{22}a_{23} & 2a_{21}a_{23} & 2a_{21}a_{22} \\ a_{31}^2 & a_{32}^2 & a_{33}^2 & 2a_{32}a_{33} & 2a_{31}a_{33} & 2a_{31}a_{32} \\ a_{21}a_{31} & a_{22}a_{32} & a_{33}a_{23} & a_{22}a_{33} + a_{23}a_{32} & a_{33}a_{21} + a_{31}a_{23} & a_{22}a_{31} + a_{21}a_{32} \\ a_{11}a_{31} & a_{12}a_{32} & a_{13}a_{33} & a_{33}a_{12} + a_{32}a_{13} & a_{11}a_{33} + a_{13}a_{31} & a_{11}a_{32} + a_{12}a_{31} \\ a_{11}a_{21} & a_{12}a_{22} & a_{13}a_{23} & a_{22}a_{13} + a_{23}a_{12} & a_{11}a_{23} + a_{13}a_{21} & a_{11}a_{22} + a_{12}a_{21} \end{pmatrix} \quad (6.3)$$

In the case of single crystal, \mathbf{a} is the product of the three Euler angles that aligned the crystal into the sample coordinate system, and thus the micro-strain can be calculated exact for a known macro-strain. Hence the micro-strain components are projected into lattice strain with the following relationship [93]:

$$\langle \epsilon_{hh} \rangle = \sum_{i=1}^6 E_i \varrho_i \epsilon_i \quad (6.4)$$

where E_i are the direction cosines and ϱ_i are defined as $(\varrho_1, \dots, \varrho_6) = (1, 1, 1, 2, 2, 2)$, the lattice strain for a single crystal can be written as a function of macro-strain:

$$\langle \epsilon_{hh} \rangle = \sum_{i=1}^6 \sum_{j=1}^6 E_i \varrho_i Q_{ij} \bar{\epsilon}_j \quad (6.5)$$

6.1.2 Single Crystal Macro-Strain to Lattice Strain Simulation Results

Cross section through a polycrystalline material is a sum of the cross section for each individual grain along the transmission path. As such, *Sinpol* calculates transmission through each grain in the distribution. In this section, strain simulation results are first presented for single crystal samples and then followed by polycrystalline sample calculations and results.

Figure 6.2 shows a simulation result for a single crystal Inconel-718 represented as relative intensity (1-Transmission) versus wavelength. The peaks are a result of diffraction from the various lattice planes present in the crystal. In this simulation, the crystal is cut along the [110] similar to the copper crystal in chapter 4, the cross section parameters for simulations are found in Table 1 in chapter 5. The [220] lattice is aligned with the direction of the neutron beam, so that this peak is positioned at 2.5455 angstroms which can be directly calculated from Bragg's law. As expected, the [220] peak is narrow in comparison to peaks at other wavelengths as it is close

to back-reflection position. Lattice planes associated with the other peaks are not aligned with the neutron beam and broaden due to the crystal mosaic structure. By taking the derivative of Bragg's law with respect to θ , change in wavelength versus change in angle goes with the cosine of the angle.

Next, the impact of strain on neutron transmission for the Inconel-718 single crystal is considered. Equation 6.6 is the calculation of the lattice strain for this crystal orientation in the neutron beam. It is calculated by inserting the Euler angles that are used to align the crystal to the neutron beam into equation 6.5, the lattice strain is then calculated as a function of the 6 components that represent the strain tensor in the material. The diffraction peak location is impacted by both Bragg angle, θ_B , and the lattice spacing, d_{hkl} . Therefore, changes in lattice spacing with strain will directly impact peak position.

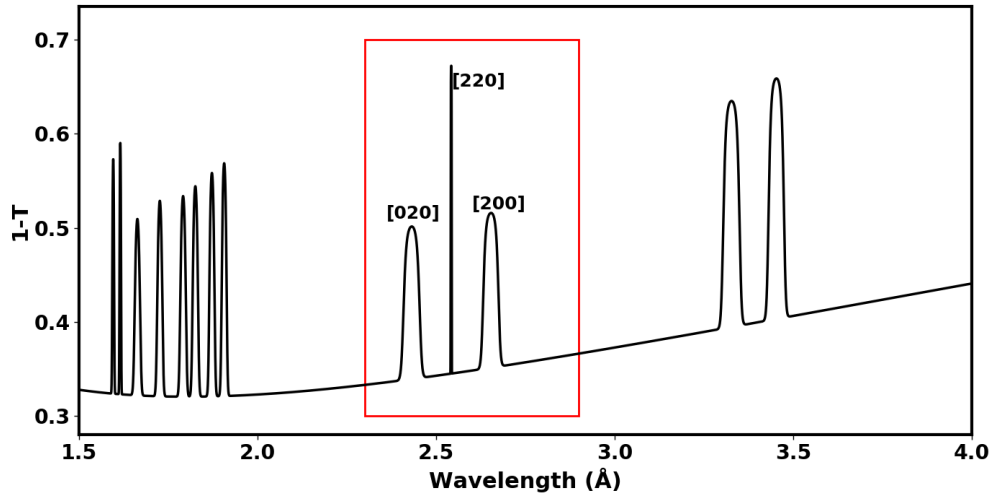


Figure 6.2: Simulation of neutron transmission spectra of single crystal Inconel 718.

$$\begin{aligned}
\langle \epsilon_{hh} \rangle = \frac{1}{h^2 + k^2 + l^2} & \left(\epsilon_1 (.543h^2 + .4567k^2 - .996hk) + \right. \\
& \epsilon_2 (3.038e^{-4}h^2 + 3.615e^{-4}k^2 + .999l^2 - 0.0380kl - 0.0348hl + 6.628e^{-4}hk) + \\
& \epsilon_3 (.456h^2 + .543k^2 + 6.65e^{-4}l^2 + 0.0380kl + 0.0348hl + .996hk) + \\
& \epsilon_4 (0.0235h^2 + 0.0280k^2 - 0.052l^2 - 1.47kl - 1.35hl + 0.0514hk) + \\
& \epsilon_5 (.996h^2 - .996k^2 - 0.035kl + 0.0380hl + .173hk) + \\
& \left. \epsilon_6 (0.026h^2 - 0.026k^2 + 1.35kl - 1.47hl + 0.0045hk) \right). \tag{6.6}
\end{aligned}$$

Figures 6.3-6.7 show simulation results for four different linear strain conditions over a smaller wavelength band around the three peaks highlighted in Figure 6.2. Each graph within the figures shows relative intensity(1-T) versus wavelengths for the no-strain case in black line, compressive strain in red line, and tensile strain in green line. Strain is a deformation of the material that is represented by a 6 value tensor $[\bar{\epsilon}_x, \bar{\epsilon}_y, \bar{\epsilon}_z, \bar{\epsilon}_{xy}, \bar{\epsilon}_{xz}, \bar{\epsilon}_{yz}]$, where $\bar{\epsilon}_x$, $\bar{\epsilon}_y$, and $\bar{\epsilon}_z$ represent the deformation in the $x(Y_1^S)$, $y(Y_2^S)$, and $z(Y_3^S)$ directions of the sample. The remaining components are shear components in the xy, xz, and yz planes. Figure 6.3 show the simulation results for linear strains in the x direction, compressive and tensile strains of $3000\mu\epsilon$ were simulated. In this set up, the neutron beam is along the z-direction and perpendicular to the strain direction. The lattice strain is calculated using equation 6.6, and diffraction peaks are shifted correspondingly. Inserting the hkl plane value of interest, the [220] plane is shifted by 0.00188 of the macro-strain, the [200] plane is shifted by 0.5433 of the macro-strain, and the [020] plane is shifted by 0.4567 of the inputted value. The simulated shifts are equal to the expected wavelength shift calculated from the Bragg equation. Similarly Figures 6.4 and 6.5 present the simulation results for macro-strains applied in the y and z direction respectively. When the strain is along the y-direction, it is perpendicular to the neutron beam along the vertical direction. The [220] plane is shifted by 0.000664 of the inputted strain value, the [020] is shifted

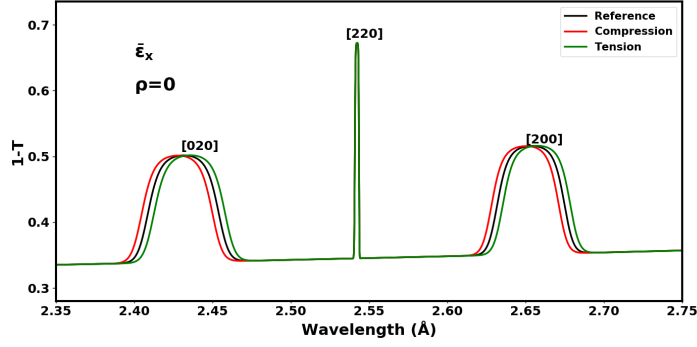


Figure 6.3: Simulation results for single crystal Inconel 718 subject to uni-axial strains along the x direction.

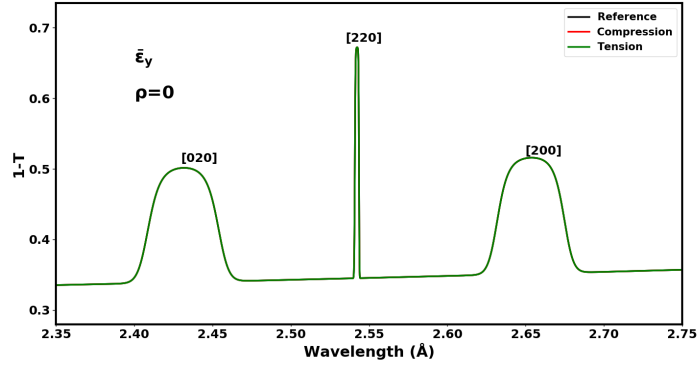


Figure 6.4: Simulation results for single crystal Inconel 718 subject to uni-axial strains applied along the y direction.

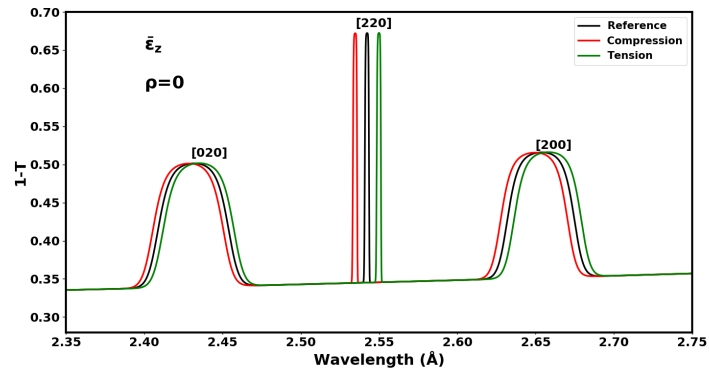


Figure 6.5: Simulation results for single crystal Inconel 718 subject to uni-axial strains applied along the z direction.

by .00036 of the inputed strain value and [200] is shifted by 0.00030 of the macro-strain value. In this case as well as when the strain is applied along the x-direction, the [220] plane's shift is not zero because the crystal is not perfectly aligned with the $\langle 220 \rangle$ along the z direction. The shift in both cases would not be detected by current detector systems. When the strain is in the z-direction, it is aligned with neutron beam. The [220] line which is close to its Bragg-edge condition is shifted by 0.997 of the macro-strain. The [020] plane and [200] plane are shifted with values similar to the case when the strain is applied along the x-direction. Figure 6.6 is an example of applying bi-axial strain on the crystal, the simulated strains are $3000 \mu\epsilon$ along the x-direction and $1000 \mu\epsilon$ along the z-direction. For completion, Figure 6.7 is the case of hydrostatic strain in which the three principal strains have values of $3000 \mu\epsilon$. The contribution of the strain in the z-direction dominates the displacement of the [220] plane as the strain in y-direction and x-direction do not contribute.

Figures 6.8 and 6.9 show the simulations of the macro-strain along the x-direction and z-direction, but in these cases the crystal has been rotated by 90 degrees around the y axis such that the x component of strain is aligned with the neutron beam and the z component of the strain is perpendicular to the neutron beam. The strain

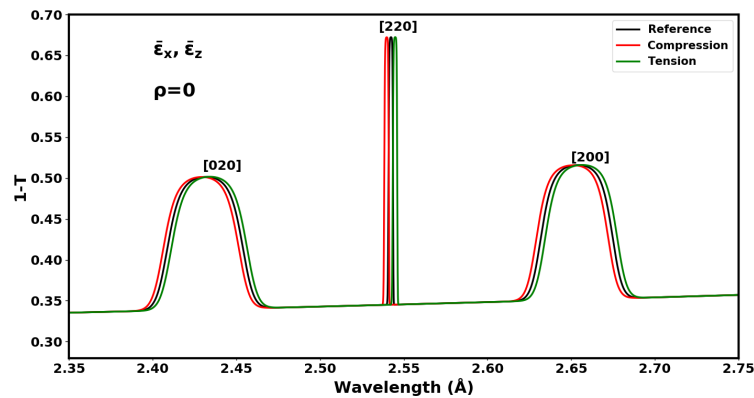


Figure 6.6: Simulation results for single crystal Inconel 718 subject to bi-axial strains applied along the x and z direction.

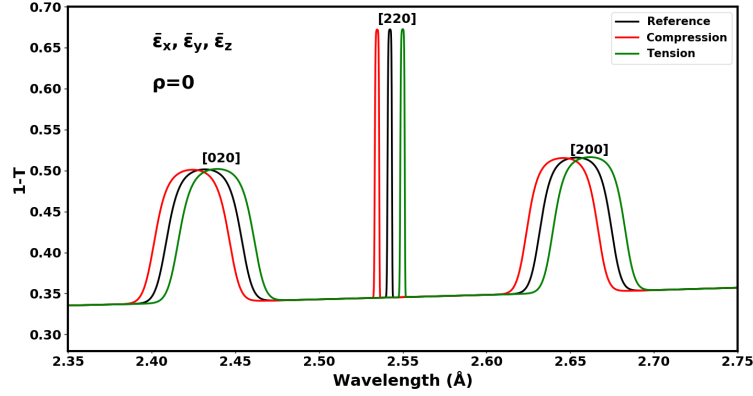


Figure 6.7: Simulation results for single crystal Inconel 718 subject to hydrostatic strains.

value remains the same as the displacement is now observed in different planes. With rotation, the [220] and [200] planes are no longer observable in the wavelength band of interest. When the strain is now aligned in the x-direction, the peak displacement is now observed in the [-220] plane which is in Bragg-edge condition, [020] and [-200] planes. When the strain is in the z-direction, the strain is orthogonal to the neutron beam and no shift is observed.

6.1.3 Polycrystal Macro-Strain to Lattice Strain

For a single crystal, the macro-strain is transformed to the crystal frame using the rotation matrix \mathbf{a} as a function of three Euler angles that aligned the crystal in the neutron beam. In the case for polycrystals, the rotation matrix \mathbf{a} which links the sample coordinate system to the crystal coordinate system is expressed as a function of the lattice planes (hkl) , the two angles that describe the measurement direction in the laboratory frame (ϕ, ρ) and the angle around the normal of the lattice plane, ω . For cubic systems, the corresponding rotation matrix can be written as the product of the three matrices and is written as

$$\mathbf{a} = g'(\vec{h}_1, \vec{h}_2, \vec{h}_3) f(\phi, \rho) g(\omega) \quad (6.7)$$

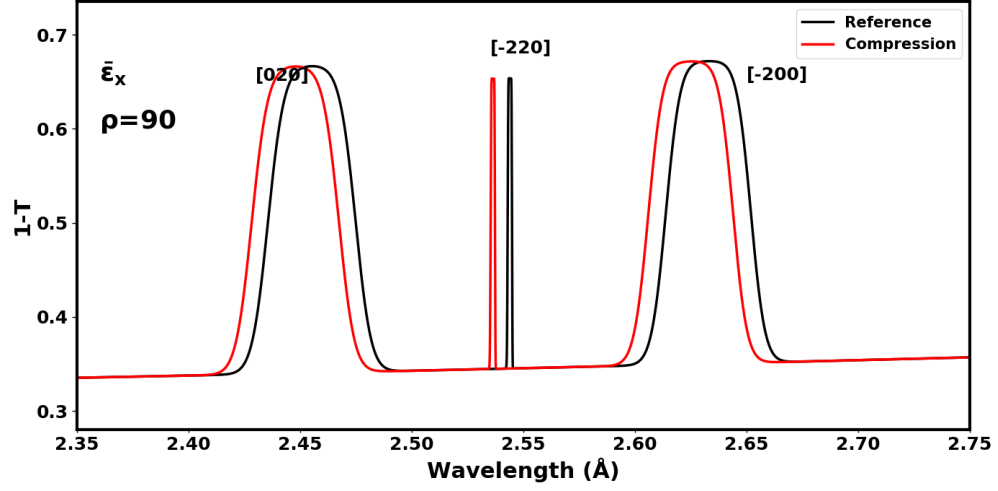


Figure 6.8: Simulation results for single crystal Inconel 718 subject to uni-axial strains applied along the X direction.

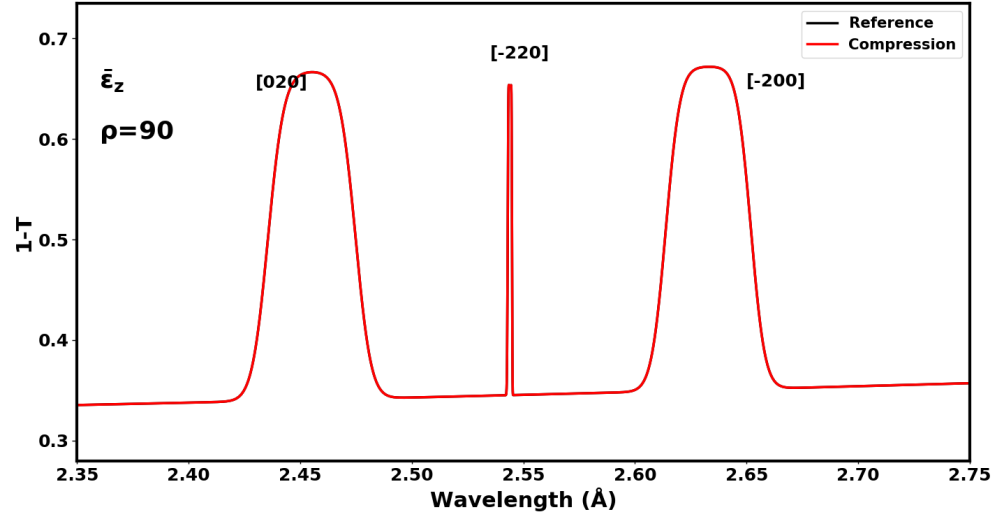


Figure 6.9: Simulation results for single crystal Inconel 718 subject to uni-axial strains applied along the Z direction.

where

$$g(\omega) = \begin{pmatrix} \cos \omega & \sin \omega & 0 \\ -\sin \omega & \cos \omega & 0 \\ 0 & 0 & 1 \end{pmatrix} \quad (6.8)$$

and

$$f(\phi, \rho) = \begin{pmatrix} \cos \rho & 0 & -\sin \rho \\ -\sin \phi \sin \rho & \cos \phi & -\sin \phi \cos \rho \\ \cos \phi \sin \rho & \sin \phi & \cos \phi \cos \rho \end{pmatrix} \quad (6.9)$$

finally

$$g'(\vec{h}_1, \vec{h}_2, \vec{h}_3) = \begin{pmatrix} h_1 & h_2 & h_3 \\ k_1 & k_2 & k_3 \\ l_1 & l_2 & l_3 \end{pmatrix} \quad (6.10)$$

where $g'(\vec{h}_1, \vec{h}_2, \vec{h}_3)$ denotes three perpendicular vectors and their h, k, l components are normalized. Following the scheme from the single crystal, the macro-strain is transformed to micro-strain and projected to each lattice using equation 6.2, the elements from the rotation matrix in equation 6.7 and the equation 6.4. The strain value measured in neutron diffraction experiment on a polycrystal is the average of the strain along the reciprocal lattice vectors. The lattice strain is the average of equation 6.5 over all grains having their reciprocal lattice vector parallel to the scattering vector and be written as

$$\langle \epsilon_{hh} \rangle = \sum_{i=1}^6 \sum_{j=1}^6 E_i Q_i \bar{\epsilon}_j \int_0^{2\pi} \frac{Q_{ij}(\vec{h}_1, \vec{h}_2, \vec{h}_3, \phi, \rho, \omega) d\omega}{2\pi} \quad (6.11)$$

by integrating over ω equation 6.11 reduces to

$$\langle \epsilon_{hh} \rangle = \sum_{i=1}^6 \sum_{j=1}^6 E_i Q_i \bar{\epsilon}_j Q_{ij}(\vec{h}_1, \vec{h}_2, \vec{h}_3, \phi, \rho) \quad (6.12)$$

inserting the orthogonality condition $h_{ij}h_{ik} = \delta_{jk}$, the dependence on hkl is remove and the lattice strain is expressed as:

$$\begin{aligned} \langle \epsilon_{hh} \rangle = & \sin^2 \rho \cos^2 \phi \epsilon_1 + \sin^2 \phi \epsilon_2 + \cos^2 \rho \cos^2 \phi \epsilon_3 + \\ & \cos \rho \sin 2\phi \epsilon_4 + \sin 2\rho \cos^2 \phi \epsilon_5 + \sin 2\phi \sin \rho \epsilon_6. \end{aligned} \quad (6.13)$$

Since equation 6.13 is independent of h,k,l component of the vector of $g'(\vec{h}_1, \vec{h}_2, \vec{h}_3)$ it holds for lattice strain calculation for textured samples.

Figure 6.10 shows simulation results for four different strain conditions simulated for an Inconel 718 powder, an inset is shown in each figure to zoom in on the displacement of the Bragg-edge for the [111] plane located at 4.1569 angstroms. Each plot within the figure shows relative intensity(1-T) versus wavelengths for no strains in back line and compressive strains in red. The linear strains in the x-direction, y-direction, z-direction and hydrostatic case are simulated. At $\rho = 0$ degrees, equation 6.13 stipulates that the displacement of Bragg-edges when the strain is orthogonal to the neutron beam in the x-direction or y-direction is not observable as shown by the top two plots of Figure 6.10. The bottom two plots of Figure 6.10 show the effect of the strain when it is along the neutron beam (lower left), and when an hydrostatic strain is applied (lower right). In this case the effect of the component of the strain

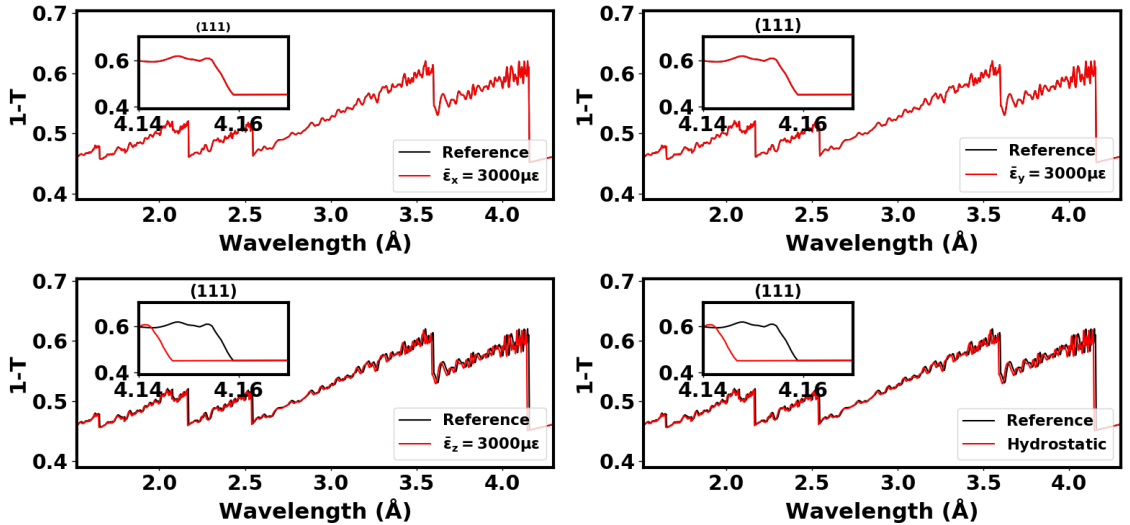


Figure 6.10: Simulation 111 Bragg-edge transmission spectra of powder Inconel 718 for four strain conditions.

along the beam is measured as the two other orthogonal components of the strain do not contribute to the simulation. Similarly Figure 6.11 shows simulation for a cube textured Inconel-718 sample with 3000 $\mu\epsilon$, the same four strain geometries are considered. Again, it is observed that the effect of the strain is not detectable when the strain is along the x-direction, or y-direction. When the strain is along the z direction and parallel to the neutron beam a shift in the Bragg-edge is observed.

Figures 6.12-6.15 present wavelength-dependent results depicting the movement of Bragg-edge locations and intensities as a function of rotation while different strain geometries are applied. This is done for the purpose of understanding Bragg-edge movement induced by strain for computed tomography. The 1-cm thick Inconel-718 sample is rotated 180 degrees around the transverse (vertical) direction and eight different strain geometries are considered. Figure 6.12 shows three simulation results, the left figure is the unstrained Inconel powder, the figure shows the location of the [111] Bragg-edge at 4.1569 angstroms remains unchanged through rotation. The middle figure is the simulation of the [111] Bragg-edge location when an hydrostatic

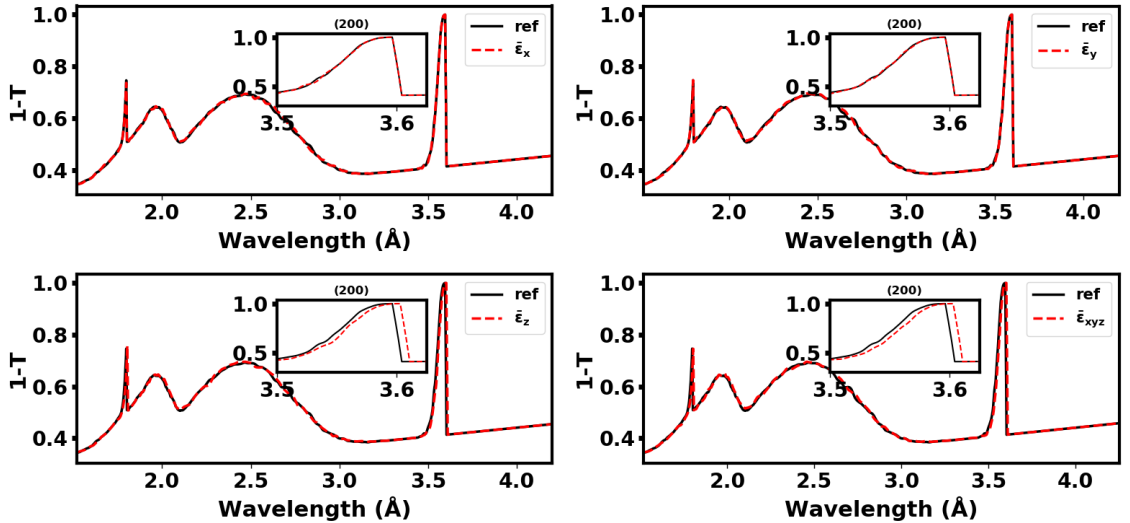


Figure 6.11: Simulation 200 Bragg-edge transmission spectra for cube textured Inconel 718 for four strain conditions.

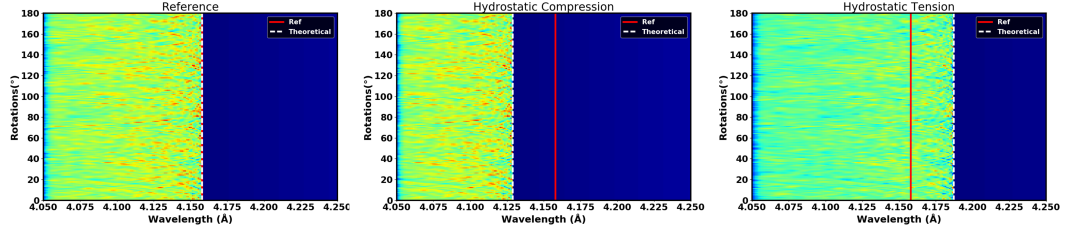


Figure 6.12: Simulation of 111 Bragg-edge under with 7000 $\mu\epsilon$ uniformly applied in compression and tension.

compressive strain of 7000 $\mu\epsilon$ is applied and the sample is rotated 180 degrees around the vertical, the new location due to the change in lattice spacing is 4.1278 angstroms as expected and remains unchanged with rotation. For completion, the same set up is simulated with hydrostatic tension applied to the sample, similarly the new Bragg-edge location(4.185998 angstroms) remains unaffected with rotations.

Figures 6.13 presents simulations of uni-axial strain along the Y_1^S axis or x axis under rotations. At rotation angle of $\rho = 0$ degrees the strain is orthogonal to the neutron beam. The effect of the strain on the Bragg-edge is negligible as the strain field is not along the neutron beam. As the sample is rotated the Bragg-edge is displaced until it reaches maximum displacement at $\rho = 90$ degrees (4.1278 angstroms for compression, 4.185998 for tension), at this angle the strain in the sample is now along the neutron beam and maximum effect of the strain is experienced by the Bragg-edge. Figures 6.14 present simulations of uni-axial strain along the Y_3^S axis or z axis as the sample is rotated. At rotation angle of $\rho = 0$ degrees the strain is along the neutron beam. The Bragg-edge experiences maximum displacement, and as the sample is rotated the Bragg-edge returns to its unstrained location at $\rho = 90$ degrees. Figures 6.15 present simulations of bi-axial strain along the Y_3^S and Y_3^S axes the sample is rotated. In this arrangement, at rotation angle of $\rho = 0$ degrees the Bragg-edge is displaced by the contribution of the strain from the Y_3^S axis. At rotation angle of $\rho = 90$ degrees the Bragg-edge is displaced by the contribution of

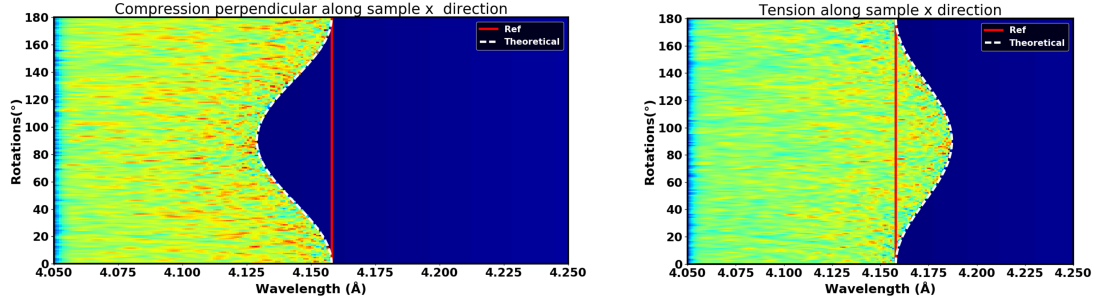


Figure 6.13: Simulation of 111 Bragg-edge under with $7000 \mu\epsilon$ along the Y_1^S axis. At rotation angle of $\rho = 0$ degrees the strain is orthogonal to the neutron beam in compression and tension.

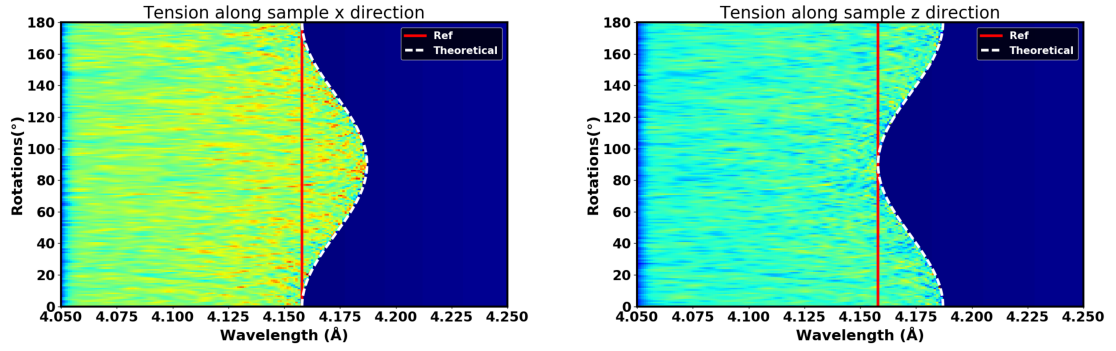


Figure 6.14: Simulation of 111 Bragg-edge under with $7000 \mu\epsilon$ along the Y_3^S axis. At rotation angle of $\rho = 0$ degrees the strain is parallel to the neutron beam in compression and tension.

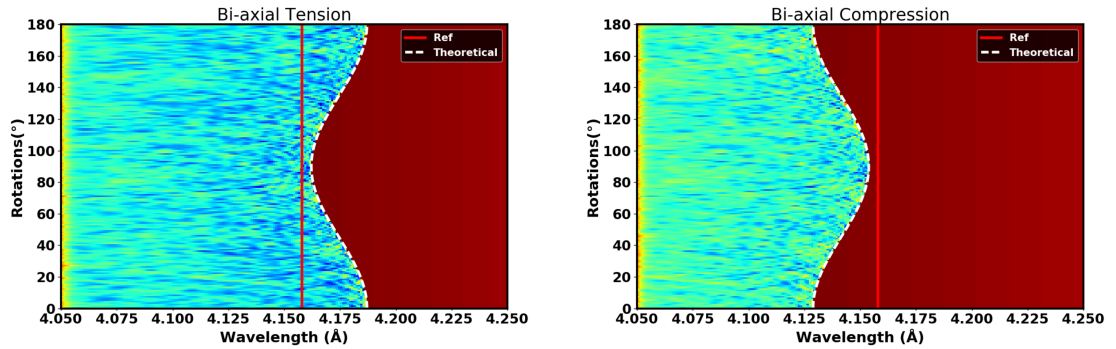


Figure 6.15: of 111 Bragg-edge under with $7000 \mu\epsilon$ along the Y_3^S axis and $1000 \mu\epsilon$ along the Y_1^S axis.

strain from the Y_1^S axis. Effect of the contributions of the strain for both axis can be observed at angles of 45 and 135 degrees.

6.2 Macro-Stress to Lattice Strain

The above sections dealt with the behavior of polycrystal lattice plane in non-texture samples which are usually considered to be isotropic. Polycrystalline materials are composed of single crystal grains whose properties are anisotropic. *Sinpol* calculates the lattice strain for a given macro-stress $\bar{\sigma}_j$ using a similar scheme that is described in the macro-strain to lattice strain section. In most materials, the Young Modulus (E) and the Poisson ratio (ν) are dependent on the direction of lattice planes that are used as strain gauges, since the stress is anisotropic [137]. In order to understand the mechanics of elastic response in polycrystalline aggregates from the perspective of neutron transmission strain measurement, we start with the strain-stress relationship for a single crystal in the limits of elastic theory.

6.2.1 Single Crystal Macro-Stress to Lattice Strain Calculation

A single crystal is an anisotropic system and its most important property is its elastic constant. The elastic constant determines the response of a single crystal for a wide range of concerns including temperature, electric field, magnetic fields, and mechanical disturbances such as stress and strain which is the focus of this section. For a general anisotropic, elastic solid the strain is linearly proportional to the stress σ_{kl} as expressed by Hook's law and is written as

$$\epsilon_{ij} = S_{ijkl}\sigma_{kl} \quad (6.14)$$

in which summation(over 1,2,3) is implied over the repeated subscript k and l . The elastic compliance tensor with elements S_{ijkl} is a fourth rank that obeys the law of

tensor transformation and has a total of 81 terms components. All 81 components are not independent. However, the strain and the stress are both second rank and are both symmetric. Each has six independent components and six equations are necessary to calculate the strain from the stress. In each equation there are six independent terms. Consequently there can be no more than 36 independent terms in S_{ijkl} . It is standard practice in elasticity to use an abbreviated Voigt [55] notation for strains, stresses and stiffness and compliance. In this abbreviated notation the strains and stresses are expressed as a six-column vectors rather than as nine-element square matrices:

$$\sigma = \begin{bmatrix} \sigma_1 = \sigma_{11} \\ \sigma_2 = \sigma_{22} \\ \sigma_3 = \sigma_{33} \\ \sigma_4 = \sigma_{23} \\ \sigma_5 = \sigma_{13} \\ \sigma_6 = \sigma_{12} \end{bmatrix} \quad \epsilon = \begin{bmatrix} \epsilon_1 = \epsilon_{11} \\ \epsilon_2 = \epsilon_{22} \\ \epsilon_3 = \epsilon_{33} \\ \epsilon_4 = 2\epsilon_{23} \\ \epsilon_5 = 2\epsilon_{13} \\ \epsilon_6 = 2\epsilon_{12} \end{bmatrix} \quad (6.15)$$

Note the definition of the stress and strain differs by a factor of 2. In the Voigt notation, the four subscripts of the compliance and stiffness tensor are reduced to two subscripts using the convention introduced by Wooster [138] and is reduced as follows: $11 \rightarrow 1, 22 \rightarrow 2, 33 \rightarrow 3, 23 = 32 \rightarrow 4, 13 = 31 \rightarrow 5$ and $12 = 21 \rightarrow 6$. Using the reduced notation Hook's law can be written as

$$\begin{bmatrix} \epsilon_1 \\ \epsilon_2 \\ \epsilon_3 \\ \epsilon_4 \\ \epsilon_5 \\ \epsilon_6 \end{bmatrix} = \begin{bmatrix} S_{11} & S_{12} & S_{13} & S_{14} & S_{15} & S_{16} \\ S_{21} & S_{22} & S_{23} & S_{24} & S_{25} & S_{26} \\ S_{31} & S_{32} & S_{33} & S_{34} & S_{35} & S_{36} \\ S_{41} & S_{42} & S_{43} & S_{44} & S_{45} & S_{46} \\ S_{51} & S_{52} & S_{53} & S_{54} & S_{55} & S_{56} \\ S_{61} & S_{62} & S_{63} & S_{64} & S_{65} & S_{66} \end{bmatrix} \begin{bmatrix} \sigma_1 \\ \sigma_2 \\ \sigma_3 \\ \sigma_4 \\ \sigma_5 \\ \sigma_6 \end{bmatrix} \quad (6.16)$$

The strain and compliance matrices in the Voigt notations are not tensors. The Voigt [55] [139] notation although the most commonly used to define the strain stress relation has several mathematical disadvantages. For example, certain norms of the fourth-rank stiffness tensor are not equal to the corresponding norms of the Voigt stiffness matrix [140] [141], and the eigenvalues of the Voigt stiffness matrix are not the eigenvalues of the stress tensor. There are two other abbreviated notation that can be used to define the strain stress relation. In the Kelvin [142] [143] notation, each element of the compliance matrix is weighted according to how many elements of the actual compliance tensor are present. Each element with indices 4,5,6 receives a weight $\sqrt{2}$. In the Wooster [138] [93] notation that is used in this section, each element with indices 4,5,6 receives a weight of 2.

For the cubic materials simulated in this work the compliance matrix as the following form:

$$\begin{bmatrix} S_{11} & S_{12} & S_{12} & 0 & 0 & 0 \\ S_{12} & S_{11} & S_{12} & 0 & 0 & 0 \\ S_{12} & S_{12} & S_{11} & 0 & 0 & 0 \\ 0 & 0 & 0 & S_{44} & 0 & 0 \\ 0 & 0 & 0 & 0 & S_{44} & 0 \\ 0 & 0 & 0 & 0 & 0 & S_{44} \end{bmatrix} \quad (6.17)$$

where S_{11} , S_{12} , and S_{44} are written in terms of the stiffness:

$$\begin{aligned} S_{11} &= \frac{C_{11} - C_{12}}{(C_{11} - C_{12})(C_{11} + 2C_{12})} \\ S_{12} &= \frac{-C_{12}}{(C_{11} - C_{12})(C_{11} + 2C_{12})} \\ S_{44} &= \frac{1}{4C_{44}}. \end{aligned} \quad (6.18)$$

Sinpol calculates the lattice strain from a given macro-stress by calculating the strain from both the Voigt assumption (constant strain) and the Reuss assumption (constant stress). The macro-stress $\bar{\sigma}_j$ is transformed into micro-stresses per grain using Popa's equation and is given as

$$\sigma_i = \sum_{j=1}^6 Q_{ij} \bar{\sigma}_j \quad (6.19)$$

where Q_{ij} is the aforementioned transformation matrix whose elements are dependent of the rotation matrix \mathbf{a} . The 6 strain components for each grain are then calculated using Hook's law

$$\epsilon_i = \sum_{j=1}^6 S_{ij} \sigma_j \quad (6.20)$$

the micro-strain are then projected into the crystal coordinate system and the average lattice strain for a single crystal is calculated with equation 6.4.

6.2.2 Single Crystal Macro-Stress to Lattice Strain Simulation Results

The simulation of the effect of the lattice strain from macro-stress on neutron transmission for the Inconel-718 single crystal is presented. Figure 6.16 shows simulation results for 1-T on the four different planes near their respective Bragg deep locations. This was done to illustrate the anisotropic lattice strain response to the same stress. Table 6.1 presents theoretical wavelength positions and simulated wavelength positions for the plane of interest([111], [200], [220], and [311]) strained

Table 6.1: Comparison between theoretical wavelength position and simulated wavelength position for 4 peaks with 1000 Mpa applied stress

	$\langle \epsilon_{hh} \rangle^{theo} (\mu\epsilon)$	$\langle \epsilon_{hh} \rangle^{Sinpol} (\mu\epsilon)$	$\lambda_{nostress}^{theo} (\text{\AA})$	$\lambda_{nostress}^{Sinpol} (\text{\AA})$	$\lambda_{stress}^{theo} (\text{\AA})$	$\lambda_{stress}^{Sinpol} (\text{\AA})$
[311]	0.00575	0.00484	2.17088	2.1707	2.1834	2.1812
[220]	0.00463	0.00420	2.54558	2.5453	2.5574	2.5560
[200]	0.00763	0.00681	3.6	3.6	3.6275	3.6245
[111]	0.00363	0.00339	4.15692	4.15691	4.1720	4.1710

and unstrained. The peak positions were simulated by aligning the ideal orientations along the beam; the respected Euler angles are (0,55,45) for [111], (0, 0, 0) for [002], (0, 90, 45) for [220], and (0, 23.9, 45) for [311]. Peak positions for strain measurements were obtained by taking the derivatives of each peak and the maxima is used as the peak location. The strain is simulated by applying 1000 Mpa along the neutron beam direction (σ_3); the stiffness values of $C_{11} = 199$, $C_{12} = 101$ and $C_{44} = 120$ for Inconel are used to calculate the compliance values for the simulation. Table 6.1 show the comparison of the theoretical wavelengths and simulated wavelength for both reference and displaced wavelengths. The difference between simulated strains and theoretical strains varies from a minimum of 5% for [111] to 16% for [311]. The difference between simulated strain and theoretical strain are due to the misalignment in crystal simulation and peak positions determined by the maxima from taking the derivatives of the peaks.

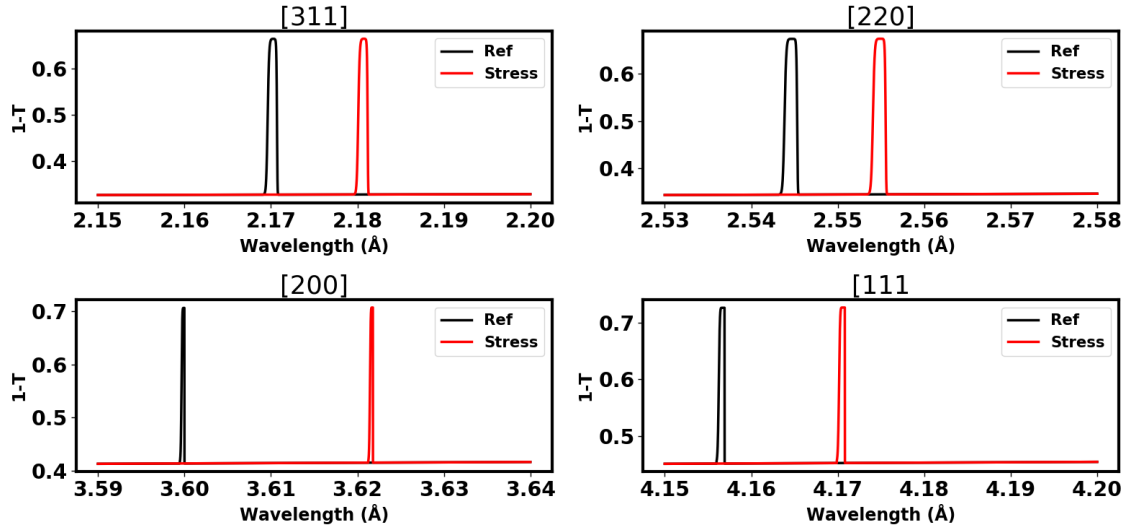


Figure 6.16: Simulation of neutron transmission of single crystal Inconel 718 peaks with 1000 Mpa stress applied along the beam direction.

6.2.3 Polycrystal Macro-Stress to Lattice Strain

Polycrystalline samples are made of single crystal aggregate whose properties are anisotropic. The elastic constants polycrystalline sample are influenced by the interaction between individual grains which is not considered in this thesis, and by the single crystal elastic constants of crystalline grains. Historically, several models have been proposed such as Voigt [55], Reuss [56] and Hill [144].

For a single crystal, the macro-stress is transformed to the crystal frame using the rotation matrix as a function of three Euler angles that aligned the crystal in the neutron beam. In the case for polycrystals, the rotation matrix \mathbf{a} which links the sample coordinate system to the crystal coordinate system is expressed by the scheme described in section 6.2.1. Following the single crystal scheme, the macro-stress is transformed to micro-stress and the micro-strains are calculated with equation 6.14 and specific lattice strains results by using equation 6.4. This is still a single crystal lattice results, which can be extended over entire polycrystal aggregate by considering the Reuss assumption: all grains experience the same macro-stress. In that case, calculating the measured lattice strain value will require averaging over ω . Because of the anisotropic behavior of the stress, dependency on the hkl indexes is not removed by averaging over ω . A general formula for the lattice strain that considers the anisotropy is achieved by spectral decomposition of the compliance matrix, the \mathbf{Q} matrix and averaging over ω . The average lattice can be written as a scalar product of two vectors and is given as:

$$\langle \epsilon_{hh} \rangle = \left((S_{12} + 2(A - 1)S_{44}\Gamma_{hkl})[1, 1, 1, 0, 0, 0] + \right. \\ \left. (S_{11} - S_{12} - 6(A - 1)S_{44}\Gamma_{hkl})[B_1^2, B_2^2, B_3^2, 2B_2B_3, 2B_1B_3, 2B_1B_2] \right) \sigma_j \quad (6.21)$$

where B_i (i goes from 1 to 3) are the cosine directions in the sample coordinate system and can be represented with the elements of the product of the matrix given by equation 6.9. Γ_{hkl} is the anisotropy factor which shows the orientation dependency of the elastic anisotropy with hkl direction and is given as:

$$\Gamma_{hkl} = \frac{h^2k^2 + k^2l^2 + h^2kl^2}{(h^2 + k^2 + l^2)^2} \quad (6.22)$$

This quantity varies from 0 for a crystal in the [100] direction to $\frac{1}{3}$ for a crystal in the [111] direction. The parameter A governs the amount of anisotropy and is given by:

$$A = \frac{S_{11} - S_{12}}{2S_{44}}. \quad (6.23)$$

When A is equals to 1 the relationship between macro-strain and stress is invariant to the measurement direction in the crystal reference (any hkl direction gives the same result). In another approach, all grains in the distribution experience the same strain which is the Voigt assumption [55] and the average lattice strain is written as

$$\langle \epsilon_{hh} \rangle^V = \left([(S_{12}^V)[1, 1, 1, 0, 0, 0] + (S_{11}^V - S_{12}^V)][B_1^2, B_2^2, B_3^2, 2B_2B_3, 2B_1B_3, 2B_{12}B_2] \right) \sigma_j \quad (6.24)$$

where S_{11}^V , S_{12}^V , and S_{44}^V are the polycrystal compliances obtained by taking the average of single crystal compliance at macroscopic level. The average compliances for a random orientation distribution are given by Popa [93]:

$$\begin{aligned} C_{11}^V &= \frac{3 * C_{11} + 2 * C_{12} + 4 * C_{44}}{5} \\ C_{12}^V &= \frac{C_{11} - 2 * C_{44} + 4 * C_{12}}{5} \\ C_{44}^V &= \frac{C_{11}^V - C_{12}^V}{2}. \end{aligned} \quad (6.25)$$

Using the above definition, the average compliances S_{11}^V , S_{12}^V , and S_{12}^V are calculated as:

$$\begin{aligned} S_{11}^V &= \frac{C_{11}^V - C_{12}^V}{(C_{11}^V - C_{12}^V)(C_{11}^V + 2C_{12}^V)} \\ S_{12}^V &= \frac{-C_{12}^V}{(C_{11}^V - C_{12}^V)(C_{11}^V + 2C_{12}^V)} \\ S_{44}^V &= \frac{1}{4C_{44}^V}. \end{aligned} \tag{6.26}$$

In *Sinpol* the neutron beam is aligned with the third component of the sample in the laboratory frame, thus $B_1 = \cos \phi \sin \rho$, $B_2 = \sin \phi$, and $B_3 = \cos \phi \cos \rho$. Inserting the definition of the B_i , equations 6.26 into equation 6.24 the previous definition of the average lattice strain in equation 6.13 is recovered.

When A is not equal to one, the average lattice strain is calculated based on the Reuss approximation which is equation 6.21. In this approximation, the stress in the sample is considered uniform across all the grains, and the strain in each grain is proportional to the anisotropic coefficient in that grain's direction. Therefore, the elastic constant depends on the crystallographic direction. For polycrystalline with random grain distribution the lattice strain is calculated with equation 6.21. Average lattice strains calculated with Reuss and Voigt approximations represent the lower and higher boundaries of the strain respectively. The strain in the sample lays somewhere in between the two boundaries, Hill [145] proposed the numerical average of the moduli predicted by the two models would provide a satisfactory strain value in most cases and thus *Sinpol* calculates the Hill lattice strain by taking the average of the lattice strains calculated by the Reuss and Voigt models

$$\langle \epsilon_{hh} \rangle^H = \frac{\langle \epsilon_{hh} \rangle^V + \langle \epsilon_{hh} \rangle^R}{2}. \tag{6.27}$$

Figure 6.17 displays neutron transmission simulation results that show the effect of lattice strain from macro-stress on a polycrystalline Inconel-718 sample. The

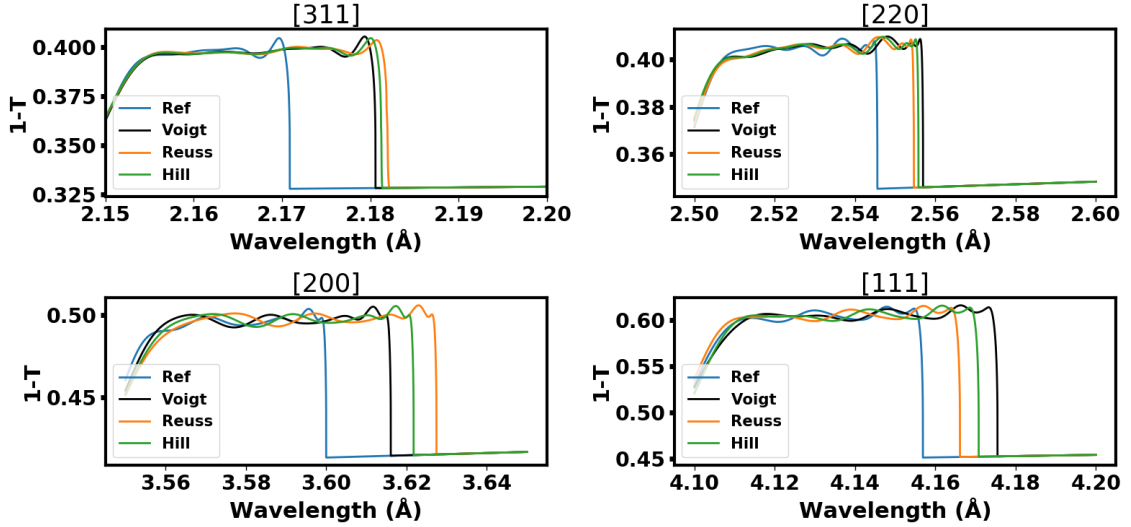


Figure 6.17: Simulation of neutron transmission of powder Inconel 718 Bragg-edges with 1000Mpa stress applied along the beam direction.

anisotropic nature of the stress is demonstrated by studying the first four Bragg-edges in the neutron wavelength spectrum. The single crystal elastic constants for Inconel have been reported in prior paragraphs. The strain is simulated by applying a 1000 Mpa stress along the neutron beam direction. The blue lines are the Bragg-edges simulated with no strain, the black lines are the Bragg-edges with strain calculated with the Voigt approximation, the orange lines are the Bragg-edges with strain calculated with the Reuss approximation and the green lines are the Bragg-edges with strain calculated with the Hill approximation. The average elastic strain calculated in the Voigt approximation affects all the Bragg-edges by displacing them by $4.5 \mu\epsilon/\text{Mpa}$ times the applied stress, in the Reuss approximation the average lattice strain is dependent on the anisotropy coefficient, and the Bragg-edges displaced with the Hill approximation lies between the Reuss and Voigt. In the Reuss approximation the [311] Bragg-edge is displaced by $5.754 \mu\epsilon/\text{Mpa}$ times the stress, [220] Bragg-edge is displaced by $4.63 \mu\epsilon/\text{Mpa}$ times the stress, [200] Bragg-edge is displaced by $7.63 \mu\epsilon/\text{Mpa}$ times the stress and [111] Bragg-edge is displaced by $3.63 \mu\epsilon/\text{Mpa}$ times the stress. Note the [200] Bragg-edge is displaced the most as its anisotropy coefficient

is zero. For the [111], the Reuss strain is closer to the reference case due to the high anisotropy coefficient.

6.3 Phenomenological Model

The intensity of Bragg-edges in neutron transmission are dependent on the crystallographic structure and lattice parameter of the sample. Similar to Bragg peaks measured with neutron diffraction, a Bragg-edge's location is coupled with the lattice spacing of a particular hkl reflection. Investigating the variation of Bragg-edge location, the different lattice spacings could be applied to strain and stress analyses, which is a common method on residual stress and strain diffractometers. This section describes the approach of simulating strain with neutron Bragg-edge transmission based on neutron diffraction strain measurements on a fatigued stainless steel sample. Simulated neutron transmission strain values are compared to strain values obtained from neutron diffraction measurement.

In the Rietveld [6, 62, 23] type neutron transmission softwares, the lattice strain is introduced by reproducing Bragg-edge locations from fitted diffraction lattice strain value. Lattice strains are responsible for changes in the lattice spacing, in these softwares the same strain is considered for all Bragg-edges. The same procedure can be reproduced within *Sinpol*, or the strain lattice can be calculated in the simulation starting from macro-strain or macro-stress as shown in the previous sections. Another possibility is that the orientation dependence of lattice strains in the sample can be expressed in terms of spherical harmonics [146, 147, 148]. In this section the neutron transmission simulation for a stainless steel sample with a strain history of plasticity is considered. The evolution of lattice strain during cyclic loading of LN 316 is discussed in Lorentzen [149] et al and evolution of lattice strains of a stainless steel sample subjected to uni-axial cyclic loading are discussed in the following publications [150, 151, 152]. Normally, a linear relationship between the lattice spacing and

the sine square of the vertical angle (d_{hkl} vs $\sin^2 \rho$) is expected when the macro residual strain is measured with diffraction. For materials that have experienced large deformation the so called non-linear phenomenon, the (d_{hkl} vs $\sin^2 \rho$), relationship oscillates. This behavior can be attributed to two factors, the influence of texture on the diffraction elastic constant [153, 154] and the existence of inter-granular strains which are dependent on the grain orientations [155, 156]. The evolution of lattice strains of a stainless steel sample subjected to large tensile stress is considered. In situ neutron diffraction experiments were carried out in the VULCAN engineering diffractometer at the SNS, full detail of the diffraction experiment on the stainless sample can be found in the following publication [157].

The 316 LN stainless steel sample used in experiment and simulation is composed of 16.31 Cr - 10.2 Ni - 2.07 Mo - 1.75 Mn - 0.23 Cu - 0.16 Co - 0.11 N- 0.039 Si - 0.009 C- 0.002 S(wt%) and the cross sections parameters ($\sigma_{abs} = 0.289$ barns, $\sigma_b = 10.595$ barns, $b_{coh} = 8.227$ fm) necessary for simulation are calculated using equation 5.9. The lattice constant measured during the neutron diffraction experiment is 3.602 angstroms. The stainless steel sample was subjected to tensile stress up 584 Mpa the multiaxial load frame at a constant strain rate of approximately $4 * 10^{-5} s^{-1}$, the tensile stress axis of the load frame was mounted 45 degrees against the neutron beam [157]. The angular dependence of the lattice strain, as well as the hkl dependence, can be described using a simple spherical harmonics approach in this instance can be written as:

$$\tilde{\epsilon}_{hkl}(\rho) = \sum_{i=0}^{\infty} \sum_{j=0}^i B_{ij} k_{2j+2} P_{2i}^0(\rho). \quad (6.28)$$

where the B'_{ij} s are constants that are obtained by fitting the diffraction data and the values used for simulation in this work are given in Table 6.2, k are octahedral harmonics polynomial function of the anisotropy factor Γ_{hkl} and the invariant C_{hkl} defined as $\frac{h^2 k^2 l^2}{(h^2 + k^2 + l^2)^3}$, and P_{2i}^0 are the Legendre polynomials. Equation 6.28 allows for the calculation of deformation induces anisotropic lattice strains for elastic and

Table 6.2: B value obtained from fitting diffraction experiment

B_{ij}	Elastic ($\mu\epsilon$)	Plastic ($\mu\epsilon$)	Max Plastic ($\mu\epsilon$)	Residual ($\mu\epsilon$)
B_{00}	202.436	270.89	566.287	123.135
B_{10}	1156.24	1398.98	2788.85	142.022
B_{11}	-708.8	-910.831	-2374.82	-1206.18
B_{20}	0	0	0	0
B_{21}	21.4128	-136.546	-654.365	-693.699
B_{22}	4.53629	28.7375	132.075	53.4837
B_{30}	0	0	0	0
B_{31}	0	3.802	-57.981	298.9579
B_{32}	0	14.16248	153.088	149.319
B_{33}	0	-48.3447	-755.183	-487.554
B_{40}	0	0	0	0
B_{41}	0	0	0	0
B_{42}	0	13.6932	74.2274	-16.7445
B_{43}	0	49.1064	551.815	369.846
B_{44}	0	0	0	0

plastic strains. The first two terms are enough to represent the lattice strains due to to elasticity, including the effect of inter-granular strains induced by anisotropy in this stage of deformation. In this particular case, the lattice strain always changes the sign from loading direction to transversal direction, as the polynomial P_2 goes from 1 to -0.5.

Figure 6.18 presents simulated lattice strain as a function of the sine square rotation for four different applied stress values(elastic, plastic, max plastic and residual) as the stainless steel is rotated from 0 degrees to 90 degrees. The simulations were performed on a 1-cm thick stainless steel plate segmented one time with 10000 distinct orientations. The lattice strain is introduced by applying equation 6.28 to each lattice plane of each single crystal grain. The ensuring Bragg-edge shifts were determined by taking the derivatives of each Bragg-edge and the maxima was used to calculate the lattice strains. At 0 degrees the loading direction is parallel with the neutron beam, and at 90 degrees the neutron beam is perpendicular to the neutron

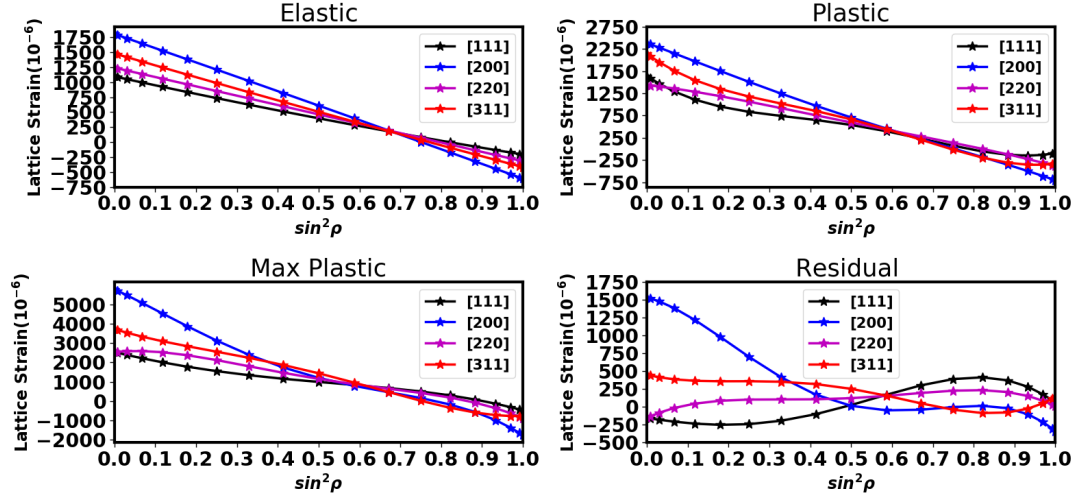


Figure 6.18: Lattice strain distributions in the 316 stainless steel simulated with 111, 200, 220, and 311 as a function of tilt angle relative to the loading with applied stress 264.35 Mpa (Elastic), 315.23 Mpa (Plastic), 584.75 Mpa (Max Plastic), and 21.36 Mpa (residual) direction.

beam. The plot labeled elastic shows the expected linear relationship as the sample is rotated; there is also a direct proportionality between the strain and the stress in the elastic regime. The plastic plot shows the initial departure from the linear relationship, the max plastic plot shows the hardening of the strain in the sample, and the residual plot are the lattice strains after the load is removed. In all four cases, the effect of anisotropy is observed as the lattice strains are different for different hkl . As expected, the displacement of the [200] plane at loading direction ($\rho = 0$ degrees) and transversal direction ($\rho = 90$ degrees) are larger than the displacement of the three other planes presented. Traditionally, the [311] plane lattice strain is used to gauge the error associated with the residual strain in fcc materials in neutron diffraction measurement. In this case, the [220] plane lattice strain may be a possible gauge in transmission. The diffraction experiment provided the lattice strains for 0 degree and 90 degrees, the simulation is an interpolation between those points and measurement is necessary to verify the strain path, however the comparison between the measured points and simulated point at 0 degrees and 90 degrees are in good

agreement and their comparison is shown in Tables 6.3 and 6.4. To illustrate the effect of the strain on the neutron transmission, Figure 6.19 presents the neutron transmission simulation of the four states on the aforementioned four lattice planes. The maximum plastic exhibits the most displacement, while the residual Bragg-edge did not return to the reference Bragg-edge location. This procedure can be repeated for bcc and fcc materials given the spherical harmonics coefficient are provided.

6.4 Summary

The effect of the lattice strain on neutron transmission spectra was calculated using a single crystal to polycrystal approach. This approach allows for the calculation of lattice on both single crystal and polycrystals. For single crystals, two different lattice strain calculation models were demonstrated; first the lattice strain was calculated by considering a macro-strain, second the lattice strain was calculated by considering a macro-stress. For polycrystalline specimens the lattice is calculated by first considering a macro-strain, next the elastic induced shifts of Bragg-edges were

Table 6.3: Comparison between simulated strain and measured on 316 stainless steel sample with loading direction parallel to loading direction.

	[200]		[311]		[220]		[111]	
	Exp($\mu\epsilon$)	Sinpol($\mu\epsilon$)	Exp($\mu\epsilon$)	Sinpol($\mu\epsilon$)	Exp($\mu\epsilon$)	Sinpol($\mu\epsilon$)	Exp($\mu\epsilon$)	Sinpol($\mu\epsilon$)
Elastic (264.35 Mpa)	1818	1806	1488	1480	1227	1242	1085	1096
Plastic (315.23 Mpa)	2357	2384	1832	1821	1408	1435	1317	1292
Max Plastic (584.75 Mpa)	5844	5779	3747	3720	2485	2532	2549	2534
Residual (21.36 Mpa)	1384	1532	440	449	-65	-155	-148	-158

Table 6.4: Comparison between simulated strain and measured on 316 stainless steel sample with loading direction perpendicular to loading direction.

	[200]		[311]		[220]		[111]	
	Exp($\mu\epsilon$)	Sinpol($\mu\epsilon$)	Exp($\mu\epsilon$)	Sinpol($\mu\epsilon$)	Exp($\mu\epsilon$)	Sinpol($\mu\epsilon$)	Exp($\mu\epsilon$)	Sinpol($\mu\epsilon$)
Elastic (264.35 Mpa)	-598	-609	-427	-416	-345	-319	-220	-206
Plastic (315.23 Mpa)	-728	-706	-465	-470	-420	-389	-277	-249
Max Plastic (584.75 Mpa)	-1747	-1756	-757	-773	-930	-880	-515	-482
Residual (21.36 Mpa)	-333	-343	104	136	9	10	34	57

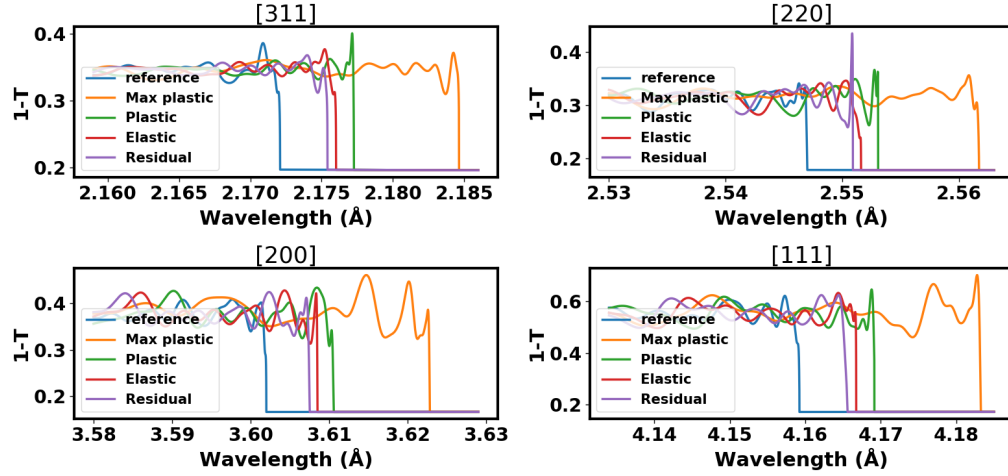


Figure 6.19: Simulated lattice strain of the 111, 200, 220, and 311 Bragg-edge in the 316 stainless steel sample.

simulated by considering the Voigt, Reuss and Hill models. Considering these models allow for taking into account the elastic anisotropy that are present in most metallic alloys, and may improve the transmission data interpretation for the estimation of residual strains. Furthermore, lattice strain were simulated based on diffraction data in which both elasticity and plasticity is considered, the lattice strain is described in terms of spherical harmonics, the single to polycrystal simulation approach allows for lattice strain calculation for any fcc or bcc materials given the spherical harmonics coefficient are provided.

Chapter 7

Summary

7.1 Discussion and Conclusions

A novel approach to the modeling of neutron transmission Bragg-edges was presented in this thesis. This new approach modeled neutron transmission Bragg-edges from single crystal to polycrystalline. The simulation tool which is called *Sinpol* offers new options to simulate neutron transmission on more complex samples when compared to existing neutron transmission simulators. A detailed theoretical analysis of the energy-dependent neutron transmission of crystalline materials is presented. The modeling framework makes special emphasis in the capability for quantitative prediction of the transmission of crystalline materials for all possible micro-structures, from single and mosaic crystals to textured polycrystals.

Sinpol provides an easy approach to simulate single crystal neutron transmission by simply entering the Euler angles which aligned the crystals in the neutron beam. This approach was benchmarked with data found in literature. Furthermore, a distribution of crystals was entered to simulate the neutron transmission spectra of polycrystals. Simulated polycrystal neutron transmission spectra were compared to neutron transmission spectra measured at the VULCAN instrument located at the

SNS. A function to simulate preferred orientation in a sample has been implemented by describing the texture in terms of ideal orientations. The simulation of the effect of texture on neutron transmission was compared with the measurement of cubic texture on a Inconel-718 bulk sample. The ability to simulate the effect of strain on neutron transmission is shown including consideration of the effect of stress on the lattice strain. Simulation of strain on both single crystal and polycrystal material was executed by considering the Voigt, Reuss and Hill approximations for isotropic polycrystal. A phenomenological approach is demonstrated for strains obtained from diffraction data.

In this study, the number of grains in a distribution necessary to observe Bragg-edges at a specific wavelength is presented. Furthermore, the number of grains that contribute to specific Bragg-edge are simulated. Detailed simulations were performed to study the number of grains contributing to the more pronounced Bragg-edges for different texture components. For uniform distributions, the low number of grains simulated in the last four Bragg-edges may have implication for strains measurement.

For tomography consideration the sample is rotated around a vertical and neutron transmission is simulated. The peak movements for single crystals were studied, the rotation of texture in bulk sample were simulated and the movement of the Bragg-edge as a function of rotation. Similar simulations of a sample with strain applied were studied as a function of rotation. Summarizing, it can be stated that *Sinpol* is a big step forward in the simulation of the Bragg-edge transmission technique, both for the efficiency of the data analysis and especially the quality of the results when compared to neutron imaging measurement. The model presented in this work would allow the use of energy-resolved neutron transmission for the analysis of oligocrystals.

Apart from developing the first transmission tool that considered both single crystal and polycrystal, below is a list of technical contributions that were addressed in my research efforts

- I developed a detailed theoretical model for energy-dependent neutron coherent cross section of mosaic crystals, using the Sears lamellar solutions of neutron transport equations in transmission. Until now, the Sears solutions have been used only in diffraction for neutron monochromators calculations and the transmission through single crystal neutron filters have been treated in approximate ways.
- The Sears approach does not cover the multiple reflection case, when multiple reciprocal lattice points are located near the Ewald sphere. For these cases I introduced an approximate phenomenological solution.
- Based on the new physical approach, I developed a simulation code able to generate various populations of grains in a single phase material and obtain neutron transmission curves for oligo-crystals and poly-crystals. As a first tool of this type, it allows accurately calculating the positions and shapes of Bragg-dips in single crystal transmission spectra, as well as Bragg-edges in polycrystalline aggregates with random orientation distributions. Published transmission experimental data collected on single crystals and on various powders measured at SNS were used to benchmark the code.
- Applied simulation code to quantify the effect of secondary extinction and insufficient grain sampling statistics on energy dispersive neutron imaging resolution.
- Performed a broad study of transmission patterns corresponding to texture components commonly present in cubic metallic alloys using *Sinpol's* ability to simulate preferential grain orientation distributions.

- Verified transmission simulation performance on a highly textured Inconel alloy using texture information in the form of an orientation distribution function (ODF).
- The effect of elastic strain on single crystal Bragg-dips positions was also studied, including the elastic anisotropy present in most of the metallic alloys. The elastically induced shifts of Bragg-edges were also simulated by considering Voigt, Reuss and self-consistent models. The new approach allows for taking into account the elastic anisotropy and may improve the transmission data interpretation for the estimation of residual strains.

7.2 Future Work

The simulation of the neutron transmission spectra for single crystals and polycrystals presented here suggests considerable potential for the neutron transmission measurement method. Opportunities of improvements and future work with this technique and possible improvements in the *Sinpol* simulation are mentioned below.

- Grain positions in the software are represented with Euler angle, and transformation from different coordinates are calculated via rotation matrices which matrix multiplications. To improve computational time and remove the ambiguities that might be presented with Euler angles, the grain position can be represented with quaternions thus reducing the number of multiplications necessary for a rotation matrix.
- The simulation uses Sears's formula for the lamellar model. For more general purpose and to remove limit presented by the lamellar model, the spherical grain model for neutron diffraction described in Becker and Coppens [158], should be implemented. The difference is that the latter model allows for the calculation

of the diffraction cross section of samples that are not parallelepiped with faces parallel to the incident and diffracted beams.

- Over the past two decades several non-destructive techniques have been developed to study the shape and map the orientation of grain in polycrystal. In X-ray, techniques such as three-dimensional X-ray diffraction microscopy [159], diffraction contrast tomography [160] and high energy X-ray diffraction [161] are used. These techniques are employed to investigate samples with thickness ranging from micrometers to millimeters and resolutions of 10 nanometers. For bulk sample with thickness ranging from millimeters to centimeters, neutron diffraction contrast tomography [162] [163] is used. This new techniques makes use of both neutron transmission and diffraction. Since the diffraction angles of each lattice plane for each grain is calculated with *Sinpol*, it is possible to also simulate the diffraction spectra of polycrystal. The code has previously been modified [129] to include virtual detectors in diffraction position for the VULCAN instrument at the SNS. For neutron diffraction tomography, the proper detector position and instrument resolution needs to be implemented.
- There is still much to learn about the neutron transmission technique. The modeling of the intensities of lattices planes at the same wavelengths is done by a phenomenological model. It is necessary to further verify this model with a single crystal neutron transmission measurement.
- The effect of mosaic near the Bragg condition is currently not well understood. Further neutron transmission modeling and neutron transmission measurement of single crystal with lattice planes near their respective Bragg conditions, if Bragg-edges are to be used as strain gauges.

Bibliography

- [1] D.P. Mitchell and P.N. Powers. Bragg refelction of slow neutrons. *Physical Review*, 50:486, 1936. [1](#)
- [2] O. Halpern, M. Hamermesh, and M.H. Johnson. The passage of neutrons through crystals and polycrystals. *Physical Review*, 59:981–996, 1940. [1](#)
- [3] E. Fermi, W. Sturm, and R. G. Sachs. The transmission of slow neutron through microcrystalline materials*. *Physical Review*, 71:589–594, 1947. [1](#)
- [4] J.M. Carpenter and C.K. Loong. *Elements of Slow-Neutron Scattering*. Cambridge University Press, Cambridge, UK, 2015. [1](#)
- [5] K. Meggers, H. G. Priesmeyer, W.J. Trela, C.D. Bowman, and M Dahms. Real time neutron transmission investigation of the austenite-bainite transformation in grey iron. *Nuclear Instrument Method B*, 88:423–429, 1994. [1](#)
- [6] S.C. Vogel. *A Rietveld-Approach for the Analysis of Neutron Time-Of-Flight Transmission Data*. PhD thesis, Christian-Albrecht-Univ. Kiel, 2000. [2](#), [3](#), [4](#), [20](#), [89](#), [142](#)
- [7] J.R. Santisteban. Time-of-flight neutron transmission of mosaic crystals. *Journal of Applied Crystallography*, 38:934–944, 2005. [xii](#), [2](#), [71](#), [72](#), [73](#), [75](#)
- [8] J.R. Santisteban, L. Edwards, A. Steuwer, and P.J. Withers. Time-of-flight neutron transmission diffraction. *Journal of Applied Crystallography*, 34:289–297, 2001. [2](#)

- [9] I. S. Anderson, R. L. McGreevy, and H. Z. Bilheux. Neutron Imaging and Applications. *Neutron Scattering Applications and Techniques*. Springer, Boston, Ma, 2009. [2](#), [12](#)
- [10] A. Steuwer, P.J. Withers, J.R. Santisteban, and L. Edwards. Using pulsed neutron transmission for crystalline phase imaging and analysis. *Journal of Applied Physics*, 97, 2005. [2](#), [6](#)
- [11] B. Abbey, Y.S. Zhang, W. Vorster, and A.M. Korsunsky. Feasibility study of neutron strain tomography. *Procedia Engineering*, 1:185–188, 2009. [2](#)
- [12] N. Kardjilov, A. Hilger, I. Manke, M. Strobl, M. Dawson, and J. Banhart. New trends in neutron imaging. *Nuclear Instrument Method A*, 605:13–15, 2009. [2](#)
- [13] A.S. Tremsin, McPhate J.B., Vallergera J.V., and et al. High- resolution strain mapping through time-of-flight neutron transmission diffraction with a microchannel plate neutron counting detector. *Strain*, 48:296–305, 2012. [xiv](#), [2](#), [6](#), [8](#)
- [14] R. Woracek, D. Penumadu, N. Kardjilov, A. Hilger, M. Boin, J. Banhart, and I. Manke. 3d mapping of crystallographic phase distribution using energy-selective neutron tomography. *Adv. Mater.*, 26:4069–4073, 2014. [2](#)
- [15] M. Adib, N. Habib, I. Bashter, H.N. Morcos, M. Fathallah, and M.S. El-Mesiry abs A.Saleh. Neutron characteristics of single-crystal magnesium fluoride. *Annals of Nuclear Energy*, 60:163–171, 2013. [2](#)
- [16] Mervat Said El Mesiry. *Neutron transmission through crystalline materials*. PhD thesis, Tanta, Egypt, 2010. [3](#), [9](#), [15](#)
- [17] G.E. Bacon and R.D. Lowde. *Acta Crys.*, 1:303, 1948. [3](#)

- [18] O.W. Dietrich and L. A. Nielsen. The effect of experimental resolution on crystal reflectivity and secondary extinction in neutron diffraction. *Acta Cryst.*, 18:184, 1965. [3](#), [52](#)
- [19] V.F. Sears. Neutron scattering length and cross section. *Neutron News*, 3:29–37, 1992. [3](#), [29](#), [52](#)
- [20] M. Boin. nxs: a program library for neutron cross section calculations. *Journal of Applied Crystallography*, 45:603–607, 2012. [xiv](#), [3](#), [5](#), [6](#), [7](#), [89](#), [90](#)
- [21] T.M. Sabine. A reconciliation of extinction theories. *Acta Crystallographica*, A44:374–379, 1988. [3](#)
- [22] T.M. Sabine. Extinction in polycrystalline materials. *Acta Crystallographica*, 38:507–518, 1985. [3](#)
- [23] H. Sato, T. Kamiyama, and Y. Kiyanagi. A rietveld-type analysis code for pulsed neutron bragg-edge transmission imaging and quantitative evaluation of texture and microstructure of a welded -iron plate. *Materials Transactions*, 52:1294–1302, 2011. [3](#), [80](#), [118](#), [142](#)
- [24] C. D. Bowman, P. A. Egelstaff, and H. G. Priesmeyer. *Experiments Using Single Neutron Pulses*, volume II of *International Collaboration on Advanced Neutron Sources*, pages 840–847. Kek report 90-25 edition, 1991. [4](#)
- [25] F. Wever. *Z. Phys.*, 28:69, 1924. [5](#)
- [26] G.L. Schulz. *J. Appl. Phys.*, 20:1033, 1949. [5](#)
- [27] Lefmann K. and Nielsen K. Mcstas, a general software package for neutron ray-tracing simulations. *Neutron News*, 10:20–23, 1999. [5](#)
- [28] J.R. Santisteban, L. Edwards, M.E. Fitzpatrick, A. Steuwer, and P.J. Withers. Engineering applications of bragg-edge neutron transmission. *Applied Physics A: Materials Science & Processing*, 74:s1433–s1436, 2002. [xiv](#), [6](#), [7](#)

- [29] Abbey B., Zhang S. Y., Vorster W., and Korsunsky A. M. Feasibility study of neutron strain tomography. *Procedia Engineering* 1, 1:185–188, 2009. [6](#)
- [30] R. Woracek, D.Penumadu, N. Kardjilov, A. Hilger, M.Strobl, R.C. Wimpory, I.Manke, and J. Banhart. Neutron bragg-edge- imaging for strain mapping under in situ tensile loading. *Journal of Applied Physics*, 109, 2011. [6](#)
- [31] W.R.B. Lionheart and P.J. Withers. Diffraction tomography of strain. *Inverse Problems*, 31, 2015. [6](#)
- [32] C.M. Wensrich, J.N. Hendricks, and M.H. Meylan. Bragg edge neutron transmission strain tomography in granular systems. *Strain*, 52:80–87, 2016. [8](#)
- [33] C.M. Wensrich, J.N. Hendricks, A. Greggs, M.H. Meylan, V. Luzin, and A.S. Tremsin. Bragg-edge neutron transmission strain tomography for in situ loadings. *NIMB*, 383:52–58, 2016. [8](#)
- [34] W. Mampe W., P. Ageron, and et al. Neutron lifetime measured with stored ultracold neutrons. *Physical Review Letters*, 63:593–596, 1989. [10](#)
- [35] W. Mampe W., P. Ageron, and et al. Neutron lifetime from a liquid walled bottle. *Nuclear Instrument Methods*, A284:111–115, 1989. [10](#)
- [36] James Byrne. *Neutron,Nuclei Matter: An Explorationof the Physics of Slow Neutrons*. Dover Pubns, Mineola,New York, 2011. [10](#)
- [37] J.M. Carpenter and W.B. Yelon. Neutron sources. In K.Skold and D.L.Price, editors, *Methods of Experimental Physics*, volume 23 of *Part A*, pages 99–197. Publ. Academic Press Inc., 1986. [11](#)
- [38] D. Q. Wang. *Strain Measurement Using Neutron Diffraction*. PhD. Thesis, Materials Discipline,Open University, Milton Keynes, UK, 1996. [11](#), [15](#)

- [39] <http://neutrons2.ornl.gov/facilities/sns/works.shtml>. 11
- [40] G.E. Bacon. *Neutron Diffraction*. Clarendon Press, Oxford, 1967. 11, 30, 31, 33
- [41] M.E. Fitzpatrick and A. Lodini, editors. *Analysis of Residual Stress by Diffraction using Neutron and Synchrotron Radiation*. Taylor Francis, 2003. 12
- [42] D. J. Hughes. *Pile Neutron Research*. Addison-Wesley, New York, 1953. 12
- [43] C.G. Windsor. *Pulsed Neutron Scattering*. Taylor Francis, London, 1981. 12, 13
- [44] M. F. L’Annunziata and W. Burkart. *Radioactivity: introduction and history*. Amsterdam, 2007. 12
- [45] N.J. Carron. *An Introduction to the Passage of Energetic Particles Through Matter*. Taylor Francis, Boca Raton, 2007. xii, 12
- [46] E. Macherauch, H. Wohlfahrt, and U. Wolfstieg. Zur zweckmayigen definition von eigenspannungen. *Hrterei-Tech. Mitt.*, 28:201–211, 1973. 15
- [47] U. Wolfstieg and E. Macherauch. Zur definition von eigenspannungen. *Hrterei-Tech.Mitt.*, 31:2–3, 1976. 15
- [48] K.H. Kloos. Eigenspannungen, definition und entstehungsursachen. *Materialwiss. Werkstofftech*, 10:293–302, 1979. 15
- [49] B.D. Cullity. Some problems in x-ray stress measurements. *Adv. in X-ray Anal*, 60:259–271, 1977. 15
- [50] I. C. Noyan and J. B. Cohen. *Residual Stress. Measurement by Diffraction and Interpretation*. Springer, New York, 1987. 15

- [51] A. Lodini and M. Perrin. Analyse des contraintes mecaniques par diffraction des rayons x et des neutrons. *Editions du CEA, Saclay*, 1996. [16](#)
- [52] A. Lodini. Analysis of residual stresses from materials to biomaterials. *Editions IITT, Marne Vallee*, 1997. [16](#)
- [53] K. Hirschi. *Thesis Universite de Reims*. PhD thesis, Reims. France, 1999. [16](#), [17](#)
- [54] M. Ceretti. *Thesis Universite de Reims*. PhD thesis, Reims. France, 1993. [16](#)
- [55] W. Voigt. *Lehrbuch der Kristallphysik*. 1st ed. Taubner, Leipzig, 1910. [18](#), [19](#), [134](#), [135](#), [138](#), [139](#)
- [56] A. Reuss. Berechnung der fließgrenze von mischkristallen auf grund der plastizitätsbedingung fuer einkristalle. *ZAMM J. Appl. Math. Mech /Zeitschrift fur Angewandte Mathematik und Mechanik*, 23:49–58, 1929. [18](#), [19](#), [138](#)
- [57] E.J. Kröner. *J Mech. Phys. Solids.*, 15:319–329, 1967. [18](#)
- [58] R. Hill. *Proc. Phys. Soc.*, A65:349–354, 1952. [18](#), [19](#)
- [59] H. Neerfeld. *Mitt. K.W.I. Eisen Düsseldorf*, 24:64–70, 1942. [18](#)
- [60] E. Kisi and C. Howard. *Applications of Neutron Powder Diffraction*, volume 24. Oxford Science Publications, 2008. [20](#)
- [61] F. Kropff and J.R. Granada. Cripo: A fast computer code for the evaluation of σ_{total} polycrystalline materials. [20](#)
- [62] M. Boin. *Developments towards the tomographic imaging of local crystallographic structures*. PhD thesis, Open University, Milton Keynes, 2011. [21](#), [142](#)
- [63] C.G. Darwin. The theory of x-ray reflexion. part ii. *Philosophical Magazine*, 27(160):675–690, 1914b. [24](#), [35](#)

- [64] P.P. Ewald. Zur begrundung der kristalloptik. iii. die kristalloptic der rontgenstrahlen. *Ann. Physik*, 54:519–595, 1917. [24](#), [33](#)
- [65] M. Von. Laue. Die dynamische theorie der rontgenstrahlinterferenzen in neuer form. *Ergeb. Exakt. Naturwiss*, 10:133–158, 1931. [24](#), [33](#)
- [66] J. J. Sakurai. *Modern Quantum Mechanics*. Addison-Wesley, New York, 1994. [25](#), [26](#)
- [67] J.S Townsend. *A Modern Approach Quantum mechanics*. University Science Books, 2000. [25](#)
- [68] N. Zettili. *Quantumn Mechanics Conepts and Applications*, volume 24. John Wiley and SonS, 2001. [25](#)
- [69] E. Merzbacher. *Quantumn Mechanics 2nd Edition*, volume 24. John Wiley and Sons, 2001. [25](#)
- [70] Victoria M. Neild and David A. Keen. *Diffuse Neutron Scattering from Crystalline Materials*. Clarendon Press, Oxford, 2001. [26](#), [27](#)
- [71] G.L. Squires. *Introduction to the Theory of Thermal Neutron Scattering*. Clarendon Press, New york, 1978. [27](#), [33](#)
- [72] S.W. Lovesey. *Theory of Neutron Scattering from Condensed Matter, Volume 1: Nuclear Scattering*. Clarendon Press, Oxford, 1986. [27](#)
- [73] P.A. Egelstaff. *Thermal Neutron Scattering*. Academic Press, London, 1989. [27](#)
- [74] A. Furrer, J. Mesot, and T. Strassle. *Neutron Scattering in Condensed Matter Physics (Series on Neutron Techniques and Applications) 1st Edition*, volume 4. World Scientific, 2009. [28](#)
- [75] C. Kittel. *Introduction to Solid State Physics 2nd Edition*. John Wiley and Sons, 1996. [28](#)

- [76] V.F. Sears. *Neutron Optics*. Oxford University Press, Oxford, 1989. [29](#), [34](#)
- [77] <https://www.ncnr.nist.gov/resources/n-lengths/>. [29](#), [59](#)
- [78] J.M. Cassels. The scattering of neutrons by crystals. In O. R. Frisch, editor, *Progress in Nuclear Physics*, volume 65, pages 185–215. Pergamon Press, London, 1950. [30](#)
- [79] I.I. Gurevich and L.V. Tarasov. *Low-energy Neutron Physics*. North-Holland Publishing- Amsterdam, 1968. [xiv](#), [31](#)
- [80] R. Weinstock. *Phys. Rev*, 65:1, 1944. [32](#)
- [81] S.A. Wermer. Extinction in mosaic crystals. *Journal of Applied Physics*, 45(8):3246–3254, 1974. [33](#), [35](#)
- [82] C.G. Darwin. The theory of x-ray reflexion. part i. *Philosophical Magazine*, 27(158):315–333, 1914a. [33](#), [35](#)
- [83] C.G. Darwin. The reflexion of x-rays from imperfect crystals. *Philosophical Magazine*, 43(257):800–829, 1922. [35](#)
- [84] A.K. Freund. *Nucl. Instrum. Methods*, 213:495, 1983. [50](#), [51](#)
- [85] W. H. Zachariasen. *Theory of X-ray Diffraction in Crystals*. New York: Wiley, 1975. [52](#)
- [86] G. E. Bacon. *Neutron Diffraction 3rd edn*. Oxford:Clarendon, 1975. [52](#)
- [87] M. Renninger. 'umweganregung' eine bisher unbeachtete wechselwirkungsercheinung bei raumgitterintererenzen. *Z. Phys*, 106:141, 1937. [53](#)
- [88] R.M. Moon and C.G. Shull. The effects of simultaneous reflections on single-crystal neutron diffraction intensities. *Acta Crystallogr.*, 17:805, 1964. [53](#)

- [89] E. Rossmanith. Approximate calculation of multiple-diffraction patterns based on renninger’s kinematical simplest approach. *Journal of Applied Crystallography*, 33:921–927, 2000. [53](#)
- [90] R. W. Grosse-Kunstleve. Algorithms for deriving crystallographic space-group information. *Acta Cryst*, A55:383–395, 1999. [58](#)
- [91] Ask Larsen, Jens Mortensen, Jakob Blomqvist, Ivano Castelli, Rune Christensen, Marcin Dulak, Jesper Friis, Michael Groves, Bjork Hammer, Cory Hargus, Eric Hermes, Paul Jennings, Peter Jensen, James Kermode, John Kitchen, Esben Kolsbjerg, Joseph Kubal, Kristen Kaasbjerg, Steen Lysgaard, Jon Maronsson, Tristan Maxson, Thomas Olsen, Lars Pastewka, Andrew Peterson, Carsten Rostgaard, Jakob Schiøtz, Ole Schütt, Mikkel Strange, Kristian Thygesen, Tejs Vegge, Lasse Vilhelmsen, Michael Walter, Zhenhua Zeng, and Karsten Wedel Jacobsen. The atomic simulation environment — a python library for working with atoms. *Journal of Physics: Condensed Matter*, 2017. [59](#)
- [92] H. J. Bunge. *Texture Analysis in Materials Science*. London:Butterworths, 1982. [xv](#), [62](#), [63](#), [64](#)
- [93] N.C. Popa. Diffraction-line shift caused by residual stress in polycrystal for all laue groups in classical approximations. *Journal of Applied Crystallography*, 33:103–107, 2000. [64](#), [120](#), [121](#), [135](#), [139](#)
- [94] J.H. Halton. On the efficiency of certain quasi-random sequences of points in evaluating multi-dimensional integrals. *Numerische Mathematik*, 2:84–90, 1960. [69](#)
- [95] L.L. Dessieux, A.D. Stoica, and P.R. Bingham. *Review of Scientific Instrument*, 89:025103, 2018. [71](#), [91](#), [96](#), [97](#), [106](#)

- [96] F. Malamud and J. Santisteban. Full-pattern analysis of time-of-flight neutron transmission of mosaic crystals. *Journal of Applied Crystallography*, 49:348–365, 2016. [xii](#), [76](#), [77](#)
- [97] W. Kockelmann, G. Frei, E.H. Lehmann, P. Vontobel, and J.R. Santisteban. Energy-selective neutron transmission imaging at a pulsed source. *Nuclear Instrument and Methods in Physics Research A*, 578:421–434, 2007. [78](#), [79](#), [96](#)
- [98] J.J. Bucki and K.J.Kurzydowski. Measurements of grain volume distributions parameters in polycrystals characterized by a log-normal distribution function. *Scripta Metall*, 28:689–692, 1993. [81](#), [177](#), [178](#)
- [99] XL. Wang and A. D. Stoica. Focusing neutron guides for vulcan-design aspects, estimated performance, and detector deployment. *Nuclear Instrument and Methods A*, 600:309–312, 2009. [84](#)
- [100] K. An, H. D. Skorpenske, A. D. Stoica, and et al. Vulcan- the engineering diffractometer at the sns. *Metallurgical and Materials Transactions A*, 42A:95–99, 2011. [84](#)
- [101] G. Song, J. Y. Y. Lin, J. C. Bilheux, Q. Xie, K. An, A. D. Stoica, M. M. Kirka, R. R. Dehoff, S. N. Dryepontdt, A. Tremsin, L. J. Santodonato, and H.Z. Bilheux. Characterization of crystallographic structures using bragg-edge neutron imaging at the spallation neutron source. *Journal Imaging*, 3:65, 2017. [84](#)
- [102] A.C. Larson and R.B. Von Dreele. *General structure analysis (GSAS) LAUR 86-748 Los Alamos National Laboratory Report*, 2004. [85](#)
- [103] H. Sato, Y. Shiota, S. Morooka, Y. Todaka, N. Adachi, S. Sadamastu, K. Oikawa, M. Harada, S. Zhang, Y. Su, T. Kamiyama, M. Ohnuma, M. Furusak, T. Shinohara, and Y. Kiyanagi. Inverse pole figure mapping of

- bulk crystalline grains in polycrystalline steel plate by pulsed neutron bragg-dip transmission imaging. *Journal of Applied Crystallography*, 50:1601–1610, 2017. [86](#)
- [104] S. Suwas and R. K. Ray. *Crystallographic Texture of Materials*. Springer, London, 2014. [88](#)
- [105] C. Escher and G. Gottstein. *Acta Mater*, 46:525, 1998. [88](#)
- [106] I.C. Hsiao, S.W. Su, and J.C. Huang. *Metall. Mater. Trans.*, 31A:2000–2169, 2000. [88](#)
- [107] T.R. McNelley, D.L. Swisher, and M.T. Perez-Prado. *Metall. Mater. Trans.*, 33:279, 2002. [88](#)
- [108] P. Echlin, C.E. Fiori, J.I. Goldstein, D.C. Joy, C.E. Lyman, E. Lifshin, D.E. Newbury, and A.D. Romig. *Scanning Electron Microscopy and X-ray Microanalysis*. Plenum Press, London,, 1992. [88](#)
- [109] K. Sztwertnia and F. Haessner. *Mater. Sci. Forum*, 157-162:1291, 1994. [88](#)
- [110] X. Huang. *Scr. Mater*, 38:1697, 1998. [88](#)
- [111] S. Mathies and G. Vinel. *Phys. Status Solidi B*, 112:K115–K120, 1982. [89](#)
- [112] K. Pawlik. *Phys. Status Solidi B*, 134:477–483, 1986. [89](#)
- [113] R. Hielscher and H. Schaeben. *J. Appl. Crystallogr.*, 41:1024–1037, 2008. [89](#)
- [114] D. Chateigner. *Combined Analysis*. Wiley, 1988. [90](#)
- [115] H. Sato, T. Kamiyama, and Y. Kiyanagi. A rietveld-type analysis code for pulsed neutron bragg-edge transmission imaging and quantitative evaluation of texture and microstructure of a welded α -iron plate. *Materials Transactions*, 52, No 6:1294–1302, 2011. [90](#)

- [116] W.A. Dollase. Correction of intensities for preferred orientation in powder diffractometry: Application of the march model. *Journal of Applied Crystallography*, 19:267–272, 1986. [90](#)
- [117] J.R. Santisteban, M.A. Vicente Alvarez, P. Vizcaino, A.D. Banchik, S.C. Vogel, A.S. Tremsin, J.V. Vallegra, J.B. McPhate, E. Lehmann, and W. Kockelmann. Texture imaging of zirconium based components by total neutron cross-section experiments. *Journal Nuclear Materials*, 425:218–227, 2012. [90](#)
- [118] K. An, H. Skorpenske, A.D. Stoica, and et al. *Metall. Mater. Trans. A*, 42A:95, 2011. [91](#), [111](#)
- [119] H.J. Bunge. Zur dartellung allgemeiner texturen. *Z. Metall.*, pages 872–874, 1965. [92](#)
- [120] R.J. Roe. Description of crystallite orientation in polycrystalline materials iii. general solution to pole figure inversion. *J. Appl. Phys.*, 36:2024–2031, 1965. [92](#)
- [121] H.J. Bunge. *Zeitschrift fuer Metallkunde*, 56:872–874, 1965. [92](#)
- [122] S. Mathies. *Physica Status Solidi (b)*, 92:K135–K137, 1979. [92](#)
- [123] H.J. Bunge and C. Esling. *Journnl Physique Lett.*, 40:L–627, 1979. [92](#)
- [124] K. Luecke, J. Pospiech, K.H. Virnich, and J. Jura. *Acta Metallurgica*, 29:167, 1981. [92](#)
- [125] M. Dahms and H. J. Bunge. *Journal of Applied Crystallography*, 22:439–447, 1989. [92](#)
- [126] S Matthies, G.W. Vinel, and K. Helming. *Standard Distributions in Texture Analysis*, volume 1. Akademie-Verlag Berlin, 1987. [92](#), [94](#)
- [127] S. Li, Q. Zhao, Z. Liu, and F. Li. A review of texture evolution mechanisms during deformation by rolling in aluminum alloys. *JMEPEG*, 27:3350–3373, 2018. [105](#)

- [128] J. J. Sidor, R. H. Petrov, and L. A. I. Kestens. Modeling the crystallographic texture changes in aluminum alloys during recrystallization. *Acta Materialia*, 59:5735–5748, 2011. [105](#)
- [129] G. Stoica, L. L. Dessieux, A.D. Stoica, S. Vogel, G. Muralidharan, B. Radhakrishnan, S. Gorti, K. An, D. Ma, and X.L. Wang. Distinct recrystallization pathways in coldrolled alloy, al2%mg, evidenced by insitu neutron diffraction. *Quantum Beam Science*, 2, 2018. [106](#), [152](#)
- [130] X. L. Wang and A. D. Stoica. *Nucl. Instrum. Methods Phys. Res., Sect. A*, 600:309, 2009. [111](#)
- [131] R. Dehoff, M. Kirka, W. Sames, H. Bilheux, and L. Lowe and S. Babu A. Tremsin. *Mater. Sci. Technol*, 31:931, 2015. [111](#)
- [132] Q. Xie, G. Song, S. Gorti, A. Stoica, B. Radhakrishnan, J. Bilheux, M. Kirka, R. Dehoff, H. Z. Bilheux, and K. An. Applying neutron transmission physics and 3d statistical full-field model to understand 2d bragg-edge imaging. *Journal of Applied Physics*, 123:074901, 2018. [111](#)
- [133] D. Ma, A. D. Stoica, Z. Wang, and M.A. Beese. Crystallographic texture in an additively manufactured nickel -base superalloy. *Materials Science and Engineering A*, 684:45–53, 2017. [113](#), [116](#)
- [134] A.W.T. Gregg, J.N. Hendriks, C.M. Wensrich, and M.H. Meylan. Tomographic reconstruction of residual strain in axisymmetric systems from bragg-edge neutron imaging. *Mechanical Research Communications*, 85:96–103, 2017. [118](#)
- [135] A.S. Tremsin, W. Kockelmann, J.F. Kelleher, A.M. Paradowska, R.S. Ramadhan, and M.E. Fitzpatrick. Energy-resolved neutron imaging for reconstruction of strain introduced by cold working. *Journal of Imaging*, 4:48, 2018. [118](#)

- [136] K. Iwase, H. Sato, S. Harjo, T. Kamiyama, T. Ito, S. Takata, K. Aizawa, and Y. Kiyonagi. in situ lattice strain mapping during tensile loading using the neutron transmission and diffraction methods. *J. Appl. Crystall.*, 45:113–118, 2012. [118](#)
- [137] M.T. Hutchings, P.J. Withers, T.M. Holden, and T. Lorentzen. *Introduction to the Characterization of Residual Stress by Neutron Diffraction*. Boca Raton: Taylor and Francis, 2005. [133](#)
- [138] W.A. Wooster. *Tensors and Group Theory for Physical Properties of Crystals*. Oxford: Clarendon Press, 1973. [134](#), [135](#)
- [139] J.F. Nye. *Physical Properties of Crystals*. Oxford at the Clarendon Press, 1957. [135](#)
- [140] K. Helbig. *Foundations of Anisotropy for Exploration Seismics*. Tarrytown, NY: Pergamon, 1994. [135](#)
- [141] J. Dellinger, Vasicek D, and C. Sondergeld. Kelvin notation for stabilizing elastic-constant inversion. *Rev. IFP*, 53:709–719, 1998. [135](#)
- [142] W. Kelvin and L. Thomson. *Phil. Trans. R. Soc.*, 166:481, 1856. [135](#)
- [143] L.J. Wapole. The stress-strain law of a textured aggregate of cubic crystals. *J. Mech. Phys. Phys. Solids*, 33:363–370, 1985. [135](#)
- [144] R. Hill. Continuum micromechanics of elastoplastic polycrystals. *J. Mech. Phys. Solids*, 23:13:89–101, 1965a. [138](#)
- [145] R. Hill. Essential structure of constitutive laws for metal composites and polycrystals. *J. Mech. Phys. Solids*, 23:15:79–85, 1967. [140](#)
- [146] N.C. Popa and D. Balzar. Elastic strain and stress determination by rietveld refinement: generalized treatment for textured polycrystals for all laue classes. *J. Appl. Crystall.*, 34:187–195, 2001. [142](#)

- [147] N.C. Popa, D. Balzar, and S.C. Vogel. Elastic macro strain and stress determination by powder diffraction: spherical harmonics analysis starting from the voigt model. *J. Appl. Crystall.*, 47:154–159, 2014. [142](#)
- [148] N.C. Popa. Spherical harmonics analysis based on the reuss model in elastic macro strain and stress determination by powder diffraction. *J. Appl. Crystall.*, 50:1735–1743, 2017. [142](#)
- [149] T. Lorentzen¹, M.R. Daymond, B. Clausen, and N. Tome. Lattice strain evolution during cyclic loading of stainless steel. *Acta Mat.*, 50:1627, 2002. [142](#)
- [150] Y.D. Wang, H. Tian, A.D. Stoica, X.L. Wang, D.J., P.K. Liaw, and J.W. Richardson. The development of grain-orientation-dependent residual stressess in a cyclically deformed alloy. *Nat. Material*, 2:103–106, 2003. [142](#)
- [151] X.L. Wang, Y.D. Wang, A.D. Stoica, D.J. Horton, H. Tian, H. Choo, J.W. Richardson, and E. Maxey. Inter-and intragranular stresses in cyclically-deformed 316 stainless steel. *Materials Science and Engineering A*, 18785:1–6, 2005. [142](#)
- [152] A.D. Stoica, X.L. Wang, D.J. Horton, H. Tian, L. Yang, J.W. Richardson, E. Maxey, P.K. Liaw, and D.Shi. Neutron diffraction study of fatigue behaviors in 316ln stainless steel. *J. of Neutron Research*, 12:99–103, 2004. [142](#)
- [153] C.M Brakman. *J. Appl. Cryst.*, page 16:325, 1983. [143](#)
- [154] C.M Brakman and P. Penning. *Acta Cryst. A*, page 44:163, 1988. [143](#)
- [155] R.H. Marion and J.B. Cohen. *Adv. X-ray Anal*, page 18:466, 1975. [143](#)
- [156] I.C. Noyan and L.S. Schadler. *Metall. Mater. Trans, A*, page 25:341, 1994. [143](#)
- [157] T. Ungár, A.D. Stoica, G. Tichy, and X.-L. Wang. Orientation-dependent evolution of the dislocation density in grain populations with different

- crystallographic orientations relative to the tensile axis in a polycrystalline aggregate of stainless steel. *Acta Materiala*, 66:251–261, 2014. [143](#)
- [158] P.J. Becker and P. Coppens. Extinction within the limit of validity of the darwin transfer equations. i. general formalisms for primary and secondary extinction and their application to spherical crystals. *Acta Cryst.*, A30:129, 1974. [151](#)
- [159] H. F. Poulsen, S. F. Nielsen, E. M. Lauridsen, S. Schmidt, R. M. Suter, U. Lienert, L. Margulies, T. Lorentzen, and D. Juul Jensen. Three-dimensional maps of grain boundaries and the stress state of individual grains in polycrystals and powders. *J Appl Crystall.*, 34:751–756, 2001. [152](#)
- [160] W. Ludwig, S. Schmidt, E.M Lauridsen, and H.F Poulsen. X-ray diffraction contrast tomography: a novel technique for three-dimensional grain mapping of polycrystals. i. direct beam case. *J Appl Crystall.*, 41:302–309, 2008. [152](#)
- [161] R.M. Sutter, D. Hennessy, C. Xiao, and U. Lienert. Forward modeling method for microstructure reconstruction using x-ray diffraction microscopy: Single-crystal verification. *RSI*, 77:123905, 2006. [152](#)
- [162] S. Peetermans and E.H. Lehmann. Simultaneous neutron transmission and diffraction contrast tomography as a non-destructive 3d method for bulk single crystal quality investigations. *Journal of Applied Physics*, 114:124905, 2013. [152](#)
- [163] A. Cerserer and et al. Time-of-flight three dimensional neutron diffraction in transmission mode for mapping crystal grain structures. *Scientific Report*, 7:9561, 2017. [152](#)

Appendix

Appendix A

Inter planar spacing, unit cell volumes, inclination angles

A.1 Inte-Planar Spacing

The equation shown here are used in the *Sinpol* library to calculate the lattice spacings of a given reflection (h, k, l).

Cubic $a = b = c; \alpha = \beta = \gamma = 90^\circ$

$$\frac{1}{d_{hkl}^2} = \frac{h^2 + k^2 + l^2}{a^2}$$

Tetragonal $a = b; c; \alpha = \beta = \gamma = 90^\circ$

$$\frac{1}{d_{hkl}^2} = \frac{h^2 + k^2}{a^2} + \frac{l^2}{c^2}$$

Hexagonal $a = b; c; \alpha = \beta = 90^\circ \gamma = 120^\circ$

$$\frac{1}{d_{hkl}^2} = \frac{4}{3} \left(\frac{h^2 + hk + k^2}{a^2} + \frac{l^2}{c^2} \right)$$

Trigonal $a = b; c; \alpha = \beta = \gamma \neq 90^\circ$

$$\frac{1}{d_{hkl}^2} = \frac{4c^2(h^2 + hk + k^2) + 3l^2a^2}{3a^2c^2}$$

Rhombohedral $a = b; c; \alpha = \beta = \gamma \neq 90^\circ$

$$\frac{1}{d_{hkl}^2} = \frac{(h^2 + hk + k^2) \sin^2 \alpha + 2(hk + kl + hl) \left(\cos^2 \alpha - \cos \alpha \right)}{a^2(1 - 3 \cos^2 \alpha + 2 \cos^3 \alpha)}$$

Orthorhombic $a \neq b \neq c; \alpha = \beta = \gamma = 90^\circ$

$$\frac{1}{d_{hkl}^2} = \frac{h^2}{a^2} + \frac{k^2}{b^2} + \frac{l^2}{c^2}$$

Monoclinic $a \neq b \neq c; \alpha = \beta = 90^\circ; \gamma \neq 90^\circ$

$$\frac{1}{d_{hkl}^2} = \frac{1}{\sin^2 \beta} \left(\frac{h^2}{a^2} + \frac{k^2 \sin^2 \beta}{b^2} + \frac{l^2}{c^2} - \frac{2hl \cos \beta}{ac} \right)$$

Triclinic $a \neq b \neq c; \alpha \neq \beta \neq \gamma$

$$\frac{1}{d_{hkl}^2} = \frac{1}{V^2} \left[h^2 b^2 c^2 \sin^2 \alpha + k^2 a^2 c^2 \sin^2 \beta + l^2 a^2 b^2 \sin^2 \gamma + 2hkabc^2 (\cos \alpha \cos \beta - \cos \gamma) + \right. \\ \left. 2klba^2 c (\cos \beta \cos \gamma - \cos \alpha) + 2hlab^2 c (\cos \gamma \cos \alpha - \cos \beta) \right]$$

A.2 Unit Cell Volume

The equation shown here are used in the *Sinpol* library to calculate the the unit cell volume v_0 of a crystal system by means of the lattice parameters.

Cubic $a = b = c; \alpha = \beta = \gamma = 90^\circ$

$$v_o = a^3$$

Tetragonal $a = b; c; \alpha = \beta = \gamma = 90^\circ$

$$v_o = a^2 c$$

Hexagonal $a = b; c; \alpha = \beta = 90^\circ \gamma = 120^\circ$

$$v_o = \frac{\sqrt{3}a^2 c}{2}$$

Trigonal $a = b; c; \alpha = \beta = \gamma \neq 90^\circ$

$$v_o = \frac{\sqrt{3a^2c}}{2}$$

Rhombohedral $a = b; c; \alpha = \beta = \gamma \neq 90^\circ$

$$v_o = a^3 \sqrt{1 - 3 \cos^2 \alpha + 2 \cos^3 \alpha}$$

Orthorhombic $a \neq b \neq c; \alpha = \beta = \gamma = 90^\circ$

$$v_o = abc$$

Monoclinic $a \neq b \neq c; \alpha = \beta = 90^\circ; \gamma \neq 90^\circ$

$$v_o = abc \sin \beta$$

Triclinic $a \neq b \neq c; \alpha \neq \beta \neq \gamma$

$$v_o = abc \sqrt{1 - \cos^2 \alpha - \cos^2 \beta - \cos^2 \gamma + 2 \cos \alpha \cos \beta \cos \gamma}$$

A.3 Inclination angles

The equation shown here are used in the library to calculate the inclination between two lattice planes. **Cubic** $a = b = c; \alpha = \beta = \gamma = 90^\circ$

$$\cos \alpha = \frac{h_1 h_2 + k_1 k_2 + l_1 l_2}{\sqrt{h_1^2 + k_1^2 + l_1^2} \sqrt{h_2^2 + k_2^2 + l_2^2}}$$

Tetragonal $a = b; c; \alpha = \beta = \gamma = 90^\circ$

$$\cos \alpha = \frac{\frac{h_1 h_2 + k_1 k_2}{a^2} + \frac{l_1 l_2}{c^2}}{\sqrt{\frac{h_1^2 + k_1^2}{a^2} + \frac{l_1^2}{c^2}} \sqrt{\frac{h_2^2 + k_2^2}{a^2} + \frac{l_2^2}{c^2}}}$$

Hexagonal $a = b; c; \alpha = \beta = 90^\circ \gamma = 120^\circ$

$$\cos \alpha = \frac{h_1 h_2 + k_1 k_2 + \frac{1}{2}(h_1 k_2 + h_2 k_1) + \frac{3a^2}{4c^2} l_1 l_2}{\sqrt{h_1^2 + k_1^2 + h_1 k_1 + \frac{3a^2}{4c^2} l_1^2} \sqrt{h_2^2 + k_2^2 + h_2 k_2 + \frac{3a^2}{4c^2} l_2^2}}$$

Trigonal $a = b; c; \alpha = \beta = \gamma \neq 90^\circ$

$$\cos \alpha = \frac{h_1 h_2 + k_1 k_2 + \frac{1}{2}(h_1 k_2 + h_2 k_1) + \frac{3a^2}{4c^2} l_1 l_2}{\sqrt{h_1^2 + k_1^2 + h_1 k_1 + \frac{3a^2}{4c^2} l_1^2} \sqrt{h_2^2 + k_2^2 + h_2 k_2 + \frac{3a^2}{4c^2} l_2^2}}$$

Rhombohedral $a = b; c; \alpha = \beta = \gamma \neq 90^\circ$

$$\cos \alpha = \frac{a^4 d_1 d_2}{v_o^2} \left[lcl \sin^2 \alpha (h_1 h_2 + k_1 k_2 + l_1 l_2) \right. \\ \left. + (\cos^2 \alpha - \cos \alpha) (k_1 l_2 + k_2 l_1 + l_1 h_2 \right. \\ \left. + h_1 l_2 + k_2 h_1 + k_1 h_2) \right]$$

Orthorhombic $a \neq b \neq c; \alpha = \beta = \gamma = 90^\circ$

$$\cos \alpha = \frac{\frac{h_1 h_2}{a^2} + \frac{k_1 k_2}{b^2} + \frac{l_1 l_2}{c^2}}{\sqrt{\frac{h_1^2}{a^2} + \frac{k_1^2}{b^2} + \frac{l_1^2}{c^2}} \sqrt{\frac{h_2^2}{a^2} + \frac{k_2^2}{b^2} + \frac{l_2^2}{c^2}}}$$

Monoclinic $a \neq b \neq c; \alpha = \beta = 90^\circ; \gamma \neq 90^\circ$

$$\cos \alpha = \frac{d_1 d_2}{\sin^2 \beta} \left[\frac{h_1 h_2}{a^2} + \frac{k_1 k_2}{b^2} + \frac{l_1 l_2}{c^2} - \frac{l_1 h_2 + l_2 h_1 \cos \beta}{ac} \right]$$

Triclinic $a \neq b \neq c; \alpha \neq \beta \neq \gamma$

$$\cos \alpha = \frac{d_1 d_2}{v_o^2} \left[lcl h_1 h_2 b^2 c^2 \sin^2 \alpha + k_1 k_2 a^2 c^2 \sin^2 \beta \right. \\ \left. + l_1 l_2 a^2 b^2 \sin^2 \gamma + (h_1 k_2 + h_2 k_1) abc^2 (\cos \alpha \cos \beta - \cos \gamma) \right. \\ \left. + (k_1 l_2 + k_2 l_1) a^2 bc (\cos \beta \cos \gamma - \cos \alpha) \right. \\ \left. + (h_1 l_2 + h_2 l_1) ab^2 c (\cos \alpha \cos \gamma - \cos \beta) \right]$$

Appendix B

Input File Example

The input parameter for neutron simulation with *Sinpol* code is listed below.

```
label=cu
spgnumber=225
thickness=1
orientnum=10000
atomic_number=63
latticea=3.61496
latticeb=3.61496
latticec=3.61496
latticealpha=90.00
latticebeta=90.00
latticegamma=90.00
density= 8.935
mass=63.55
bound_xs=8.035
coherent=7.485
```

incoherent=.55
absorption_xs=3.78
coheren_xs_length=7.718
Debye_Temperature=344

Appendix C

Generation of Log-normal Distribution of Thicknesses

The log-normal distribution for crystallites is parametrized by average value c and the standard deviation b on a logarithmic scale. According to Bucki and Kurzydowski [98], the probability density for a number weighted log-normal grain volume distribution is given as

$$LN_N(v)dv = \frac{1}{vb\sqrt{2\pi}} \exp \left\{ -\frac{1}{2} \left(\frac{\ln v - c}{b} \right)^2 \right\} dv, \quad (\text{C.1})$$

where v is the volume.

The volume weighted log-normal distribution of the grain volume can be written as

$$LN_v(v)dv = \frac{1}{b\sqrt{2\pi}} \exp \left\{ -\frac{1}{2} \left(\frac{\ln v - c}{b} \right)^2 - c - \frac{b^2}{2} \right\} dv. \quad (\text{C.2})$$

Let $v = \tau^3$ where τ is the thickness of a cubic grain; equation C.3 is now expressed as function of the grain thickness τ

$$LN_v(\tau)d\tau = \frac{3\tau^2}{b\sqrt{2\pi}} \exp \left\{ -\frac{1}{2} \left(\frac{\ln \tau - \frac{c}{3}}{\frac{b}{3}} \right)^2 - c - \frac{b^2}{2} \right\} d\tau. \quad (\text{C.3})$$

To create a cumulative grain-size distribution, we have to integrate equation C.3

$$F(\tau) = \int_{-\infty}^{\ln \tau} \frac{3}{b\sqrt{2\pi}} \exp \left\{ -\frac{1}{2} \left(\frac{y - \frac{c}{3}}{\frac{b}{3}} \right)^2 - c - \frac{b^2}{2} \right\} e^{3y} dy \quad (\text{C.4})$$

$$= \frac{1}{2} + \frac{1}{2} \left(\frac{\ln \tau - \frac{c}{3} - \frac{b^2}{3}}{\sqrt{2\frac{b}{3}}} \right). \quad (\text{C.5})$$

Following Bucki and Kurzydowski [98], the volume weighted coefficient of variation (relative std.) for the log-normal distribution is given as

$$c_v^2 = e^{b^2} - 1, \quad (\text{C.6})$$

and the volume weighted mean volume

$$E_v = \tau_v^3 = \exp \left(c - \frac{3b^2}{2} \right). \quad (\text{C.7})$$

To generate a volume weighted log-normal distributed grain thickness, equation C.5 is solved for a randomn uniformly distributed number $y_o \in \{0, 1\}$

$$\tau = \tau_v \left((1 + c_v)^{-\frac{1}{6}} \right) \exp \left[\frac{\sqrt{2 \ln(1 + c_v)}}{3} (2y_o - 1) \right]. \quad (\text{C.8})$$

In the above calculations, the use of volume weighted distribution is appropriate for a column simulation. For multiple rays interacting with multiple columns, an area-weighted distribution should be considered instead of a volume-weighted distribution.

Vita

Luc L Dessieux, was born on November 10, 1973 to parents Luc and Jaccinette Dessieux in Cap-Haitien , Haiti. He received a Bachelor of Arts degree in 1997 from Central Methodist College in Fayette, Missouri where he double majored in Physics and Mathematics. In 1996 he was inducted into Kappa Mu Epsilon mathematics honor society. He received a Masters degree in Physics from the University of Tennessee in Knoxville in December of 2002. He went to work as a computer programmer for a decade. He started graduate work as a PhD candidate at the University of Tennessee in the Fall of 2009, where he studied Neutron physics with focus on Neutron Transmission. On April 22, 2019, Luc successfully defended his dissertation and received his PhD in August.